ESA Contract No. 4000109609/13/NL/JK

Investigation of the mechanism of cometary activity: Predictions and first analysis for the Rosetta target comet 67P/Churyumov-Gerasimenko

Searching for large particles in images of inner comas of comets

Final report

January 15, 2014 – January 27, 2017

Prepared by:
Oksana Shalygina
Horst Uwe Keller
Jürgen Blum

Contents

1. Introduction

Recent results suggest that the mechanism of cometary activity and the near-nucleus coma may substantially differ from what was thought before. Observationally, the recent flyby of Deep Impact spacecraft of comet Hartley 2 showed that, at least for that comet, a significant fraction of the activity is in the form of large (10s of cms) ice blocks [1]. Furthermore, the flybys of Deep Impact at comet Tempel 1 and Hartley 2 showed, for the first time, clear evidence for heterogeneity of the composition of the outgassing material [1]. Experimentally, recent laboratory work suggests that cometary activity can be maintained only if the dust activity is dominated by large (mm or cm-sized) particles [2, 3, 4]. That could be part of the solution of a longstanding puzzle in a cometary science: the onset and maintenance of cometary activity. Earlier laboratory experiments were not able to maintain a "comet" active in the laboratory [5].

Much of cometary activity may be initiated by a break-up of large boulders from the nucleus, but origin of boulders in coma is still an open question. For study this problem it is needed to collect the evidences of the large particles appearance, and get more information about their space distribution, speed, *etc.*

The project has the aim to reanalyse the data from previous cometary flybys with the objective to find evidence for large ice or dust blocks near the cometary nucleus. The first specific objective is to re-analyze existing spacecraft data from cometary flybys. The data acquired with the Halley Multi-Color Camera (HMC) on board Giotto will be reprocessed and analyzed. A detailed analysis of Signal/Noise ration for the detection of large particles will be performed for the most promising images. Furthermore, the method developed for HMC will then be applied to the archival imaging data of the other missions (*e.g.* Deep Impact/EPOXI mission to comet Hartley 2).

2. Halley Multi-Color Camera (HMC) data overview

2.1. Description of Phase I

Input: GIOTTO/HMC data from PI Institute.

Purpose: Re-reduction of those data in view of evidence of large dust or ice particles.

Output: update of Planetary Science Archive (PSA) [6] with re-reduced database.

2.2. GIOTTO/HMC data bases

There are several sources of HMC data:

1. GIOTTO/HMC data in Planetary Science Archive [6]
2. GIOTTO/HMC data in the Planetary Data System [7]
3. Data archive provided by Nick Thomas [1].
4. Data stored on 24 CDs and 16 Digital Data Storage (DDS [2]) cartridges in Open Virtual Memory System (VMS) [3] file system format at Max Planck Institute for Solar System Research (MPS) [4].

The sources 1 and 2 contain the same data archives and they include only images with comet 1P/Halley which were calibrated (*i.e.* dark current, coherent noise, and events removed, responsivity corrected) and then geometrically rectified (see details of images' processing in [8]). They do not contain the flight images and additional data (*e.g.* star observation).

The archive 3 contains the programs and the data in custom format (can be converted into FITS), with the results of several intermediate consecutive stages of the data processing, so-called: "flight" (unprocessed data with the header already converted from the original flight format), "radio" (calibrated data), "geometry" (calibrated data to which the image restoration procedure was applied and which were corrected by the geometrical distortion caused by the specific HMC observation scheme), and "cleaned" (cleaned with an adaptive filter, enhanced by cross-correlation, processed by point spread function (PSF)). See the examples of HMC images in fig. A.1.

Data 4 include the cometary observations and additional images, such as observations of the stars and planets which were obtained for the camera calibration. Besides the images these backups contain some program files. All CDs of data base 4 were read using VMS machine at

[1] Professor of Experimental Physics, Physikalisches Institut University of Bern, Switzerland

[2] Digital Data Storage (DDS) is a format for storing and backing up computer data on tape that evolved from the Digital Audio Tape (DAT) technology

[3] This is a computer server operating system that runs on VAX, Alpha and Itanium-based families of computers, previously known as VAX-11/VMS, VAX/VMS or (informally) VMS

[4] Max-Planck-Institut für Sonnensystemforschung, Justus-von-Liebig-Weg 3, 37077, Göttingen, Germany

MPS and stored in modern format (some data on them are repeated). Two of the DDS cartridges contain archives in a custom format. Information needed for their decoding is lost, so these tapes were only dumped. Thus, 14 tapes were read, 9 of them contain unique information (3 tapes are identical to others, 2 tapes are the home directories and VMS system files, not HMC data, and were not copied).

Available readable HMC data show that there is enough material to study the activity of comet 1P/Halley. However, it was found that not all data obtained by HMC are available now, *e.g.* Altair images are absent, and there is no full information about the PSF applied to produce the "geometrical corrected" level of data (see solution in section 2.4.1).

2.3. Assessment of the radiometric calibration for the weak flux values in HMC images

It is natural to expect that (probable) particles, ejected from the nucleus, increase in number with decreasing size. For the characterization of the observed particles it is required to know the intensity of the light, reflected by a particle. For sub-pixel size particles it is the only measurable quantity connected to their size and albedo. Therefore reliable radiometric calibration of the camera for the expected fluxes is needed. Since the calibration of every photometric detector suffers from uncertainties at a certain level near zero (for instance, because of the imprecise knowledge of the dark current value), it is important to know the smallest intensity value with still reliable calibration. It must be noted also that the obtained by HMC data were compressed by an approximate square-root function, basically a 12-bit to 8 bit lookup table [8]. This compression may slightly effect the noise distribution together with digitization, especially in case of low signal. If for a particular image the difference between true dark matrix and the computed one is comparable to the signal from a particle (or larger), such image can not be used (at least directly) for estimations of the particle properties, because the radiometric calibration is significantly wrong in the range of values, comparable to the dark matrix errors. Therefore these images need to be identified.

If we look at "radio" and geometrically corrected HMC images we see negative values of the signal (see examples in fig. 2.1, totally 166 there are 166 files). The signal level in such images is low and it is important to know the precise value of the noise. There is a Poisson noise on the original signal together with the dark current which (after subtraction of an averaged dark matrix) results in negative counts. Thus we shall check whether the intensity follows the Poisson distribution in the regions with negative values of the signal. Parameters of the Poisson noise in the images at low intensities are connected to the dark current removing procedure and may be signs of over/under-estimation of the dark current value.

It is seen in examples of images (fig. 2.1) that the number of pixels that have negative signal values vary at different images: in case of images FCC00968 and FCC01468 the minimal values reach down to -87, but these are individual pixels, and typically negative values are not smaller than -12.

To check whether these values follow the Poisson distribution, only pixels that have brightness values lower than 2, 4 and 6 $\mathrm{mW \cdot m^{-2} \cdot sr^{-1}}$ were used (see fig. 2.2). The distribution of the number of pixels which have different intensities (bin size by intensity was 0.05 $\mathrm{mW \cdot m^{-2} \cdot sr^{-1}}$) were calculated, and the approximation by the Poisson function

$$P(x;\lambda) = \frac{\lambda^x e^{-\lambda}}{x!}$$

was done.

For the approximation the following function was used:

$$P(x;\lambda;\Delta x;x_s;a) = a\frac{e^{-x_s\lambda}(x_s\lambda)^{x_s(x-\Delta x)}}{\Gamma(x_s(x-\Delta x)+1)},$$

where λ is the mean value of the Poisson distribution, Δx is the displacement, and x_s is the scale.

Examples of this approximation for three images are shown separately for FCC00968 (fig. 2.3), FCC01468 (fig. 2.4) and FCC01880 (fig. 2.5). It is seen that low-level noises in HMC images indeed could be fitted by Poisson PDF function.

Results of this approximation for all such images are shown in table B.1 and overview of the displacements is given in fig. 2.6. For many images the difference between λ and Δx is larger than several $\mathrm{mW\cdot m^{-2}\cdot sr^{-1}}$ (see table B.1 and fig. 2.6). Results for $I_{max} \leq 6\,\mathrm{mW\cdot m^{-2}\cdot sr^{-1}}$ seem to be most reliable because often the maximum of the Poisson PDF is found at values larger than $4\,\mathrm{mW\cdot m^{-2}\cdot sr^{-1}}$ and in majority cases larger than $2\,\mathrm{mW\cdot m^{-2}\cdot sr^{-1}}$. Absence of the maximum naturally makes fitting uncertain. In some images very low values of brightness are not fitted good by the Poisson function (see numbers of images marked by symbols in table B.1).

The actual signal above the nightside of the nucleus is very low and we may have statistical noise producing negative numbers, especially the blue images taken a long time before closest approach, the signal on the nightside from the nucleus will be close to zero at these points. However, in orange and red there should be non-zero levels with a fairly uniform distribution in pixels values about the mean (not perfectly but close enough). Again the signal is low but not completely negligible. The procedure of the dark current subtraction was very complicated [8]. In the first months of the cruise phase, images of test or calibration objects were taken with shutter in order to provide an accurate dark image for subtraction from the image of the object. However, the images of the shutter were not useful as dark images because shutter images were read out of the CCD immediately, whereas images taken through filters would wait on the CCD while the filter wheel moved to the shutter position before read-out would commence. During this "wait time", dark charge would build up on the CCD. The wait time depended upon the position of the filter used with respect to the shutter. The operating temperatures for many of the calibration images and for the encounter were at least $10-15\,^{\circ}\mathrm{C}$ above the design temperature. The dark charge generated at these temperatures (around $-5\,^{\circ}\mathrm{C}$ at encounter) was a severe problem when analysing the data. Furthermore, dark images taken before the night of the encounter are difficult to use because the temperature varied considerably during operations and from one operation period to another. As a result, two other techniques were devised to help to reduce the data [8].

Considering the difficulty with the dark subtraction, the distribution of digital number (table B.1) actually looks quite good: for $I_{max} = 6\,\mathrm{mW\cdot m^{-2}\cdot sr^{-1}}$ only 1 image has $(\lambda+\Delta x)$ more than $10\,\mathrm{mW\cdot m^{-2}\cdot sr^{-1}}$, 14 images show displacement of more than $5\,\mathrm{mW\cdot m^{-2}\cdot sr^{-1}}$. So, the most of the images have $(\lambda+\Delta x)$ less than $5\,\mathrm{mW\cdot m^{-2}\cdot sr^{-1}}$ (see fig. 2.6) and can be used for our tasks. Images with large shifts of the centre of the Poisson distribution (see $(\lambda+\Delta x)$ in table B.1) need to be avoided when doing search for faint particles, since it would be impossible to retrieve particle parameters from them with reliable accuracy.

2.4. Image restoration using the point spread function (PSF)

For the main purposes of the planned research the "cleaned" and geometrically rectified data are not suitable because during the image transformation irreversible changes took place, *e.g.* image smoothing due to interpolation, and filtering of the images also removed possible particles as part of the noise. To improve the data using modern techniques we shall mainly work with "flight" and "radio" data archives 3 and 4 (choosing the level of processing in accordance to the

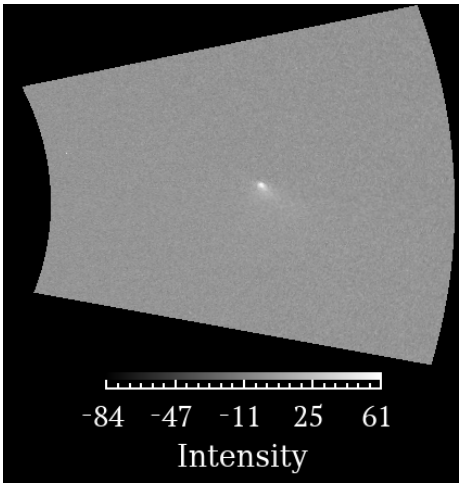

(a) FCC00968.00G.

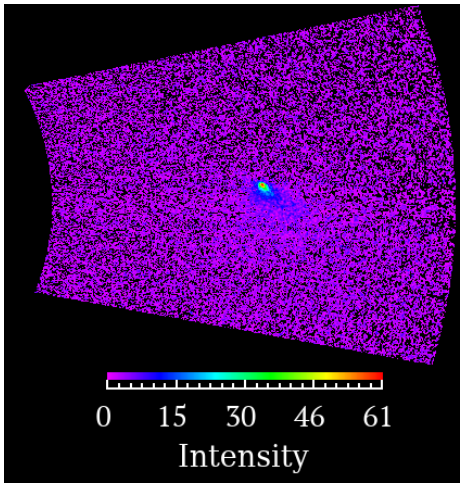

(b) FCC00968.00G.

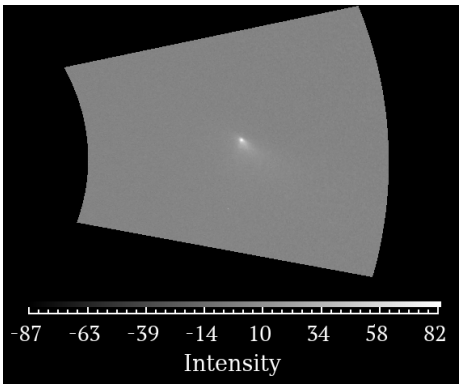

(c) FCC01468.00G.

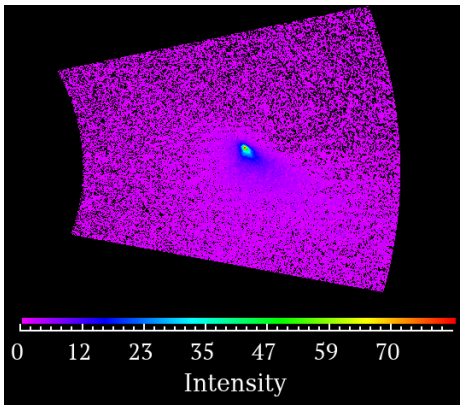

(d) FCC01468.00G.

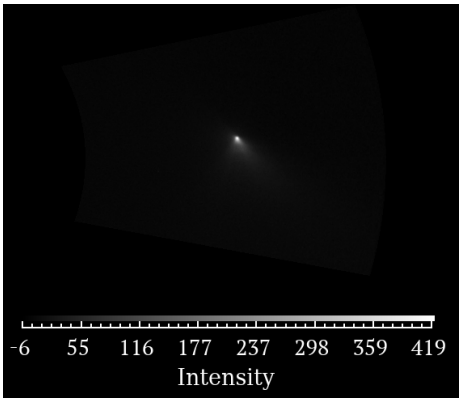

(e) FCC01880.00G.

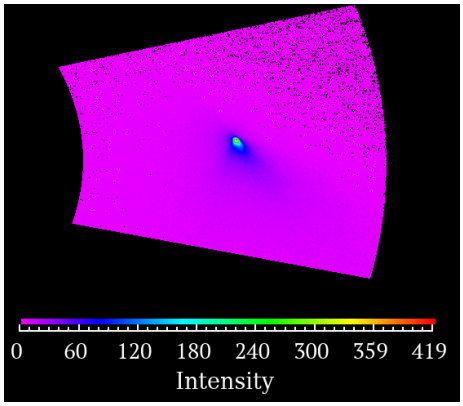

(f) FCC01880.00G.

Figure 2.1.: Examples of images which have negative values of the background signal. In the left images (figs. 2.1a, 2.1c and 2.1e) all values are shown, in the right ones (figs. 2.1b, 2.1d and 2.1f) the images show by colour the distribution of positive values of the signal (the scale starts from zero), and the negative values are shown as black pixels.

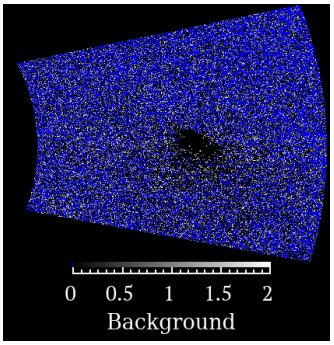

(a) FCC00968. $I_{max} = 2\,\mathrm{mW} \cdot \mathrm{m}^{-2} \cdot \mathrm{sr}^{-1}$.

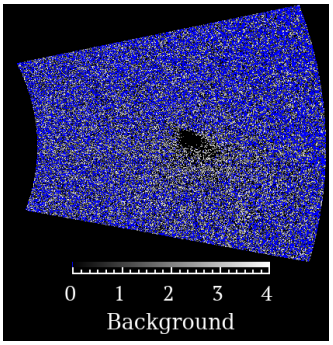

(b) FCC00968. $I_{max} = 4\,\mathrm{mW} \cdot \mathrm{m}^{-2} \cdot \mathrm{sr}^{-1}$.

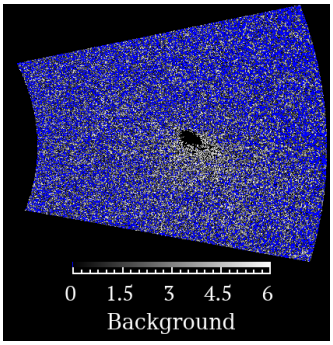

(c) FCC00968. $I_{max} = 6\,\mathrm{mW} \cdot \mathrm{m}^{-2} \cdot \mathrm{sr}^{-1}$.

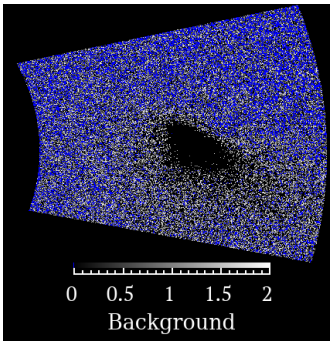

(d) FCC01468. $I_{max} = 2\,\mathrm{mW} \cdot \mathrm{m}^{-2} \cdot \mathrm{sr}^{-1}$.

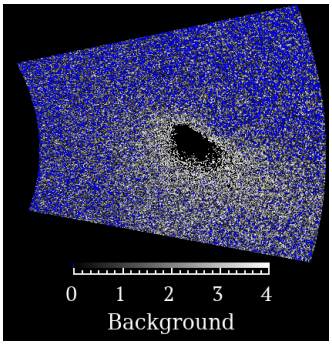

(e) FCC01468. $I_{max} = 4\,\mathrm{mW} \cdot \mathrm{m}^{-2} \cdot \mathrm{sr}^{-1}$.

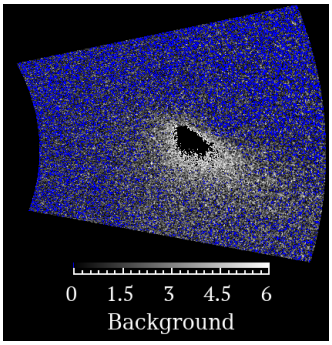

(f) FCC01468. $I_{max} = 6\,\mathrm{mW} \cdot \mathrm{m}^{-2} \cdot \mathrm{sr}^{-1}$.

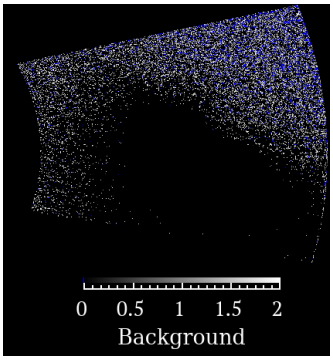

(g) FCC01880. $I_{max} = 2\,\mathrm{mW} \cdot \mathrm{m}^{-2} \cdot \mathrm{sr}^{-1}$.

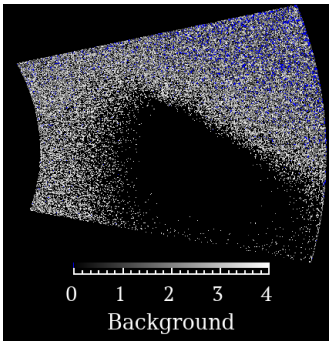

(h) FCC01880. $I_{max} = 4\,\mathrm{mW} \cdot \mathrm{m}^{-2} \cdot \mathrm{sr}^{-1}$.

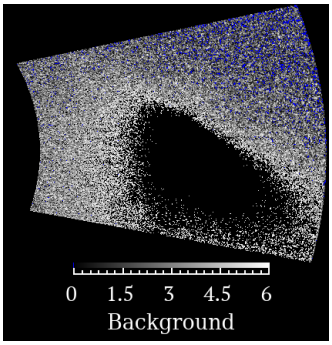

(i) FCC01880. $I_{max} = 6\,\mathrm{mW} \cdot \mathrm{m}^{-2} \cdot \mathrm{sr}^{-1}$.

Figure 2.2.: Only brightness values lower than 2, 4 and 6 $\mathrm{mW} \cdot \mathrm{m}^{-2} \cdot \mathrm{sr}^{-1}$ at fig. 2.1 are shown. Blue colour specifies the places where the negative values are placed, while the positive values are shown in grey scale. Image names are noted.

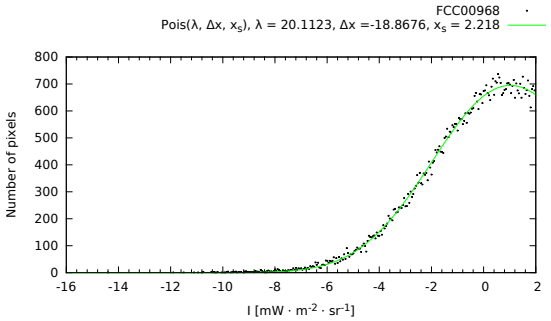

(a) $I_{max} = 2\,\mathrm{mW} \cdot \mathrm{m}^{-2} \cdot \mathrm{sr}^{-1}$.

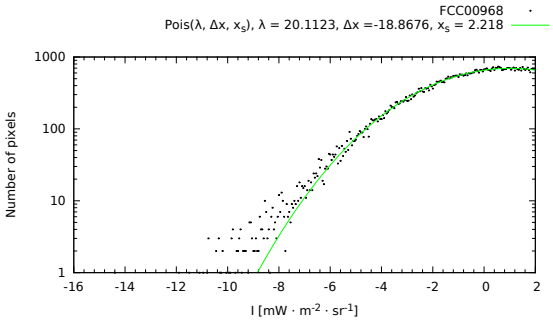

(b) $I_{max} = 2\,\mathrm{mW} \cdot \mathrm{m}^{-2} \cdot \mathrm{sr}^{-1}$.

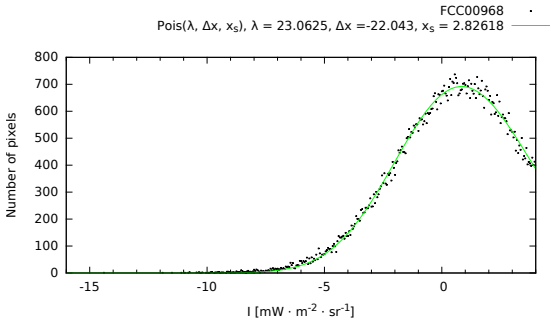

(c) $I_{max} = 4\,\mathrm{mW} \cdot \mathrm{m}^{-2} \cdot \mathrm{sr}^{-1}$.

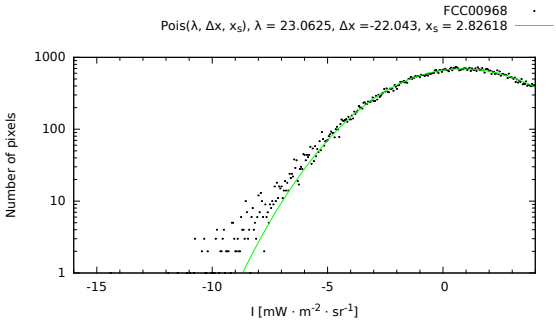

(d) $I_{max} = 4\,\mathrm{mW} \cdot \mathrm{m}^{-2} \cdot \mathrm{sr}^{-1}$.

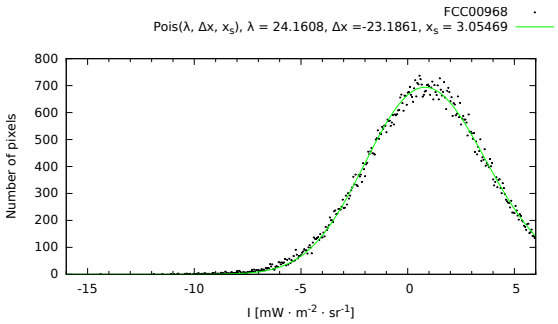

(e) $I_{max} = 6\,\mathrm{mW} \cdot \mathrm{m}^{-2} \cdot \mathrm{sr}^{-1}$.

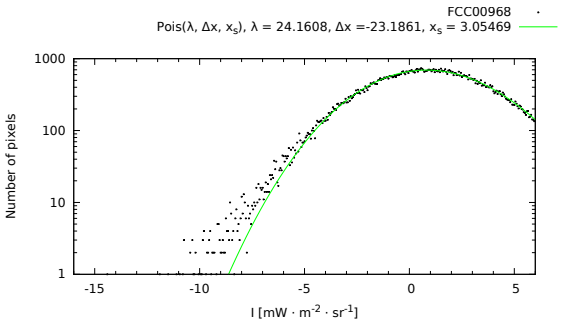

(f) $I_{max} = 6\,\mathrm{mW} \cdot \mathrm{m}^{-2} \cdot \mathrm{sr}^{-1}$.

Figure 2.3.: Approximation of the data by the Poisson PDF (green line) (figs. 2.2a to 2.2c) obtained from the image **FCC00968**. In the left panel the Y axis is linear, while in the right one the same is plotted with a logarithmic axis.

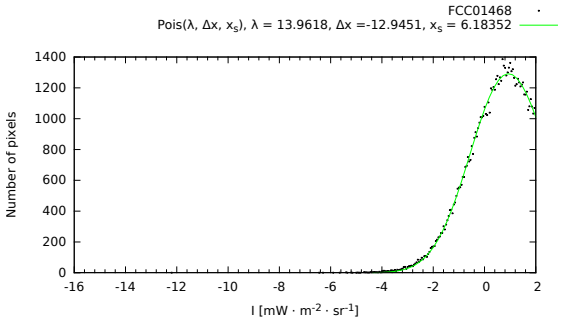

(a) $I_{max} = 2\,\mathrm{mW} \cdot \mathrm{m}^{-2} \cdot \mathrm{sr}^{-1}$.

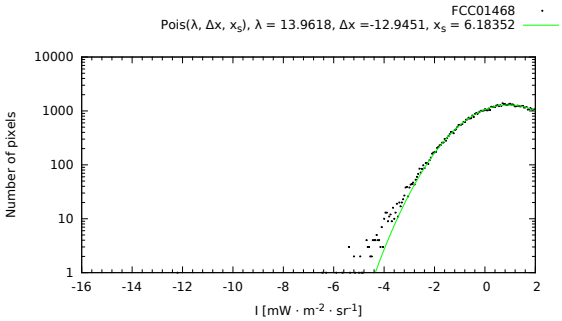

(b) $I_{max} = 2\,\mathrm{mW} \cdot \mathrm{m}^{-2} \cdot \mathrm{sr}^{-1}$.

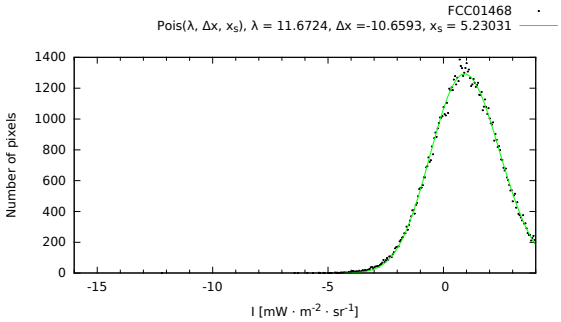

(c) $I_{max} = 4\,\mathrm{mW} \cdot \mathrm{m}^{-2} \cdot \mathrm{sr}^{-1}$.

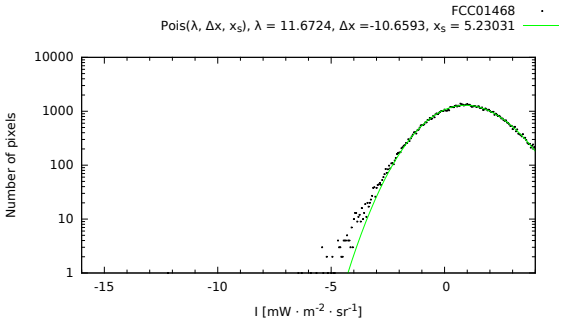

(d) $I_{max} = 4\,\mathrm{mW} \cdot \mathrm{m}^{-2} \cdot \mathrm{sr}^{-1}$.

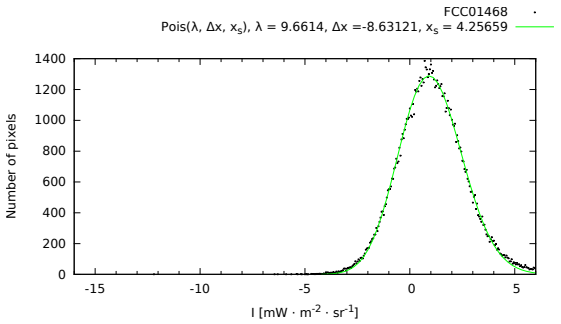

(e) $I_{max} = 6\,\mathrm{mW} \cdot \mathrm{m}^{-2} \cdot \mathrm{sr}^{-1}$.

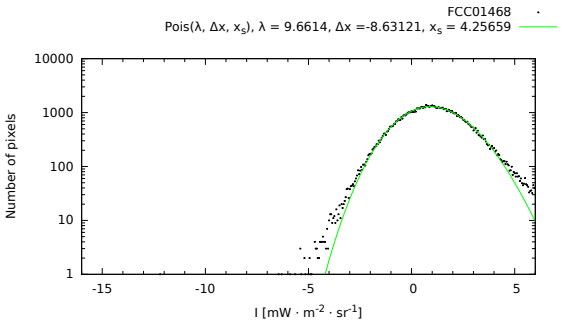

(f) $I_{max} = 6\,\mathrm{mW} \cdot \mathrm{m}^{-2} \cdot \mathrm{sr}^{-1}$.

Figure 2.4.: Approximation of the data by the Poisson PDF (green line) (figs. 2.2d to 2.2f) obtained from the image **FCC01468**. In the left panel the Y axis is linear, while in the right one the same is plotted with a logarithmic axis.

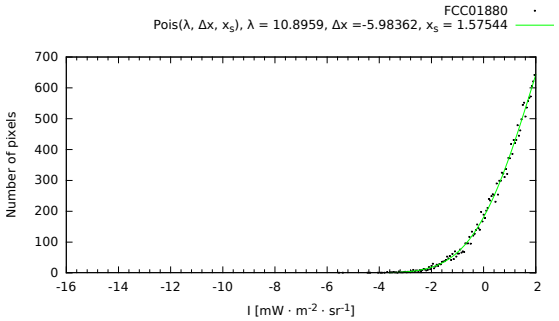

(a) $I_{max} = 2\,\mathrm{mW} \cdot \mathrm{m}^{-2} \cdot \mathrm{sr}^{-1}$.

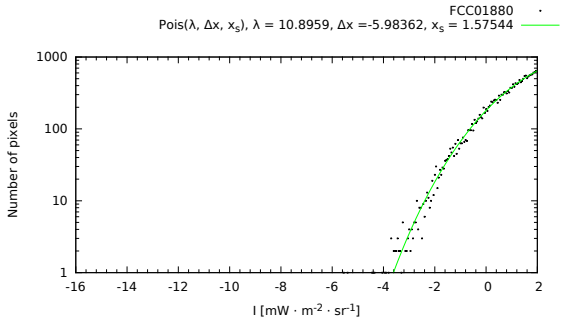

(b) $I_{max} = 2\,\mathrm{mW} \cdot \mathrm{m}^{-2} \cdot \mathrm{sr}^{-1}$.

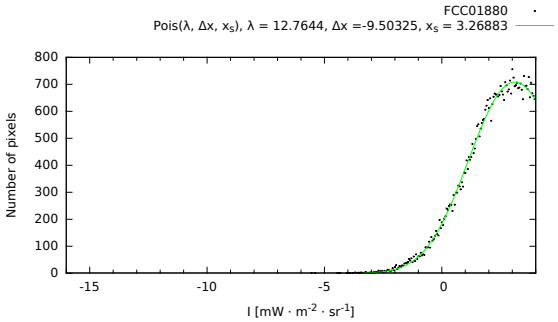

(c) $I_{max} = 4\,\mathrm{mW} \cdot \mathrm{m}^{-2} \cdot \mathrm{sr}^{-1}$.

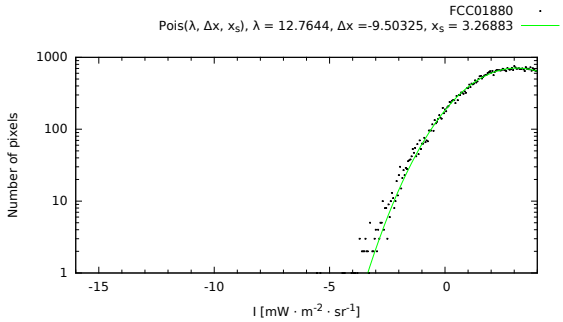

(d) $I_{max} = 4\,\mathrm{mW} \cdot \mathrm{m}^{-2} \cdot \mathrm{sr}^{-1}$.

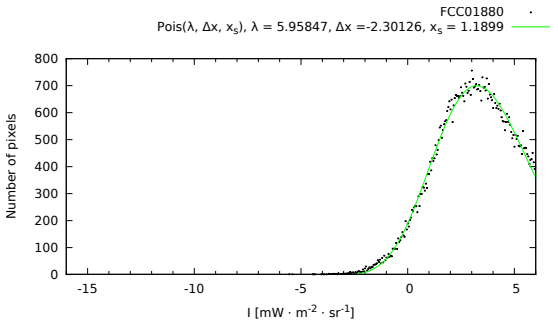

(e) $I_{max} = 6\,\mathrm{mW} \cdot \mathrm{m}^{-2} \cdot \mathrm{sr}^{-1}$.

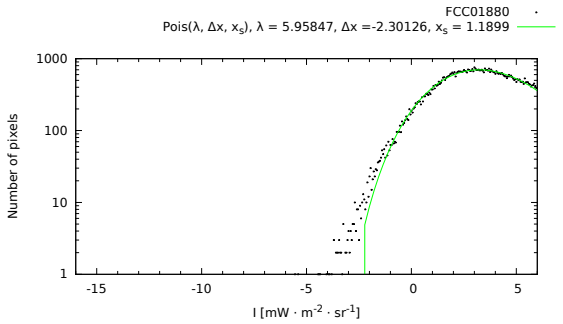

(f) $I_{max} = 6\,\mathrm{mW} \cdot \mathrm{m}^{-2} \cdot \mathrm{sr}^{-1}$.

Figure 2.5.: Approximation of the data by the Poisson PDF (green line) (figs. 2.2g to 2.2i) obtained from the image **FCC01880**. In the left panel the Y axis is linear, while in the right one the same is plotted with a logarithmic axis.

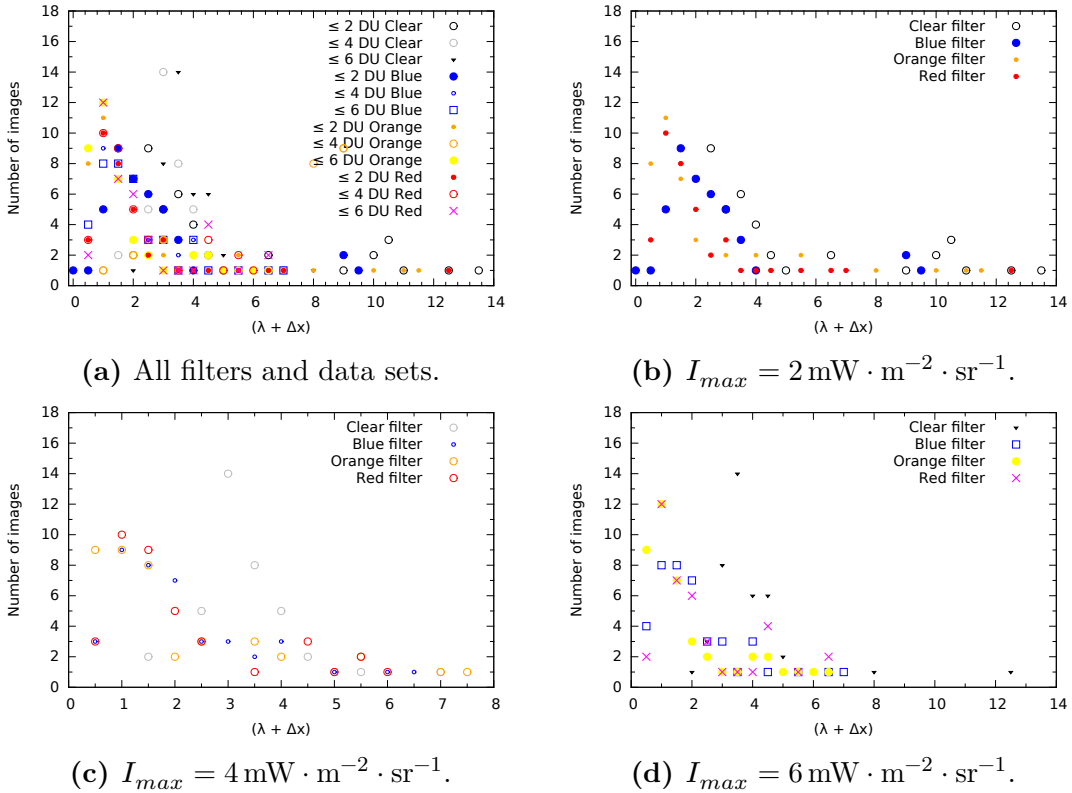

(a) All filters and data sets. **(b)** $I_{max} = 2\,\mathrm{mW} \cdot \mathrm{m}^{-2} \cdot \mathrm{sr}^{-1}$.

(c) $I_{max} = 4\,\mathrm{mW} \cdot \mathrm{m}^{-2} \cdot \mathrm{sr}^{-1}$. **(d)** $I_{max} = 6\,\mathrm{mW} \cdot \mathrm{m}^{-2} \cdot \mathrm{sr}^{-1}$.

Figure 2.6.: Amount of images with specified values of $(\lambda + \Delta x)$ obtained in four filters (clear, blue, orange, and red) for 3 signal limitations: 2, 4 and $6\,\mathrm{mW} \cdot \mathrm{m}^{-2} \cdot \mathrm{sr}^{-1}$. Bin size is 0.5 $\mathrm{mW} \cdot \mathrm{m}^{-2} \cdot \mathrm{sr}^{-1}$.

task), and process them, but shall take into account useful information about the geometrical distortion and signal distribution which is contained in geometrically rectified data.

2.4.1. Point spread function

The optical resolution of HMC is limited by its finite aperture, by minute mechanical degradations within the instrument, and by the high speed time delay and integration (TDI) illumination method adapted to the spin of the spacecraft [8, 9]. The sum of all results in a visible loss of image sharpness. The resolution of images and contrast can be improved by applying the deduced point spread function. The smearing effect has been calibrated using images of stars which can be considered as a point source. The Altair images obtained on Feb. 11, 1986 were used to determine the PSF for the image restoration [9]. This PSF was applied to the cometary dataset which is stored as "geometrical corrected" data. Unfortunately, it is not possible to get this function in a digital form now due to technical reasons (datafile is not readable any more), moreover, as it was mentioned above in section 2.2, there are no available images of Altair. It is required to use a PSF in the image analysis, and it is surely needed for improving the dataset.

However, not only Altair can be used for obtaining the PSF. There are observations of stars which were performed before the Altair observations (see [10, 11]). Using these data another PSF was obtained (see Ref. [10] and fig. 2.7). For obtaining the PSF from the Altair images they were superimposed after centering in the frequency domain with subpixel accuracy (see details in [9]), which was more accurate than that was done before in Ref. [10]. As the next step we plan to apply the method described in Ref. [9] to the other star images and study in detail the influence of the data selection and applied techniques on the resulting PSF.

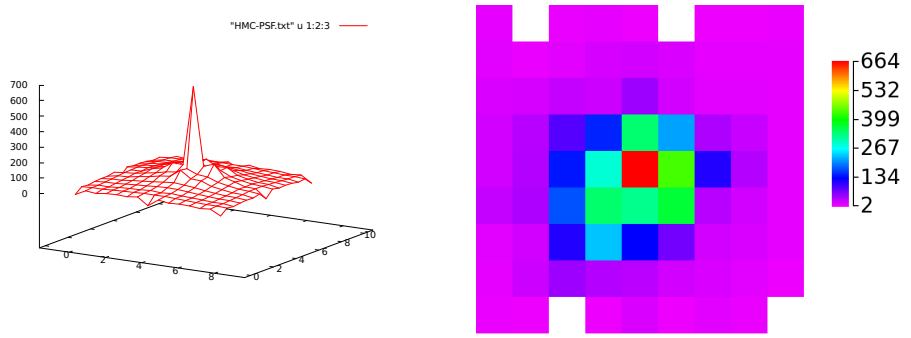

(a) Surface plot of the HMC point spread function determined by superimposing images of five stars.

(b) PSF image of function showed in fig. 2.7a. It is shown to demonstrate the asymmetry of the function.

Figure 2.7.: HMC point spread function from star observations on sensor C with clear filter.

2.4.2. Improving the restoration

Image restoration is a process in which one should be careful with noise. So, the result of applying the PSF to the image restoration depends also on the used method. In Ref. [9] the PSF was applied to the images using simple deconvolution implemented via Fourier transform. The weakness of such technique is that it "restores" the noise too. Many other methods were elaborated which were successfully used for the restoration of the Hubble Space Telescope (HST) data (see *e.g.* Ref. [12]). One of the popular methods most widely used for restoring HST images which gives good results is the Richardson-Lucy (RL) algorithm [13, 14].

The standard RL algorithm has a number of characteristics that make it well-suited:

- The RL iteration converges to the maximum likelihood solution for Poisson statistics in the data [15], which is appropriate for optical data with noise from counting statistics.
- The RL method forces the restored image to be non-negative and conserves flux both globally and locally at each iteration. This means that even if one stops the iteration before it has converged, the restored image has good photometric linearity.
- The restored images are robust against small errors in the PSF.
- Typical RL restorations require a manageable amount of computer time, representing a reasonable compromise between quick (but often unsatisfactory) methods such as Wiener filtering and the much slower (though sometimes superior) Maximum Entropy Method (ME).

We have used the RL method to test how it works with the HMC data. The PSF obtained in Ref. [10] was used (see fig. 2.7). As a test the image of the Earth obtained by HMC on Oct. 18, 1985 was used because we can compare the HMC image after the restoration with the images of the Earth which were obtained at the same time by two satellites (see fig. 2.8e and [10]). So we can decide whether the details obtained after the restoration and seen on the Earth image are real, or not. Also the results of deconvolution of the same HMC image which were obtain using the PSF obtained from Altair images and Fourier transform are shown for comparison (see fig. 2.8c).

Although the image of the Earth obtained by GMS-3 (fig. 2.8e) is not exactly in the same position as the HMC image, one can see in fig. 2.8 the effectiveness of the applied method of image restoration: details which are seen in the fig. 2.8e are distinctly seen in fig. 2.8b while in the raw image (fig. 2.8a) they were smoothed. This is an indication that such methods work not worse

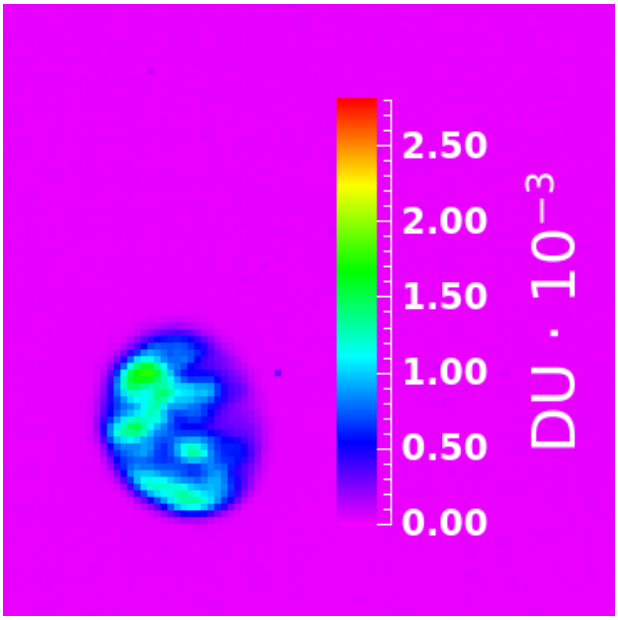

(a) The unprocessed Earth image foc01621x taken at distance of 20.09 million km on 18 October 1985 5:19 UT.

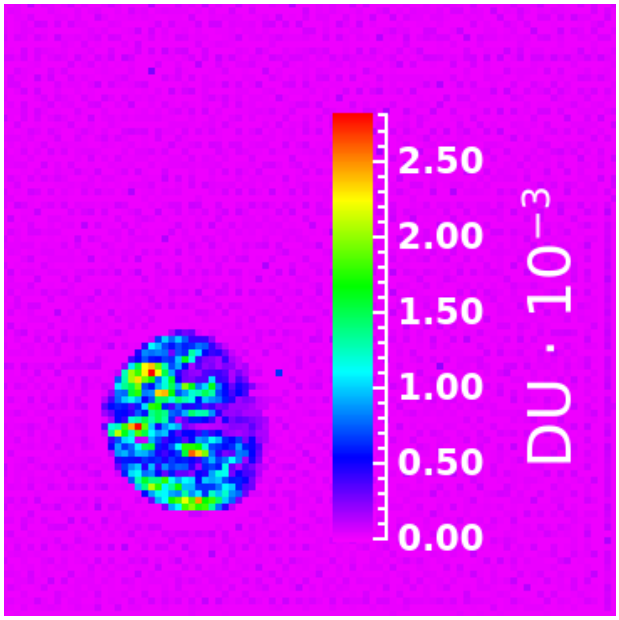

(b) PSF processed image shown at fig. 2.8a. Richardson-Lucy restoration.

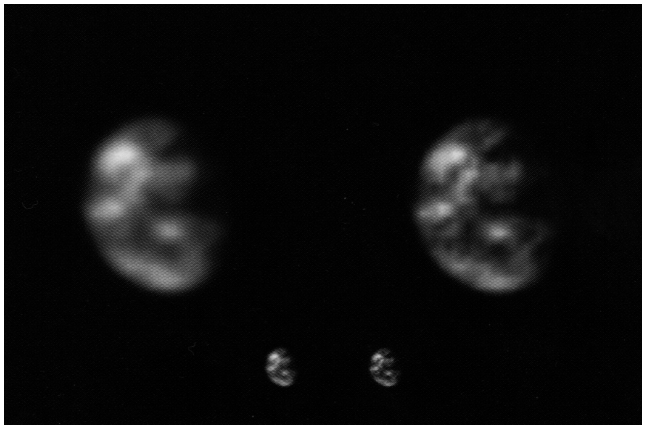

(c) The same HMC image as in fig. 2.8a; unprocessed data (left) and PSF processed (right). Image from Ref. [8].

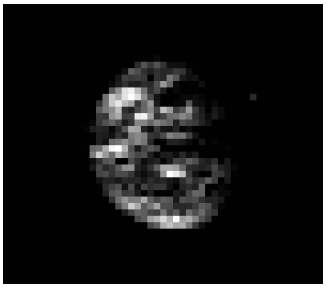

(d) The same HMC image as in fig. 2.8b but in gray scale. RL method.

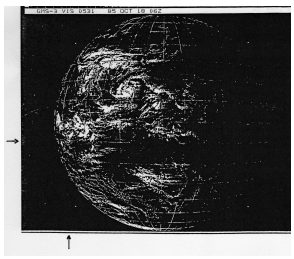

(e) Earth as seen from the satellite GMS-3 [10] at the same time as HMC.

Figure 2.8.: Example of the Earth image RL restoration with the PSF (see fig. 2.7). For comparison of the visibility of the details (clouds) the Earth image obtained from the Japanese meteorological Earth satellite GMS-3 is shown in fig. 2.8e. The Giotto spacecraft and GMS-3 were on the same meridian near 05:20 UTC. The GMS-3 image thus approximately shows the portion of the Earth observed by HMC (Courtesy Meteorological Satellite Centre, Tokyo). The result of Earth image's restoration made in fig. 2.8c is shown for comparison with the results of RL restoration.

than the direct deconvolution method used before (compare fig. 2.8d with fig. 2.8c). We plan to study the RL method with comet images, as well as expectation-maximization algorithms, to find the best suited one for the HMC data.

3. Estimations of the detection possibility of comet particles' by HMC

3.1. Definition of the parameters

$F_{\odot}$ flux from the Sun [$\mathrm{W} \cdot \mathrm{m}^{-2}$];

a reflectance of the particle [dimensionless];

r particle's radius [m];

l distance between the camera and particle [m];

S geometrical cross-section [m^2];

i_{FOV} field of view (FOV) of a pixel [rad];

Ω_p solid angle in which the particle is visible from the camera;

Ω_C solid angle in which camera is visible from the particle;

Ω_i solid angle which one pixel cut on coelosphere;

TDI_{lines} the number of TDI lines. It has been optimized for constant output signals for the appropriate filter bands taking into account the resolution requirements. For detectors the values of TDI_{lines} are [16]: **B** 6 px, **C** 6 px, **D** 8 px, **E** 4 px;

τ_1 exposure time for a single line;

τ total exposure time for a slit $\tau = TDI_{lines} \cdot \tau_1$;

SNR signal to noise ratio.

3.2. General considerations

Here we consider a particle in the best detectable geometry, *i.e.* normal incidence ($\mu_0 = 0$). Consider a reflectance coefficient of a particle of

$$a = \frac{\pi I}{F_{\odot}}. \tag{3.1}$$

Therefore, from the whole particle the radiant intensity:

$$I_p = \frac{F_{\odot} a S_p}{\pi}. \tag{3.2}$$

If the particle is observed by a telescope, the latter is visible from the particle with a solid angle Ω_C and receives a radiant flux of

$$\Phi_C = I_p \Omega_C.$$

At a given time the particle is visible from the camera with a solid angle Ω_p. Then, given the field of view of a pixel (i_{FOV} and corresponding solid angle Ω_i), the image of a particle occupies N^0_{pix} pixels

$$N^0_{pix} \approx \max\left(1, \frac{\Omega_p}{\Omega_i}\right). \tag{3.3}$$

If the particle moves during imaging, the image might be smeared and occupy more pixels. Here we neglect the radial (with respect to the camera) component of the speed vector and account for tangential velocity only.

Table 3.1.: Estimations of smearing velocities ($v_{1_\perp}$ and $v_{2_\perp}$, see eqs. (3.4) and (3.5)) for different sizes of particles (r) at different distances (l).

TDI_{lines}	τ_1 [s]	r [m]	$l \cdot 10^3$[m]	$v_{1_\perp}$ [m · s^{-1}]	$v_{2_\perp}$ [m · s^{-1}]
6	$14.2 \cdot 10^{-6}$	1	1	263	23474
6	$14.2 \cdot 10^{-6}$	10	10	2629	234741
6	0.001	0.01	1	3.73	3.33
8	$14.2 \cdot 10^{-6}$	100	10^2	19718	1760563
8	$14.2 \cdot 10^{-6}$	0.01	1	197	176
8	0.001	0.01	1	2.8	2.5
4	$14.2 \cdot 10^{-6}$	100	10^2	39437	3521127
4	$14.2 \cdot 10^{-6}$	0.01	1	394	352
4	0.001	0.01	1	5.6	5

If the particle moves with velocity v_p each pixel makes a track in the field of view with length $\omega = v_p\tau/l$, where τ is the exposure time. The track will occupy ω/i_{FOV} pixels. Since all of the tracks are straight lines we can write that the total number of occupied pixels $N_{pix} = N^0_{pix} + N^v_{pix}$, where

$$N^v_{pix} = \frac{v_p\tau}{l \cdot i_{FOV}}.$$

3.3. HMC imaging mode

HMC was taking images in the so-called TDI mode [16]. In this mode only a thin part of the 2D CCD detector was uncovered, and vertical scan-out was provided by the spacecraft (and therefore the camera) spinning. During this spinning charges were transferred line-by-line in the same direction. In case of HMC, the slit was made wider than 1 px (see TDI_{lines}), which increases exposure time but degrades the sharpness to some extent. Since pixels of the CCD are square [8, page 25], the smearing in both directions will be the same.

Therefore, if the tangential velocity $v_\perp$ of the particle is

$$v_{1_\perp} > \frac{i_{FOV} \cdot l}{\tau}, \tag{3.4}$$

where τ is the exposure time in TDI mode, then there will be smearing of the particle image for more than 1 px. If, at the same time, the smearing is larger then the size of the particle image $2r/(l \cdot i_{FOV})$, then the decrease of the registered brightness is significant. Thus,

$$v_{2_\perp} > \frac{2r}{\tau} \tag{3.5}$$

would decrease the signal by a factor of two (see table 3.1). Once a particle is detected and parameters of its movement are obtained, its smeared image can be restored and the signal can be increased.

If the response of the camera is stronger than the background noise, this signal (and thus the particle) may be detected. Let $I > I_{bg} \cdot SNR$ be the condition for detection.

Particles are expected to have speeds of $\sim 0-100\,\mathrm{m \cdot s^{-1}}$ at closest approach (where the exposure time $\tau_1 = 14.2\,\mathrm{s}$). Figure 3.1 illustrates the estimations of the critical velocities for the particles. As it can be seen from table 3.1 and fig. 3.1 the particles near the comet will be observed as unmovable objects.

3.4. Visibility and detectability of particles

Each pixel from the particle's image gets energy per time unit of

$$B = \frac{\Phi_C}{N_{pix}}. \tag{3.6}$$

Since the camera is calibrated in $\mathrm{W} \cdot \mathrm{m}^{-2} \cdot \mathrm{sr}^{-1}$, let us calculate the registered radiance for those pixels on the aperture:

$$I_R = \frac{B}{S_c \Omega_i}, \tag{3.7}$$

where S_c is the cross-section of the aperture.

Now let us substitute everything in eq. (3.7).

$$I_R = \frac{M_C}{N_{pix} S_c \Omega_i} = \frac{F_{\odot} a S_p \Omega_C}{\pi (N^0_{pix} + N^v_{pix}) S_c \Omega_i} = \frac{F_{\odot} a S_p \Omega_C}{\pi \left(\max\left(1, \frac{\Omega_p}{\Omega_i}\right) + \frac{v_p \tau}{l \cdot i_{FOV}} \right) S_c \Omega_i} \tag{3.8}$$

The condition of detectability is:

$$I_R \geq I_{bg} \cdot SNR,$$

where I_{bg} is the mean intensity of the image background (including noises), and SNR is the target signal to noise ratio.

Consider the particle's cross-section S_p. Let us assume that it depends on the particle radius r as $S_p = k_s r^x$ (for a compact particle $x = 2$, k_s is dimensionless and is equal to π, for very fluffy $x = 3$). Hereafter we focus on the case of compact particles.

Let us separate eq. (3.8) into 2 cases: when the radius of the particle is less and more than 1 pixel, respectively

$$I_R = I_{bg} \cdot SNR = \begin{cases} \frac{F_{\odot} a S_p \Omega_C}{\pi S_c \Omega_i \left(1 + \frac{v_p \tau}{l \cdot i_{FOV}}\right)}, \text{if } \frac{\Omega_p}{\Omega_i} < 1 \\ \\ \frac{F_{\odot} a S_p \Omega_C}{\pi S_c \Omega_i \left(\frac{\Omega_p}{\Omega_i} + \frac{v_p \tau}{l \cdot i_{FOV}}\right)}, \text{if } \frac{\Omega_p}{\Omega_i} \geq 1 \end{cases}.$$

Assuming that $S_p = \pi r^2$, $S_c = \pi D^2/4$, $\Omega_p = \pi r^2 / l^2$, and $\Omega_C = \pi D^2/(4l^2)$:

$$I_R = I_{bg} \cdot SNR = \begin{cases} \frac{F_{\odot} a r^2}{l^2 i^2_{FOV} \left(1 + \frac{v_p \tau}{l \cdot i_{FOV}}\right)}, \text{if } \frac{\pi r^2}{l^2 i^2_{FOV}} < 1 \\ \\ \frac{F_{\odot} a r^2}{\pi r^2 + i_{FOV} l v_p \tau}, \text{if } \frac{\pi r^2}{l^2 i^2_{FOV}} \geq 1 \end{cases}. \tag{3.9}$$

Thus the critical value of r is:

$$r = \begin{cases} l \cdot i_{FOV} \sqrt{\frac{I_{bg} \cdot SNR \cdot \left(1 + \frac{v_p \tau}{l \cdot i_{FOV}}\right)}{F_{\odot} a}}, & \text{if } \frac{\sqrt{\pi} \cdot r_0}{l \cdot i_{FOV}} < 1; \\ \\ \sqrt{\frac{l \cdot i_{FOV} v_p \tau}{F_{\odot} a / (I_{bg} \cdot SNR) - \pi}}, v_p \neq 0, & \text{if } \frac{\sqrt{\pi} \cdot r_0}{l \cdot i_{FOV}} \geq 1. \end{cases} \tag{3.10}$$

Here r_0 is defined in the sense of eq. (3.3), *i.e.* for non-moving particles.

When the particle does not move and its image is resolved, the intensity from it is constant and equal to

$$I_R = \frac{F_{\odot} a}{\pi}, \tag{3.11}$$

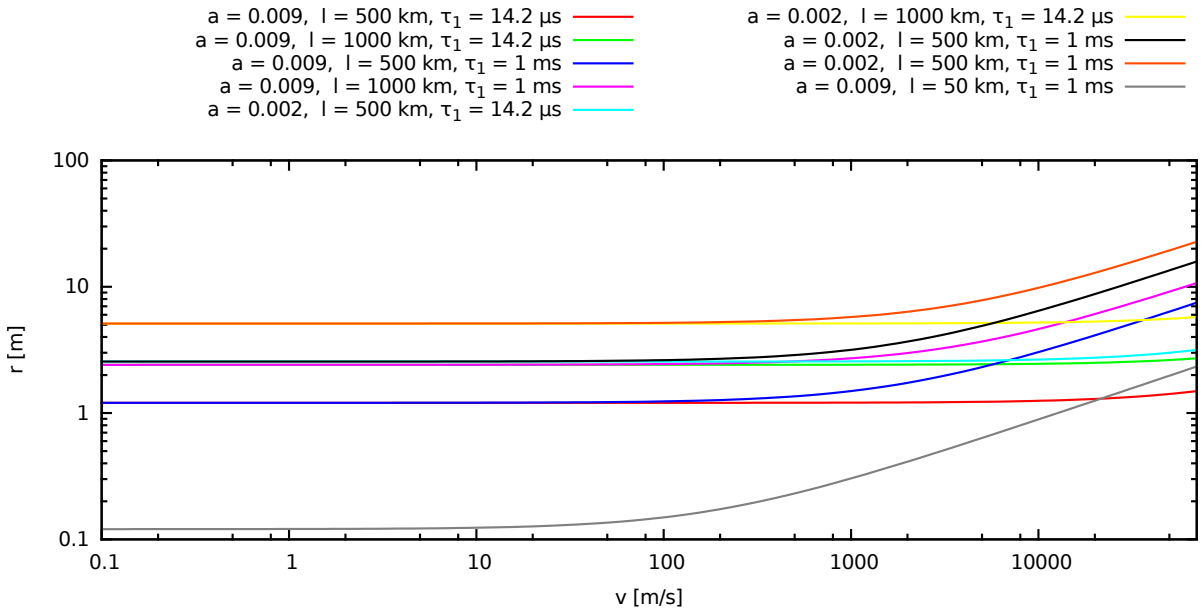

Figure 3.1.: Influence of tangential speed of the particle on its visibility for the camera (see eq. (3.10) and values of parameters noted above plot; different cases are marked by different colours). Distance from the camera to particle is varied from the closest encounter with the nucleus (500 km) up to 1000 km, special case of 50 km, *i.e.* a particle that flew far away from the nucleus, is also considered; two kinds of particles are shown: bright (reflectance $a = 0.009$), and dark ($a = 0.002$); variation of exposure time τ_1: 14.2 s (the shortest exposure for camera) and 1 ms (the longest one); $TDI_{lines} = 6$. $SNR = 1.5$.

i.e. is determined by its reflectance only (according to our assumption in eq. (3.1)).

Assuming a mean value of the background of $50\,\mathrm{mW \cdot m^{-2} \cdot sr^{-1}}$ [8] and non-moving (in frame) particles, we obtain the conditions of detectability shown in fig. 3.2. It is seen that in case that we would like to detect particle close to the nucleus (where we expect to have larger concentration of particles) on the distance about 20 000 km particle should have radius about tenth of meters even if it is bright (dirty ice on the Earth has reflectance about 0.18). So, it has sense to consider the close images.

The estimations of the exact radii of particles depend on their light scattering properties. In the absence of compositional information of the large particles under search, we may assume that the particles may behave photometrically like the comet nuclei (the "dusty case"), or to be consist of the bright icy material (the "icy case"). The highest detected value of reflectivity of the nucleus through the clear filter of HMC is 0.0092 which corresponds to 16 – 20 % of geometric albedo at the phase angle of 107° [8, p. 70]. Ejected particles might have the same value of reflectivity, that gives us the smallest possible diameter of detectable particles from a distance of $\sim 500\,\mathrm{km}$ (closest encounter with the nucleus) particles $\sim 3\,\mathrm{m}$ for a $SNR = 2$, and $\sim 2\,\mathrm{m}$ for a $SNR = 1.1$. If we will consider that the particles are icy, this leads to the decreasing of diameter to centimetres. Obtained values are in accordance with the estimations made for comet 103P/Hartley 2 in [17].

However, since the camera is moving together with the spacecraft with speed of $68\,\mathrm{km \cdot s^{-1}}$ relative to the nucleus [8], some of the particles might move with respect to the camera with a speed up to this value. The influence of this on the detection capabilities is show in fig. 3.1. As it is seen from figs. 3.1 and 3.2, particles near the nucleus may be detected even if they are quite fast, but detection of particles that are ten times closer to the camera seems to be barely possible.

If ejected particle moves directly to the place where HMC will be at the time of observations,

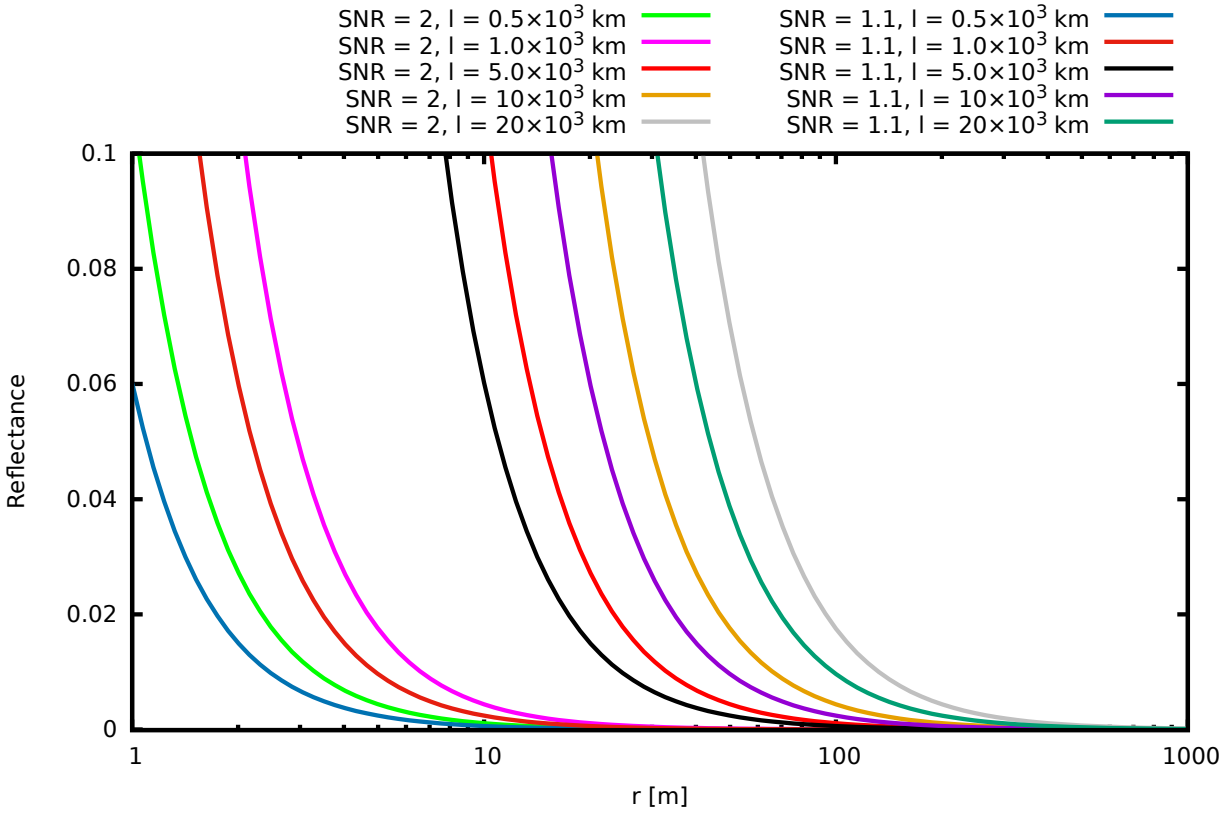

Figure 3.2.: Detectability of particles with zero tangential velocity from different distances and under various SNR values (see eq. (3.10) and values of parameters noted above plot; different cases are marked by different colours). We considered two cases of SNR: 2 (very good) and 1.1 (more realistic). Distance from the camera to particle is varied from 0.5×10^3 km (closest approach) up to 20×10^3 km, and reflectance up to the 0.1 (dirty ice on the Earth has reflectance value of about 0.18).

it can become more visible for the camera. If a particle moves with speed of at least 10 m/s, it can easily travel tens of thousand kilometres in tree month (approximate time from starting the nucleus activity to the HMC observations in March 1986). However, camera's cone of view occupies only 5×10^{-6} of the space (field of view 0.5° by 0.3° [8]), thus only small amount of particles will increase their detectability in this way. But nevertheless it is known that several particle hits the camera during the flyby [18, 19]. In this perspective it is interesting to look at the closest images in the active regions where particles might be detectable.

4. Large particle detection: general algorithm and it's implementation to HMC data

4.1. HMC data selection

As it was mentioned at the beginning (see section 2.2), there are four types of data from the processing levels "flight", "radio", "geo", and "cleaned" (see as an example fig. A.1). "Geo" images are in different projection and during transforming into this projection, single-point objects in images were distorted and thus "geo" images are not suitable for our task.

Among three available HMC datasets ("flight", "radio", and "cleaned") only the last one ("cleaned") obviously is not suitable for particles search due to specific of image filtering used to obtain it. The "flight" images are very noisy. The images from "radio" level are not so noisy because, according to [8], dark current was subtracted and cosmic events were removed (however, the dark current was retrieved in a non-straightforward, quite complex way). Statistics of noise and useful signal (faint particles at random image locations) are the same (see examples of brightness histograms for several unprocessed HMC images in fig. 4.1). Thus the only difference between possible particle images and random noise is the space coherence of the formers. Therefore, in order to be on the safe side, we've performed tests for particles in both image sets ("flight" and "radio").

It was shown above that the detection of large particles by HMC is possible in principle (see chapter 3). Thus, taking to account the estimations of particles detectability, it is reasonable for searching the particles to select the images using the following criteria:

- non-processed ("flight" level) and/or calibrated images ("radio" level) could be used;
- images obtained in multi-detector mode (MDM) shall be used. To get an idea of the MDM HMC images look, please see figs. A.2 and A.3;
- clear filter images are most suitable (because obviously in this case the registered flux of light is larger than through other filters);
- SNR for detector C images is larger than for other detectors, and size of these images is 74×74 pixels (superpixel[1] format 0), that is larger than for detectors B, D, E (37×37 pixels);
- distance from the camera to the nucleus supposed to be in the range of $20\,000 - 16\,000$ km and smaller to provide needed resolution for a detection.

The following images meet the criteria and form our working set: $3\,436 - 3\,480$ (distances from camera to nucleus are in range of $20\,000 - 8\,000$ km), and the closest images which still contain the space except nucleus itself (image numbers are $3\,480 - 3\,493$, distances from camera to nucleus are about $8\,000 - 4\,000$ km).

[1] Superpixel format (SPF) is the summation of several original pixels into one of a larger area for purpose of data compression. SPF = 0 means no data compression

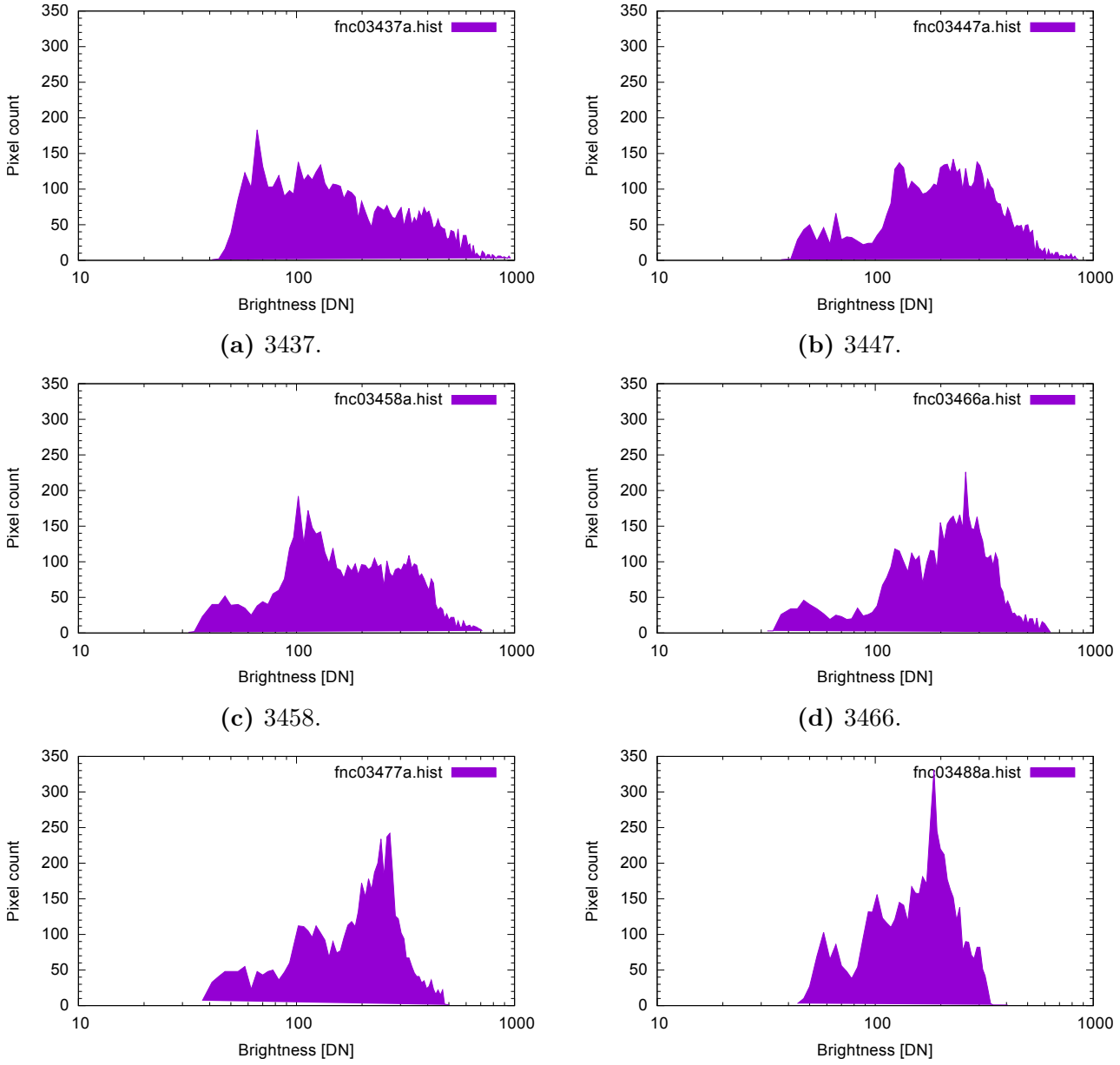

(a) 3437. **(b)** 3447.

(c) 3458. **(d)** 3466.

(e) 3477. **(f)** 3488.

Figure 4.1.: Examples of brightness histograms for several HMC images. The closer the spacecraft is to the nucleus (image number increases), the larger portion of the image frame the nucleus occupies (see figs. A.2 and A.3).

Semi-regular structure in images We would like to note that there are some regular changes of signal which are present in unprocessed images that is likely to be artificial. They are clearly seen as artificial "grid" in image of standard deviation from mean value of signal for our data set of MDM images, that showed up in almost every 16^{th} pixel (see fig. 4.2). The signal was square-root encoded and during the telemetry conversion the data were decompressed, so appearance of this pattern could not be explained by data compressing algorithm, but maybe it was caused by errors in analogue-to-digital encoder, or by the CCD design. As such, these pixels must be excluded from any analysis.

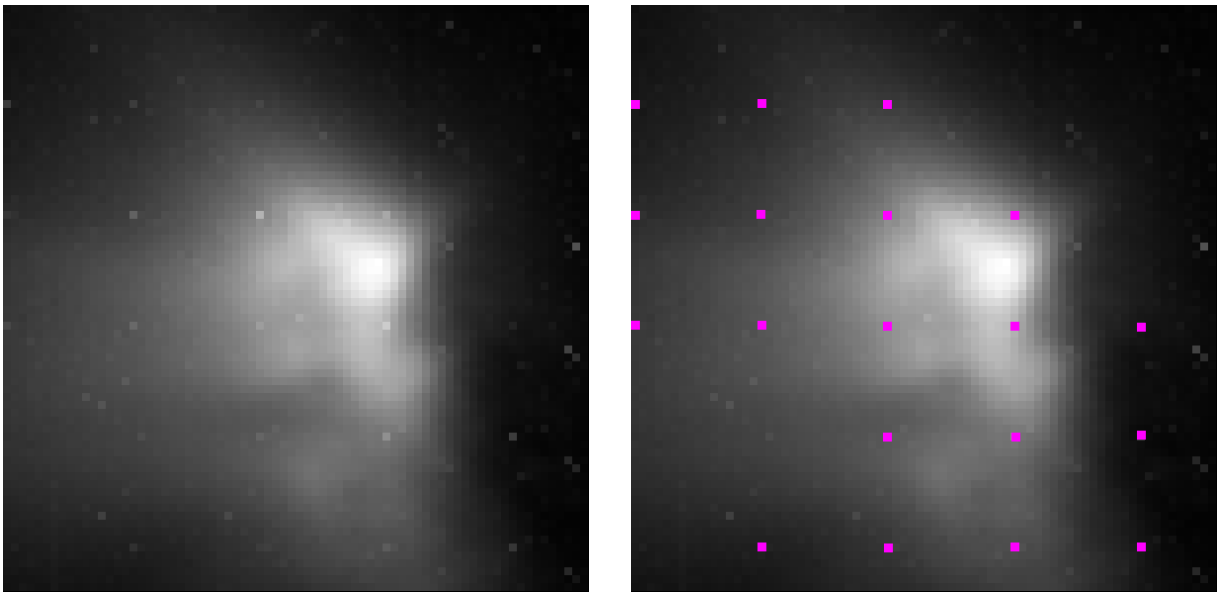

(a) Standard deviation of brightness.

(b) Standard deviation of brightness. Points are marked by magenta colour.

Figure 4.2.: Standard deviation from mean value of brightness for summarized image for MDM data set (a). Points that formed artificial "grid" are marked by magenta colour (b).

4.2. Images differencing method (IDM). Searching for the particles at superposed HMC images

To distinguish between the particles and sporadic noises in images, space coherence of the former may be used. Noise does not have such coherence. Moreover, time gaps between subsequent HMC images are so small compared to the predicted particle velocities, that their positions in consecutive images should not change much (except for the very last images, where drastic changes of viewing geometry requires special treatment, or if particle is relatively close to the camera). To compare several images, obtained at close time moments, they have to be transformed into the same coordinate system, or, in the first approximation, superposed. The last approach is easier to try, thus we started from it. Only images which do not differ significantly from each other (in sense of geometry) can be used for this. Sequence of 15 images (3 436 – 3 450) have been used. The program which superposes HMC images with decreasing step and checks the rate of the residual decrease has been developed. The Nelder-Mead method[2] was used for minimizing squares of residuals to superpose images.

[2]The Nelder-Mead method [20] is a simplex method for finding a local minimum of a function of several variables. For two variables, a simplex is a triangle, and the method is a pattern search that compares function values at the three vertices of a triangle. The worst vertex, where the value is largest, is rejected and replaced with a new vertex. A new triangle is formed and the search is continued. The simplest step is to replace the worst point with a point reflected through the centroid of the remaining N points. If this

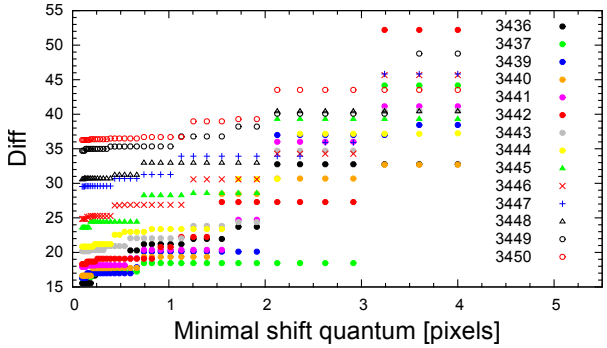

(a) $0 < B < 1\,000$ DN, including the intermediate shift quantum values.

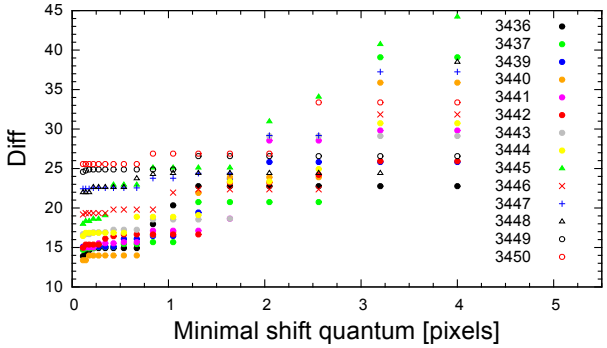

(b) $0 < B < 550$ DN.

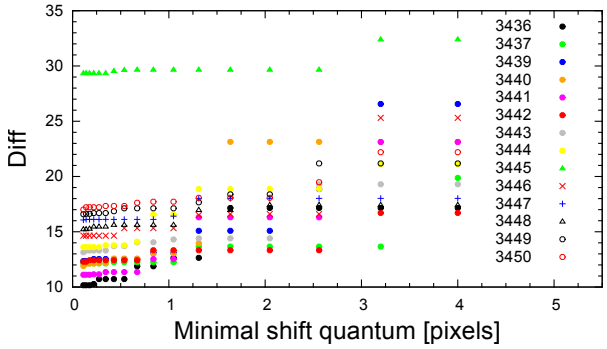

(c) $0 < B < 200$ DN (dark part).

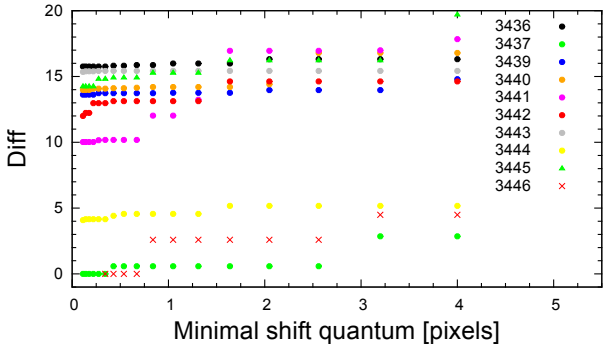

(d) $0 < B < 100$ DN (very dark).

Figure 4.3.: Precision needed to superpose the images. "Diff" is minimizing function $\sum_{i,j}(I^0_{i,j} - I_{i,j})^2$, where i, j enumerates all non-blank pixels in both images, the function that were minimized. Base image I^0 is image number 3438 (that is why it is not present). Distance to the nuclei is $\sim 20\,000$ km, MDM, detector C, clear filter. Different ranges of B are present: (a) for all brightness' values, (b),(c),(d) for the regions with marked different levels of darkness.

Using different target accuracies we can determine how alignment accuracy depends on the minimal shift quantum. It was found that the difference between the images in the selected sequence does not decreases significantly after reaching alignment accuracy of 0.25 px (see fig. 4.3). The value of shifts along the OX and OY axes are shown in fig. 4.4 for 36 minimal shift quantum values. They reflect the movement of the comet in the HMC field of view (FOV), and a jump is seen in image 3445 (see fig. A.2 and fig. 4.4). Obtained shifts are plotted in fig. 4.4 for three ranges of brightness. For some shifts quantum values shifts were found to be the same, and points in figure are overlapped in such cases. Image 3438 was used as base to which other images in sequence were aligned and that is why there is no shift for this image at fig. 4.4.

Results of automatic method of superposition were compared with results of superposing by eye using blink method[3], and they were found to be in consistency.

After superposing images, the next step for this method is comparing the consecutive ones: subtraction of images might allow us to detect moving particles, while summation can be used to detect non-moving ones. It turned out that projection in the images series changes too fast

point is better than the best current point, then we can try stretching exponentially out along this line. On the other hand, if this new point isn't much better than the previous value, then we are stepping across a valley, so we shrink the simplex towards a better point. The process generates a sequence of triangles (which might have different shapes), for which the function values at the vertices get smaller and smaller. The size of the triangles is reduced and the coordinates of the minimum point are found. This simplex surrounds a minimum and shrinks to a point. If the enough number of calculations of simplex (number of iteration) is set this optimizer surely find the local minimum

[3]Software implementation of the well-known *blink comparator* device [21]

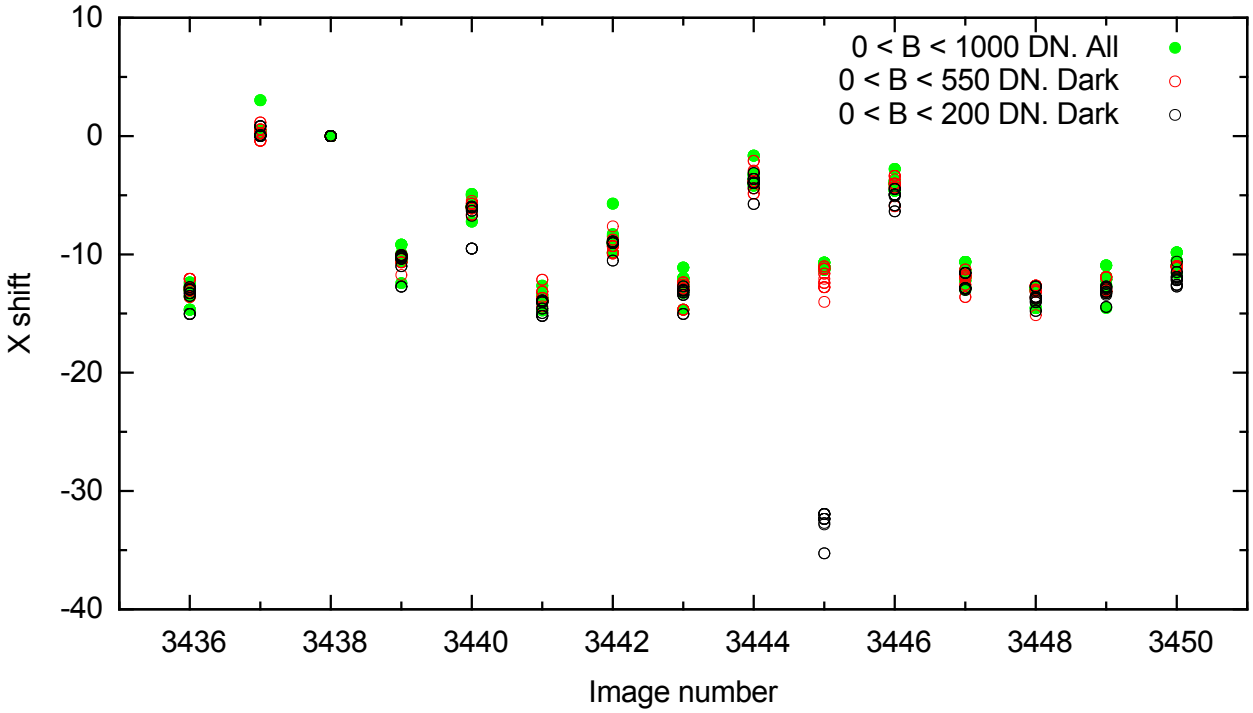

(a) Shifts along the OX axis in pixels.

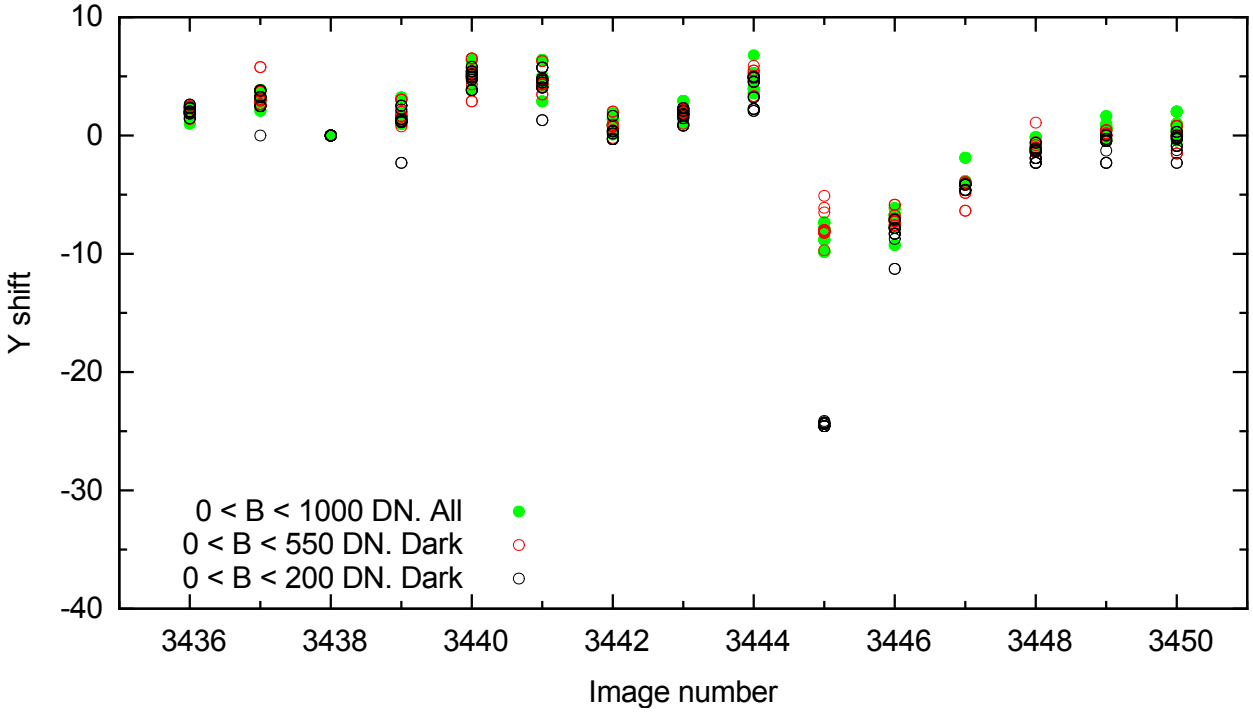

(b) Shifts along the OY axis in pixels.

Figure 4.4.: Comparison of shifts with different limitation of pixel brightness. Base image is 3438. 36 steps of changes of the minimizing function are shown for every image (starting from 4 to 0.1 with factor of 0.9). For some steps results are the same, and points in figure are overlapped in such cases.

to get long enough sequences to achieve significant SNR increase for detecting particles. The longest possible series consists of 3 images, and after that distortions become larger than 1 pixel everywhere, thus preventing particle detection. Because continuous object (the nucleus) occupies only a small part of the image, it is impossible to use methods of soft image alignment to extend the image sequences: alignment results outside of the nucleus image, where the particles are expected to be found, can not be certain. It is possible also to compare by eye the superposed images (one by one) by blinking or by creating a movie, and try to see the movements of any pixels along a straight line in it. It is obvious that this is also not an easy task. The situation is complicated by the facts that the brightness of particle can also change from image to image, and that the scale at images is changed with distance (*e.g.* see fig. A.2), so it is possible to work only with groups of images which have close geometry. Thus, this method turned out to be not very effective. Nevertheless, if even it would be possible to detect the particles in such way, it would be hard to be sure that found suspicious pixels are indeed particles, because to prove this we need to *e.g.* restore the track in space (in case of moving particle). And we can not superimpose enough images without correcting their geometry to increase SNR high enough for non-moving particles detection. The image projections could be different even between two neighbour images (this is seen from the fact that image scales are different if we look at several consequent images), and they really differ if we compare, *e.g.*, image 3 436 and 3 446 in our sequence. Of course, it is possible to search for the scaling factor together with shifts (or even the whole matrix of affine transform), but after realising the problems listed above it become evident that development and implementation of other method, which would allow to restore the 3D picture of possible particles location and/or movements, is more advanced and accurate.

4.3. Automatic method of the large particle detection (AM)

4.3.1. General algorithm

What we expect from the algorithm is the confident detection of all pixels which are probable images of a particle, which stays or moves with arbitrary speed along a straight line in space. The general scheme of the algorithm is shown in fig. 4.5. At the first step we find suspicious pixels in frames and compile lists of them for every frame. The list of frames is sorted then by time (*i.e.* by image number). For all suspicious pixels in a set of HMC images we shall compute lines of sight. The next step is the search for intersections of boresight lines with probable trajectories in the 3D space (we need a sequence of at least three images). To detect the non-moving particle (the more easy case) it is enough to find the intersection of at least three lines of sight at one place in space. For detection of moving particle one shall search for the intersection of at least three lines of sight with the line which crosses (with some precision) all of lines of sight that are under test (trajectory). To do this we have to enumerate all possible combinations of sets that consist of three lines of sight. When the line which could be particle trajectory is found it shall be checked by the tests: do moments of intersection form the correct time sequence? Can it originate from the comet nucleus? Does speed within the predicted bounds? Does speed vary along the trajectory? Those lines that passed all tests have high chances to be real particles trajectories, and the chances grow rapidly with detection of particle in every additional image in sequence. More detailed description of the steps of the algorithm is given below.

4.3.2. Selecting the suspicious pixels

It is not possible to distinguish between noise and possible particle image at HMC "flight" level images, because both processes (random noise and particles appearance) are random, so, they have the same statistics. We know that from the one hand, such images are very noisy (see an

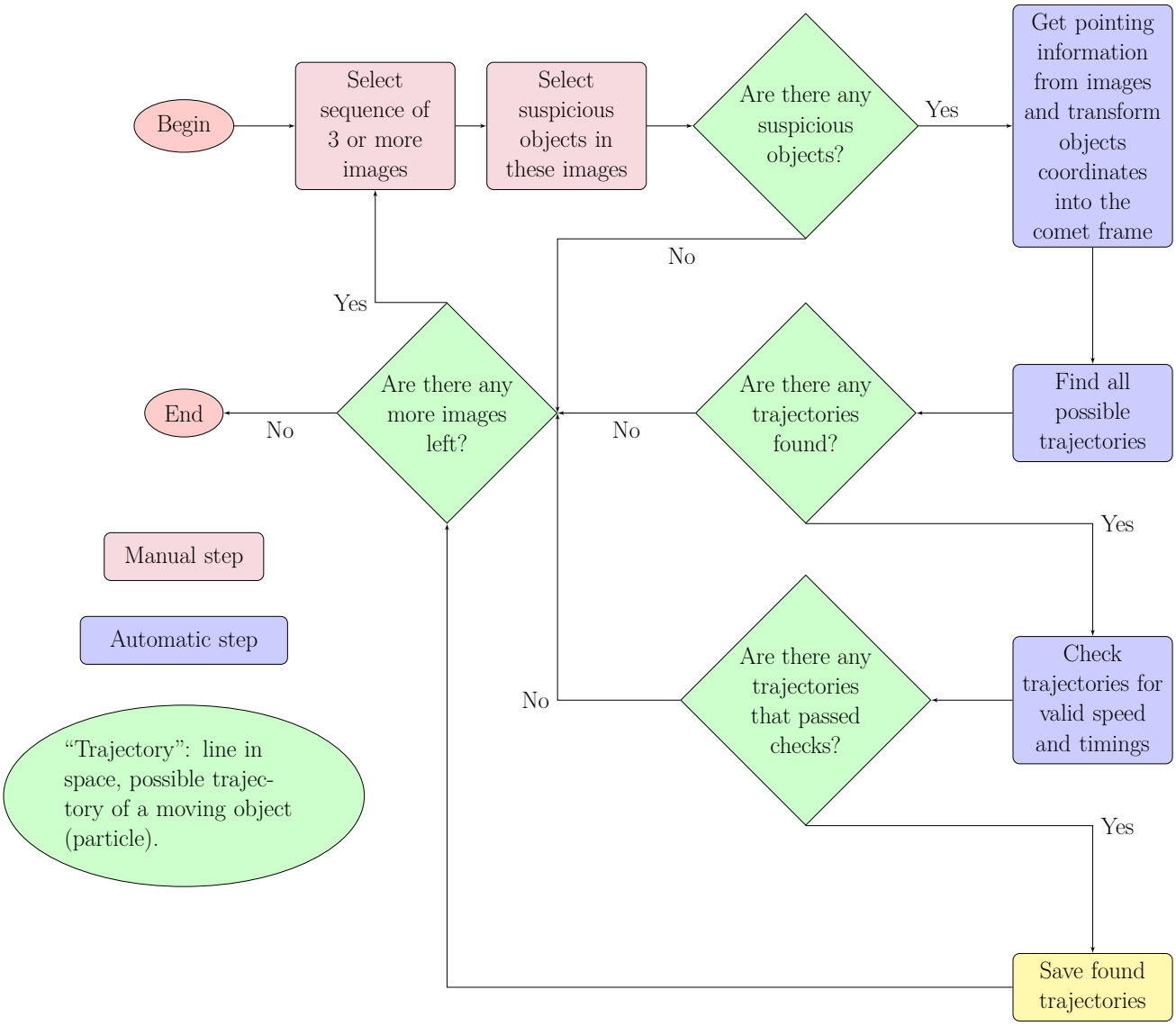

Figure 4.5.: General scheme of algorithm of particles detection. Parts of it are described in details below and at diagrams in figs. 4.17 and 4.18.

example in fig. A.1a), and it does not make sense to work with something which is probably not a particle image because we want to achieve the reasonable time performance. From the other hand, we do not want to miss any particle. A single HMC image contains many suspicious pixels (up to few hundreds depending on how strictly we select them). A sequence of 57 HMC images suitable for the particles search makes too many combinations for a brute-force algorithm. Such brute-force search is a very general problem-solving technique that consists of systematic enumerating all possible candidates for the solution and checking whether each candidate satisfies the problem's statement. To optimize the search we may decrease the number of suspicious pixels. For this we shall formulate the criteria what a suspicious pixel is. Since we do not expect that most part of the pixels is the particles images, and image of particle has to be not larger than one pixel, we may suppose that such event should be seen as pixel with brightness which differs from the brightness of neighbour pixels. Particle potentially may change its apparent albedo with time (*e.g.* because of rotation). Thus we may see the same particle as bright pixel on a dark background (the space) and then as dark pixel on a bright background (a jet). But such pixels for sure can increase the level of false positives. To exclude these pixels we may limit the minimal level of brightness, if we suppose that the situation when particle seen in one image as bright object, and in another as very dark, is quite unlikely. Changes of these two parameters lead to the determination of different number of suspicious pixels in image (see figs. 4.6 and 4.7). Figure 4.6 demonstrates image 3 469 which is shown as example of distribution of the suspicious pixels in accordance with using the different values of minimal brightness and minimal allowed deviations from the neighbour pixels (measured in standard deviations). It looks reasonable that in case of $B_{min} = 200\,\mathrm{DN}$ most of suspicious pixels are placed in the direction of the comet jets where particles are most probably expected. For example, analysis of Hartley-2 comet data revealed particles detected by searching for point sources with a peak amplitude greater than 5σ above the local background in images [17]. One can see from fig. 4.7 that for HMC data for $B_{min} = 150\,\mathrm{DN}$ and $200\,\mathrm{DN}$ for 4σ and 5σ, the numbers of suspicious pixels are close. Usage of the criterion $B_{min} = 150\,\mathrm{DN}$ and 4σ leads to the selection of about 50 suspicious pixels from a single image (fig. 4.7b) (out of 5476 pixels in an image with size 74×74 pixels), that is comparatively not too many, and those pixels are not distributed only in the jet areas (see as example distribution of pixels in image number 3 469 in fig. 4.6c). Distribution of brightness for the suspicious pixels selected in such way for our sequence is shown in fig. C.1.

To decrease influence of the background brightness variation within the image and from image to image we apply diagonal Laplace filter firstly. It is seen in fig. 4.8 that after Laplace filtration the peculiarities in the signal are more pronounced (compare fig. 4.8c and fig. 4.8d). After the filtering we selected the suspicious pixels in the images of the second derivative (fig. 4.8b) by a filter, similar to the median filter: if a given pixel differs from mean value in its given neighbourhood (rectangular region, so-called "window") for more than a given value (cutoff level is measured in standard deviations σ) the pixel is assumed to be suspicious. Figure 4.9 shows how the number of suspicious pixels depends on cut-off level and "windows" size. For all "window" sizes the results are quite similar, and amount of selected pixels predominantly depends from the cutoff level, while 3×3 pixels size seems to be too small, and also this size is close to the PSF (fig. 2.7). Applying the same procedure of the suspicious pixel selection to the calibrated data led to the results shown at fig. 4.10. If we compare the suspicious pixels coordinates for unprocessed and calibrated images, for data with cutoff level of 4σ and more, all pixels selected in calibrated images are present in the suspicious pixel list obtained from the unprocessed images almost always (except for a few pixels in several images in our data sequence).

For our purpose we selected cutoff level of 4σ and "window" size of 7×7 pixels as optimal, which leads to the selection of about 60 suspicious pixels from a single unprocessed image (see fig. 4.11 as example of pixels distribution).

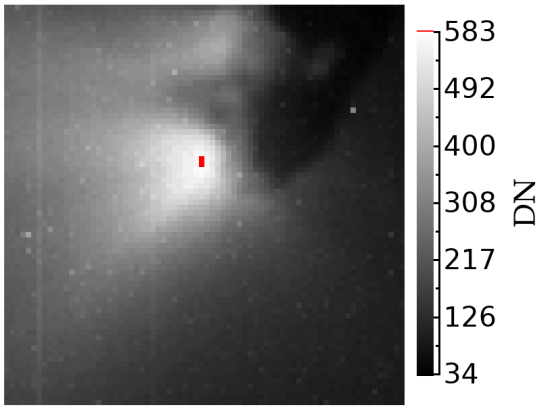

(a) Image 3469, grey palette.

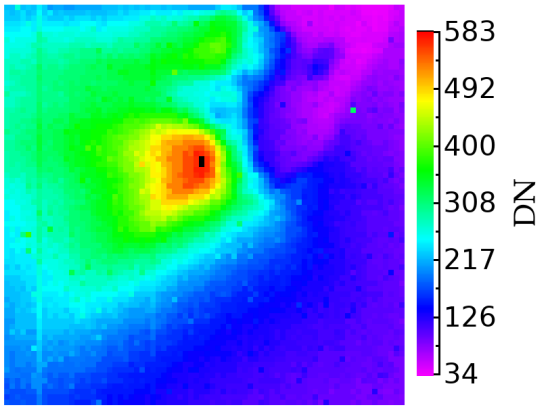

(b) Image 3469, colour palette.

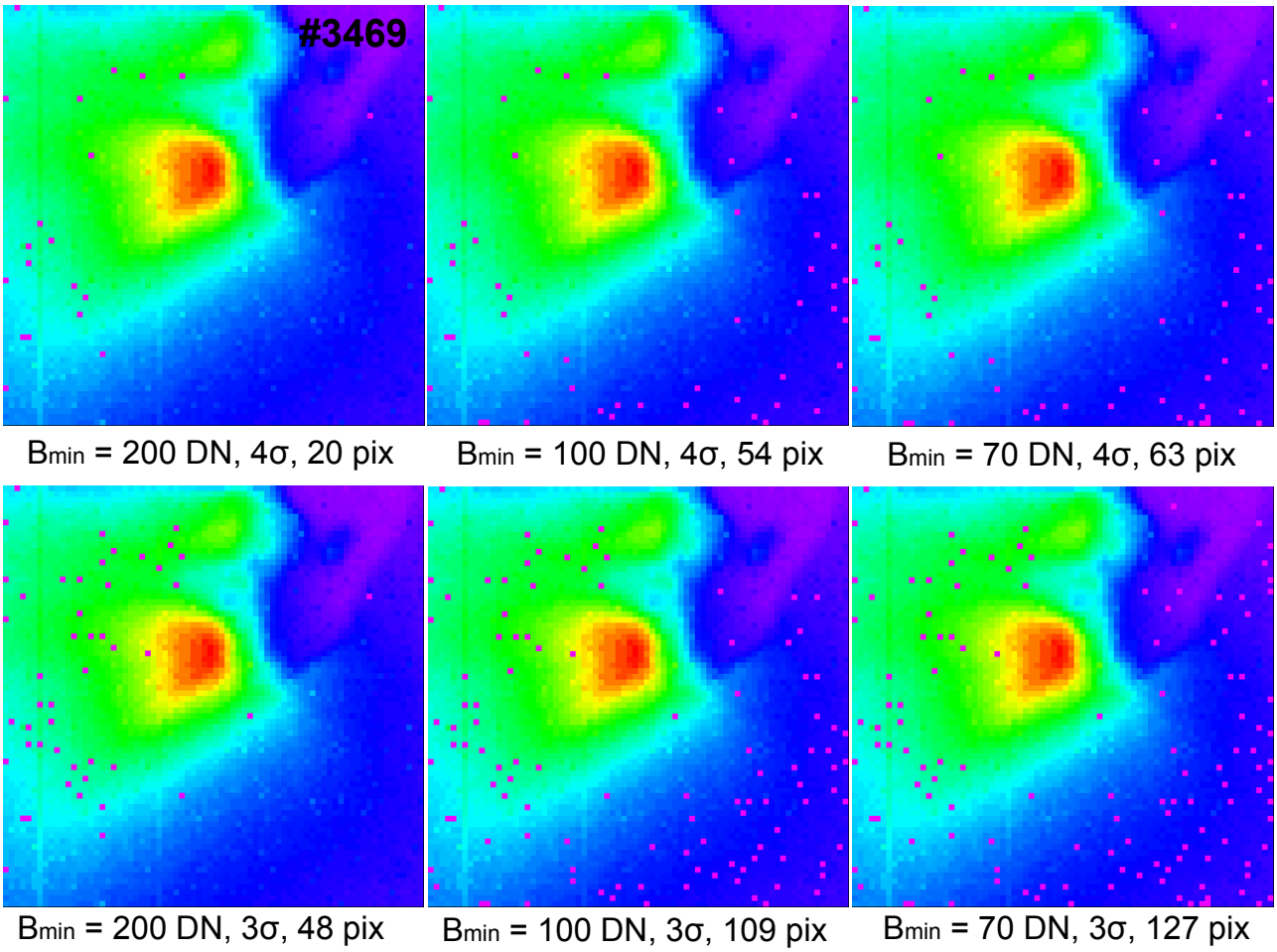

(c) Distribution of suspicious pixels for different configurations.

Figure 4.6.: Example of suspicious pixels distribution (magenta points in (c)) for image 3469. Image itself is shown in (a) and (b) in grey and colour palettes correspondingly. Red point in (a) and black in (b) indicates the position of the signal maximum in image.

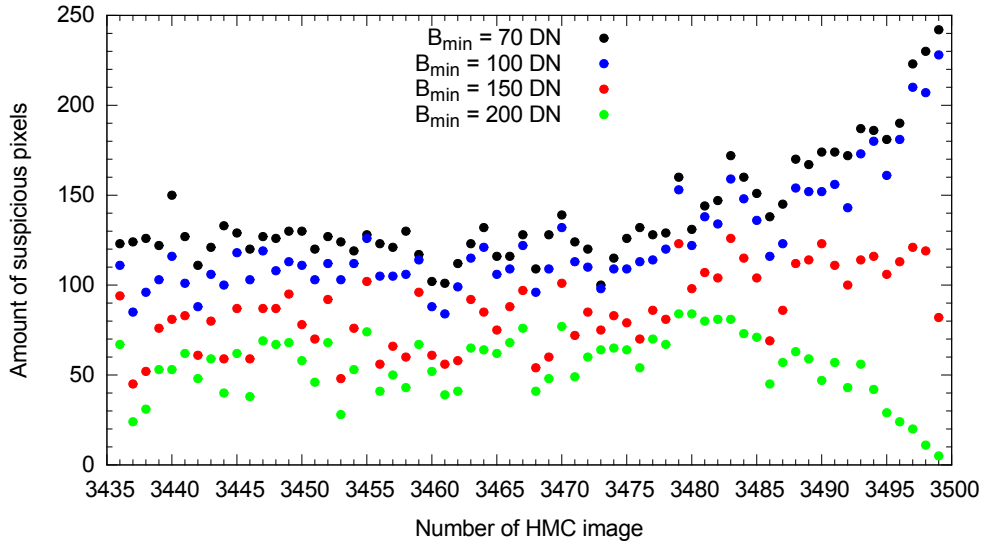

(a) 3σ.

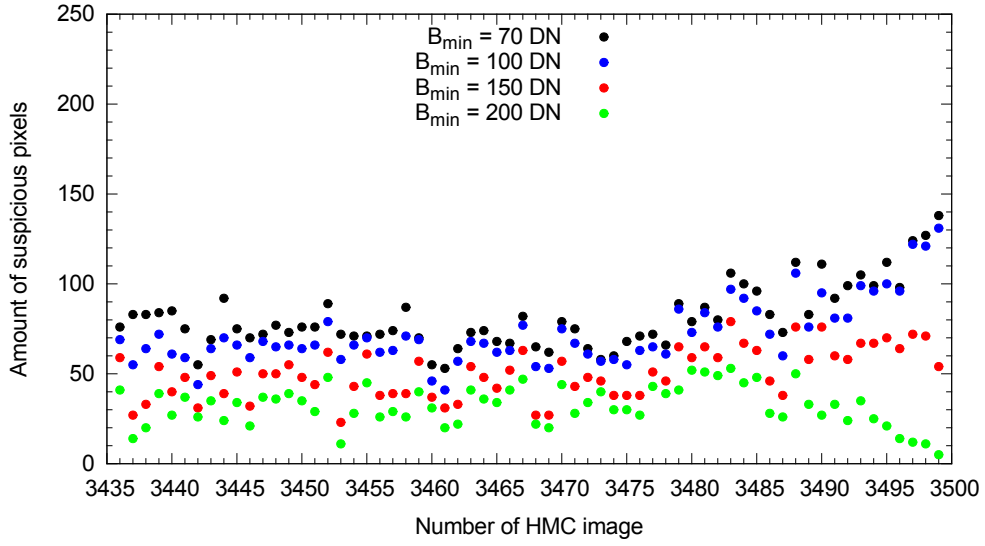

(b) 4σ.

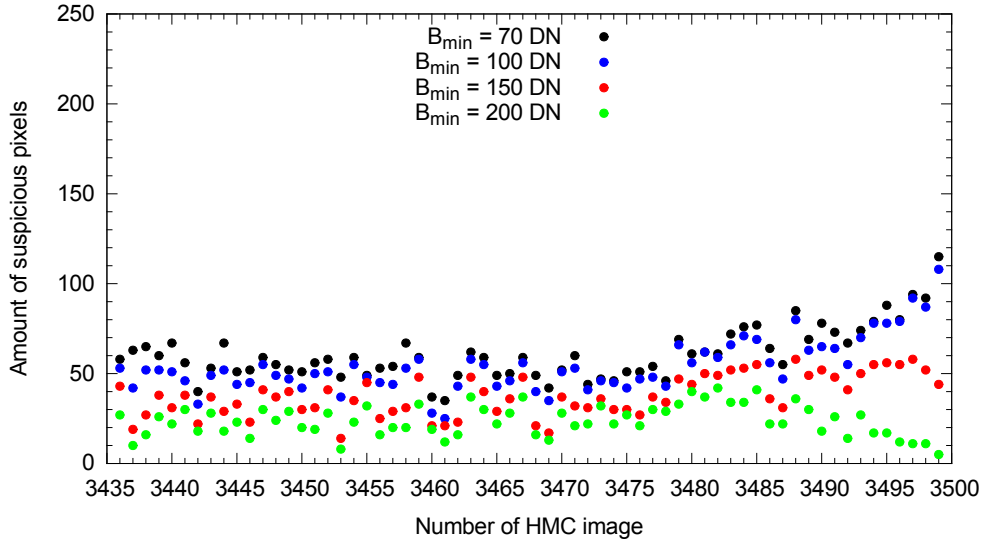

(c) 5σ.

Figure 4.7.: Amount of the selected suspicious pixels in accordance to the value limitation of minimal brightness B_{min}, and standard deviation σ. The windows size is 3×3 pixels.

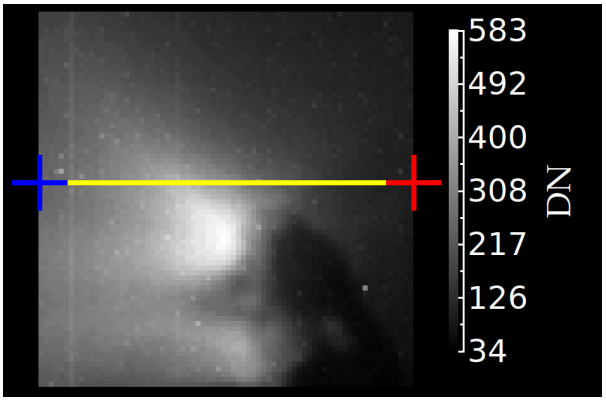

(a) Image 3469, slice.

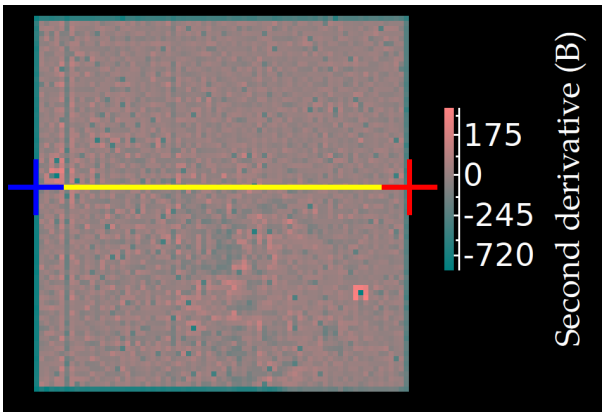

(b) Image 3469, Laplace filter, slice. Gamma = 4.

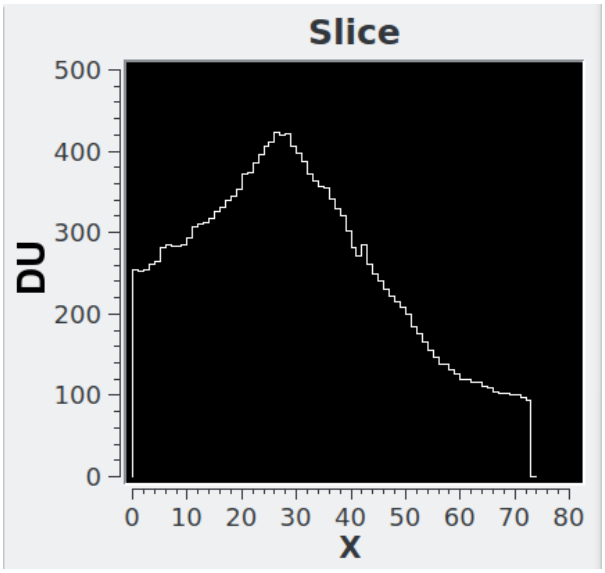

(c) Image 3469, slice profile.

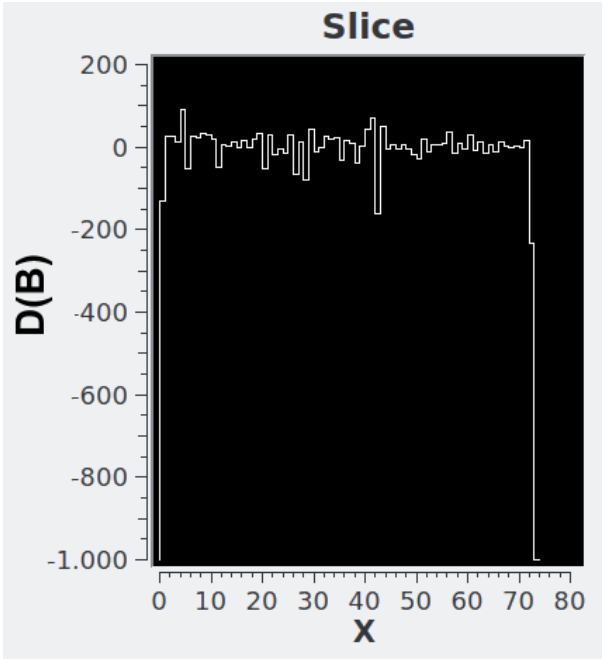

(d) Image 3469, Laplace filter, slice profile.

Figure 4.8.: Example of signal distribution along the line (marked by yellow colour) in raw image 3469 (a), and for the same place at this image after the Laplace filtering (b) with non-linear visualization (gamma 4). Corresponding profiles are shown in (c),(d).

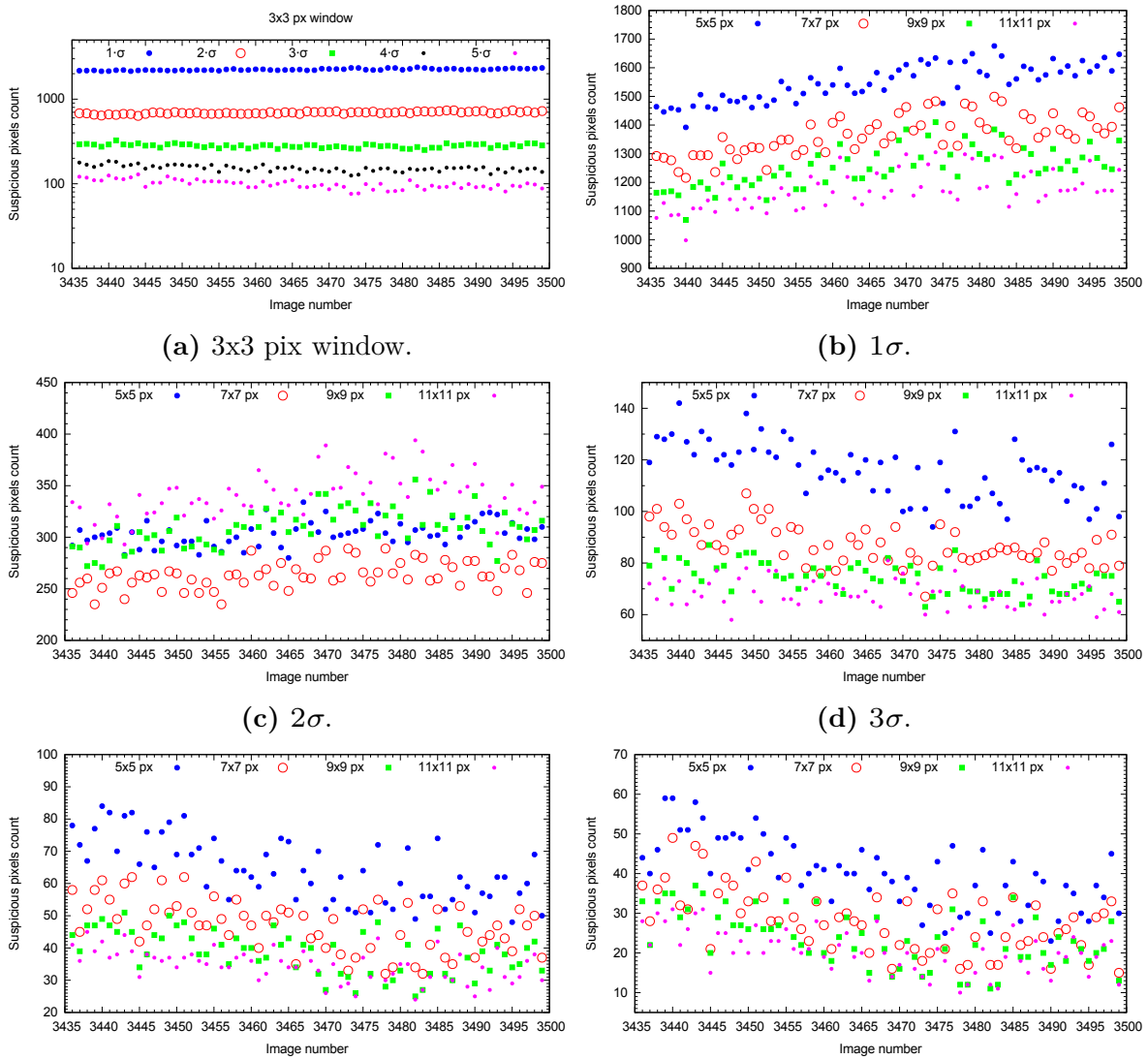

(a) 3x3 pix window.

(b) 1σ.

(c) 2σ.

(d) 3σ.

(e) 4σ.

(f) 5σ.

Figure 4.9.: Amount of the selected suspicious pixels for unprocessed (raw) images in accordance to the square "window" size (in pixels), and standard deviation σ. Case of the smallest "window" (a) is shown separately.

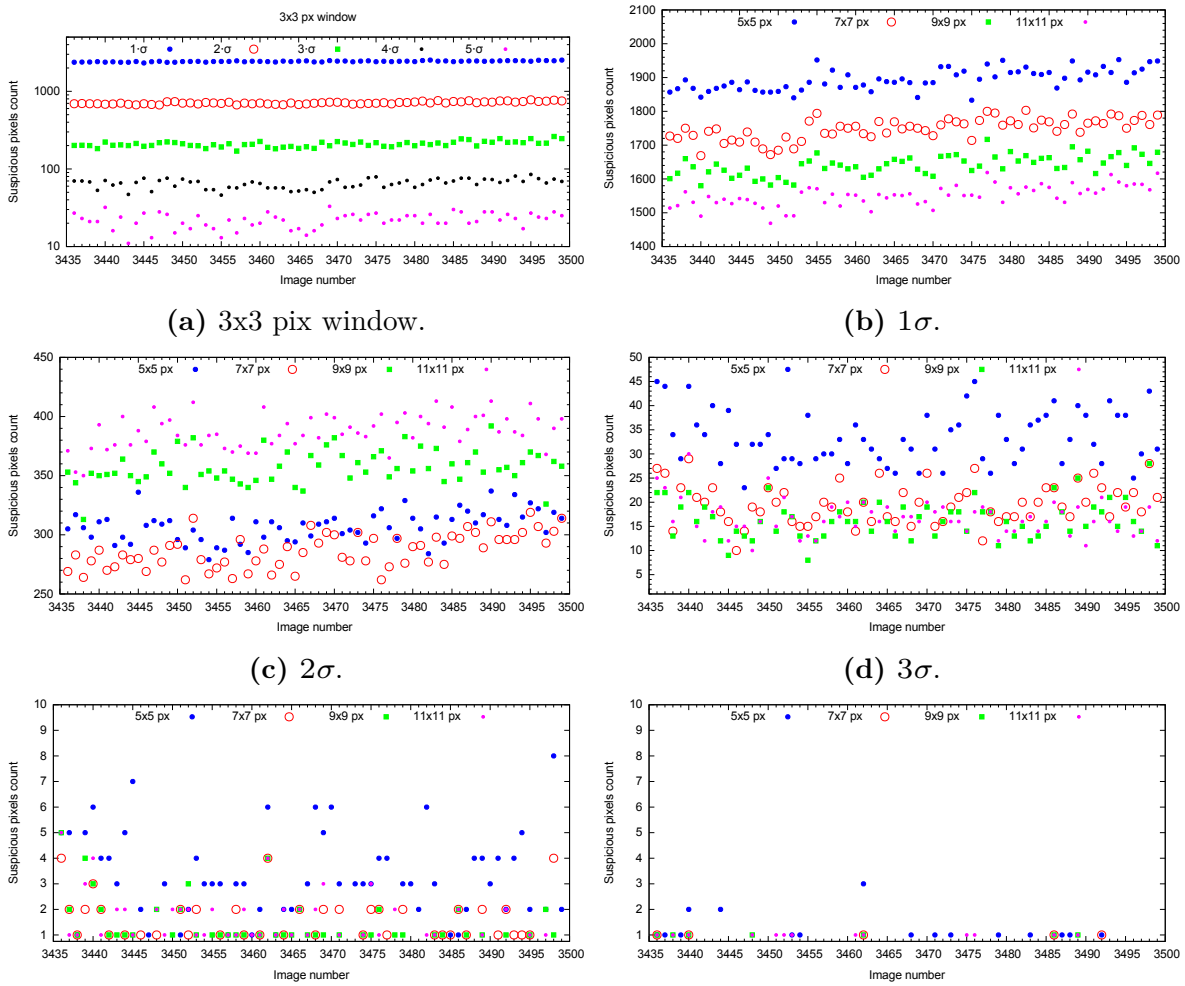

(a) 3x3 pix window.

(b) 1σ.

(c) 2σ.

(d) 3σ.

(e) 4σ.

(f) 5σ.

Figure 4.10.: Amount of the selected suspicious pixels for calibrated ("radio") images in accordance to the square "window" size (in pixels), and standard deviation σ. Case of the smallest "window" (a) is shown separately.

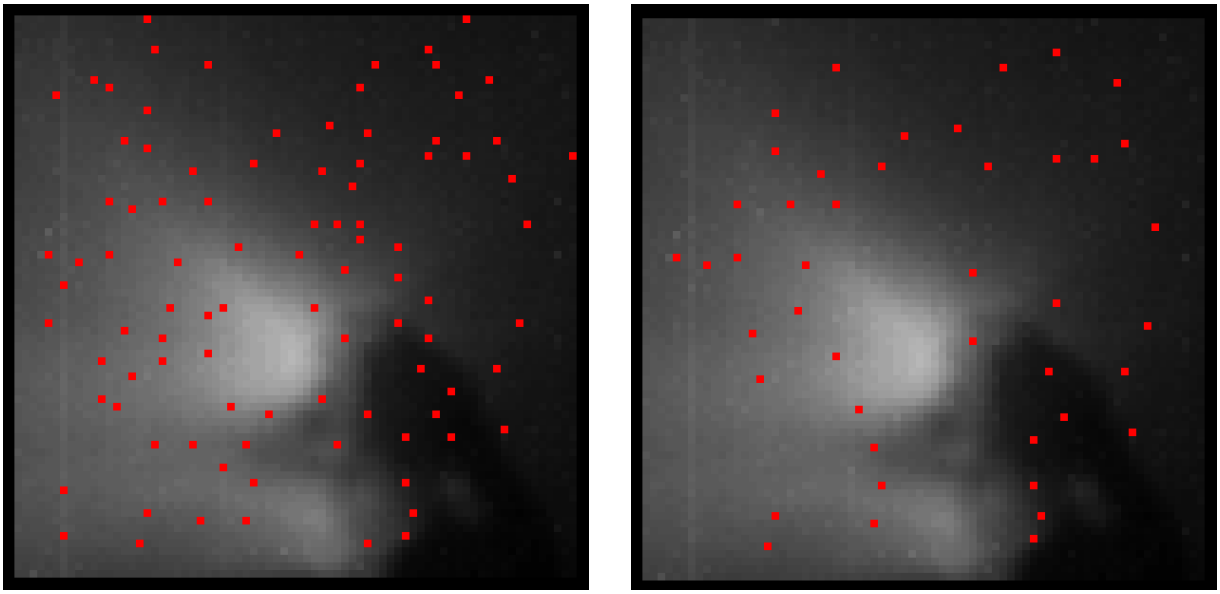

(a) Image 3469, 3σ. **(b)** Image 3469, 4σ.

Figure 4.11.: Distribution of the selected suspicious pixels for unprocessed image 3469 after consistent applying the Laplace and Median filters (7×7 pixel "window" and standard deviation 3σ (a) and 4σ (b)).

4.3.3. Restoring the lines of sight

Required for our purposes pointing information for the HMC was not released in a simple form like *e.g.* SPICE[4] that is used for other ESA's missions. There is only the SPK[5] file which provides Giotto spacecraft trajectory as well as ephemerides of Halley's comet and Earth for the duration of Giotto's closest approach to Halley [24]. So-called "geometrically corrected" images have been released in a specific coordinate system, and geometrical distortion was took into account [8]. But since we need to work with images obtained in the original geometry of camera ("flight" level), we have to restore pointing for every pixel by ourself.

To restore the line of sight one needs to know for the time of imaging the HMC camera location in space, in what direction it looked, how it was oriented, and how it was rotating during the exposure. We will not transform one image to the other in our sequence, but for the particles detection we need lines of sight for each suspicious pixel (in different images) to be in the same coordinate system. For that we utilise two directions for every HMC image: spacecraft-nucleus vector and spacecraft-Sun vector. Both are known in barycentric system with required precision, and thus for a particular pixel line of sight in the barycentric system can be computed.

Positions of the Sun and comet are known values (they are stored in metadata of HMC images), so we will use these two objects as reference ones. We may also assume that we know coordinates of some certain point on cometary image, which we can clearly identify in every image of our sequence, and than we can use this point as "base" point and calculate pointing for all other pixels of the image. Role of base points may play, *e.g.* the brightest point on comet, or a detail, which could be seen in comet images, so we need to determine which point is better to use as "base" point.

4.3.3.1. Determination of the base point in HMC image

One of the most important duties of the HMC on board was the tracking procedure. The HMC had to always centre the point of maximum brightness within the image frame. The camera had to be able to follow the comet's trajectory for any observing condition and without the prior knowledge of this condition. Onboard, all flyby parameters were continuously updated and the achieved accuracy enabled HMC to make good tracking prediction for the final encounter phase. A posterior analysis used all parameters at the same time and should thus have obtained a better accuracy. Tracking was based on the brightest bin (14×16 pixels) as reference which was found incessantly at the footpoint of the bright northern jet [25, 8]. If we suppose that the brightest point in the jet is the same region in all images, we can then measure it coordinates in the image coordinate system (see fig. 4.12).

We have determined the point of maximum brightness in every image (which is placed in the source region of one of the jets) and than measured manually the coordinates for the brightest point. Also we have measured in semi-automatic way the coordinates of the centres of three details on comet nuclei (marked by coloured circles and numbers in fig. 4.12a). Details 3 and 4 are not well resolved in the first images of our sequence (3 436 – 3 452), that is why it was hard to measure their coordinates. Also it was impossible to detect bright spot 2 (hill) for close images with numbers 3 481 – 3 484 and 3 488 – 3 493, because this part of the comet was not in the HMC field of view. Just to get a feeling what the details are, the changes of their brightness

[4]SPICE is an information system the purpose of which is to provide scientists the observation geometry needed to plan scientific observations and to analyse the data returned from those observations. SPICE is comprised of a suite of data files, often called kernels, and software — mostly subroutines. A customer incorporates a few of the subroutines into his/her own program that is built to read SPICE data and compute needed geometry parameters for whatever task is at hand. Examples of the geometry parameters typically computed are range or altitude, latitude and longitude, phase, incidence and emission angles, instrument pointing calculations, and reference frame and coordinate system conversions (see details in [22, 23])

[5]The SPK system is the component of SPICE concerned with ephemeris data

(in absolute units) are shown in fig. 4.12d. Some brightness' increase with oncoming to the comet (see fig. 4.12d), especially for B_{max} is expected because resolution is increased (see some additional information about the observations in figs. C.1 and C.3). Changes of resolution is clearly seen from the changes of the distances in images (in pixels) between curves in figs. 4.12b and 4.12c. Also it is clearly seen that these curves for different details are following each other pretty well (as well as the curve for B_{max}). This means that we can use any of these points as the base point. Since the B_{max} is present in all images we have used it as the reference point to determine the coordinates in space for all other pixels of each image.

4.3.3.2. The projection of the SC spin axis into the HMC image plane

The projection of the SC spin axis into the HMC image plane defines a point ZP (see fig. 4.13b) inside or outside of HMC images. This point is fixed with respect to the SC spin motion and the HMC images are rotated about ZP. To correct the geometrical distortion of HMC images it is required a good knowledge of ZP position [25]. Expected behaviour of ZP during HMC operation was:

- ZP lies near the HMC origin with ZP_z on line C (extension of the slit on detector C, see fig. C.2) in fig. 4.13b.
- ZP will change if the wobble changes.
- the SC's free precession makes ZP and the images move on a cone.
- mirror displacement will affect only the ZP_z component.
- HMC rotation will move ZP_y along line C into the Y_f direction (see fig. 4.13b).
- ZP_z has to be zero if the object crosses the line perpendicularly.

In MDM mode an independent method of calculation the ZP position was available, when the rotational fix point can be determined from the object position on two (or more) sensors at almost the same time and the internal HMC timing. Good alignment of the focal plane hardware was indicated [25]. It was found that although the initial wobble was compensated with the mirror, the rotational fix point is obviously displaced from line C (see fig. C.2). Findings reveal a linear dependence between ZP_z and ZP_y with a slope of 0.068°.

The acquisition of the comet was a difficult task because of hardware problems, and the achieved accuracy is limited [25]. The initial wobble was compensated completely in the Z-direction but in the Y-direction a rotational offset of 0.02° must be assumed. From the acquisition results and the flyby model, inertial coordinates could be determined for the SC attitude with high accuracy. Near closest approach rapid changes from image to image occur. In MDM the aspect angle (object positions) can be determined independently and with high accuracy. This reveals the flyby distance and the time of closest approach. The achieved accuracy allows to transfer the reference from the bright point on the northern tip to the geometrical centre of the nucleus. Nutation and dust impacts turned out as error terms in the tracking performance.

For practical reasons the projection of the spin axis into the HMC FOV ZP needed to be known for every image, and it was stored in the catalogue in [25]. Figures 4.13c and 4.13d demonstrate projection of the spin-vector into the image plane for the set of images that is used in our work.

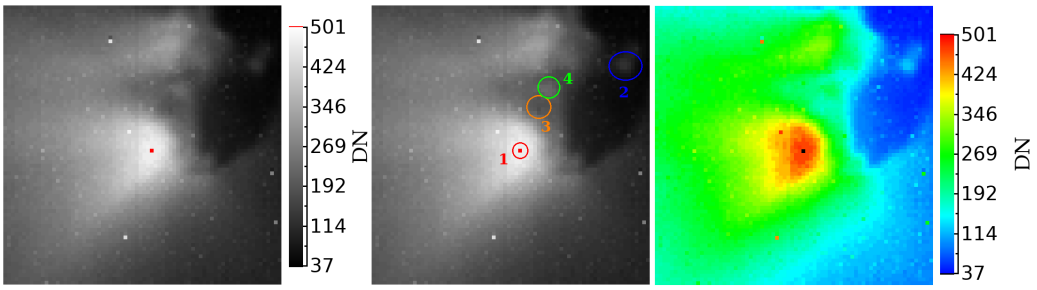

(a) Scheme with marked regions for image 3477.

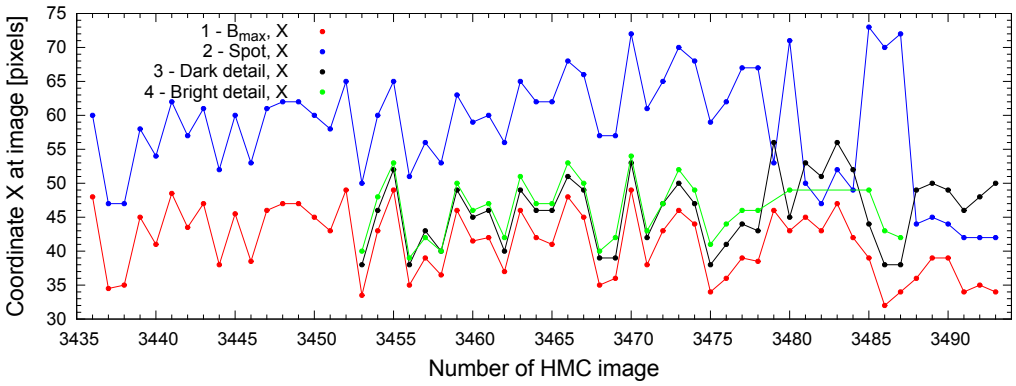

(b) X coordinate.

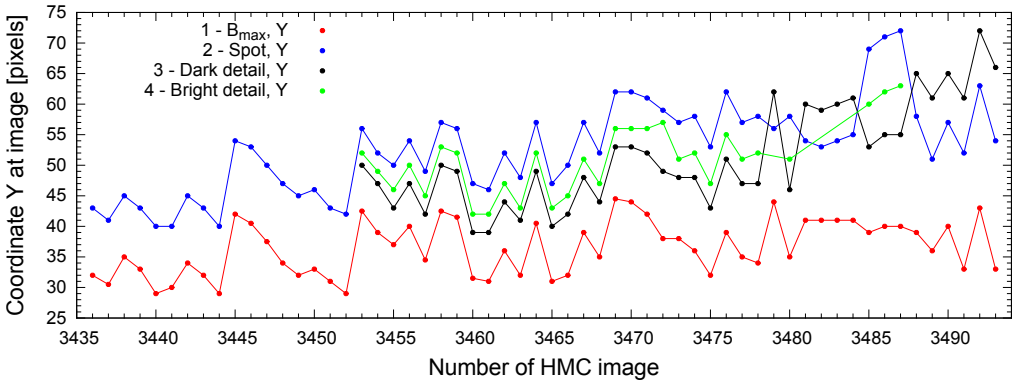

(c) Y coordinate.

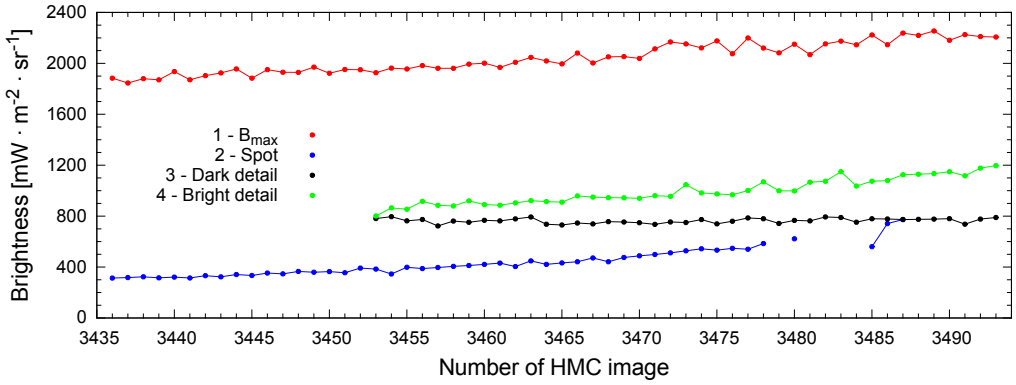

(d) Brightness of details.

Figure 4.12.: (b), (c): coordinates of comet details in image plane. Their locations at comet are marked by coloured circles in (a): 1 (red) is the maximum of brightness (B_{max}) in image which is placed in the source region of one of the jets. Position of the B_{max} is shown by red (in grey palette image) and black (in colour palette image) points correspondingly; 2 (blue) is the mountain; 3 (orange) is the dark and 4 (green) is the bright parts of the detail in comet. Brightness of details' centres is present in (d).

4.3.3.3. Geometric correction of HMC images

The imaging technique adopted by the HMC team was a line scan mode. The portion of the sky swept by the exposed lines during image taking was a section of an annulus resulting in over-sampling at the end of the exposed lines nearest the SC spin axis and under-sampling at the other end [8]. The published images have been corrected for the geometrical distortion introduced by "squashing" the section of an annulus into rectangular array [8]. The effect of the geometric rectification procedure is seen *e.g.* in comparison of the pairs of images from "flight" and "geo" levels: if compare fig. A.1a vs. fig. A.1c, and fig. A.1d vs. fig. A.1f. Since we work with "flight" level of data we need to take into account the changes of the field of view for different pixels when we restore the lines of sight.

Precise boresight vectors are crucial part of the particle detection, because only space coherence differs the images of a particle from a noise. Geometry of the raw HMC images is quite complicated, its determination required significant efforts from the HMC team and in the given work quite similar one needs to be done. "Rectification" of the HMC images can serve as a good test for the developed software. Match between the images created by the HMC team and rectified by us would indicate correct determination of the images geometry, that is a function of time, camera aspect angle, TDI, and sensor. The match for the whole HMC images sequence would indicate that these parameters are handled correctly. To test this part of our algorithm we compared the geometrically corrected HMC image with the images in the catalogue ("geo" level) from the ESA & NASA web archives.

The correction is done using an algorithm similar to the one described in [26] (for details see also [27]). It closely resembles algorithms used in cartography ("cartographic tangent cone" method). To do this we need to know the position of the SC spin axis (see fig. 4.13) and the TDI time (from image metadata). The axis of a cone is defined to coincide with the extension of the SC spin axis. The opening angle is defined such that the sides of the cone touch the celestial globe at a co-latitude defined by the angle between the line of sight (for the centre of line C at given time) and the SC spin axis. The image (on the celestial globe) is then mapped onto the cone which is subsequently "unrolled" to form a plane, finally giving the corrected image. An original pixel address can, therefore, be mapped onto the image plane. The resulting output address is not integer and hence bi-linear interpolation was performed.

The rectified images for working data set were obtained and compared with geometrically corrected by the HMC team ones. To estimate more precisely do the calculated images and "geo" images are congruent, we have measured the coordinates of four points (details, see fig. 4.14) at rectified comet image, and got all possible triangles for which we calculated the lengths of the sides, and then compared them with the same triangles measured in "geo" images. It was found that with uncertainty about 1 pixel they are equal (precision of measuring the coordinates is certainly not less than 0.5 px for each measurement). In the other words, with accuracy of measuring the points coordinates for forming triangles (about 0.5 px for one point) which were used for measuring the distances, images are congruent.

It was found that it is practically impossible to estimate the rotation angle accurately. For measuring it we calculated for what angle the large triangle side (with length 20 – 30 px) declines from the horizontal axis of image and then compare the result with the same measurement at "geo" images. Even one pixel difference in length (comes from the coordinates' measurement) leads to the appearance of difference in desired angle. Our base is 20 – 30 px wide, and the positional error is 1 pixel, with precision of 0.5 px one needs base of at least 55 – 60 px to detect rotation angle of 1°. Thus, precision of the rotation angle determination is 0.03 – 0.05 rad, *i.e.* 2 – 3°. This means that accuracy of measuring method is not enough for estimate such small changes. However, after using blink-comparator it is possible to state that images can be aligned by shifts and the difference between them then can be attributed to the fact that "geo" ones are processed by filters and look smooth while calculated by us ones are not.

Concluding, the performed test showed that coordinate transformation of the conic scan into the rectified system is correct: calculated images are congruent to the known images.

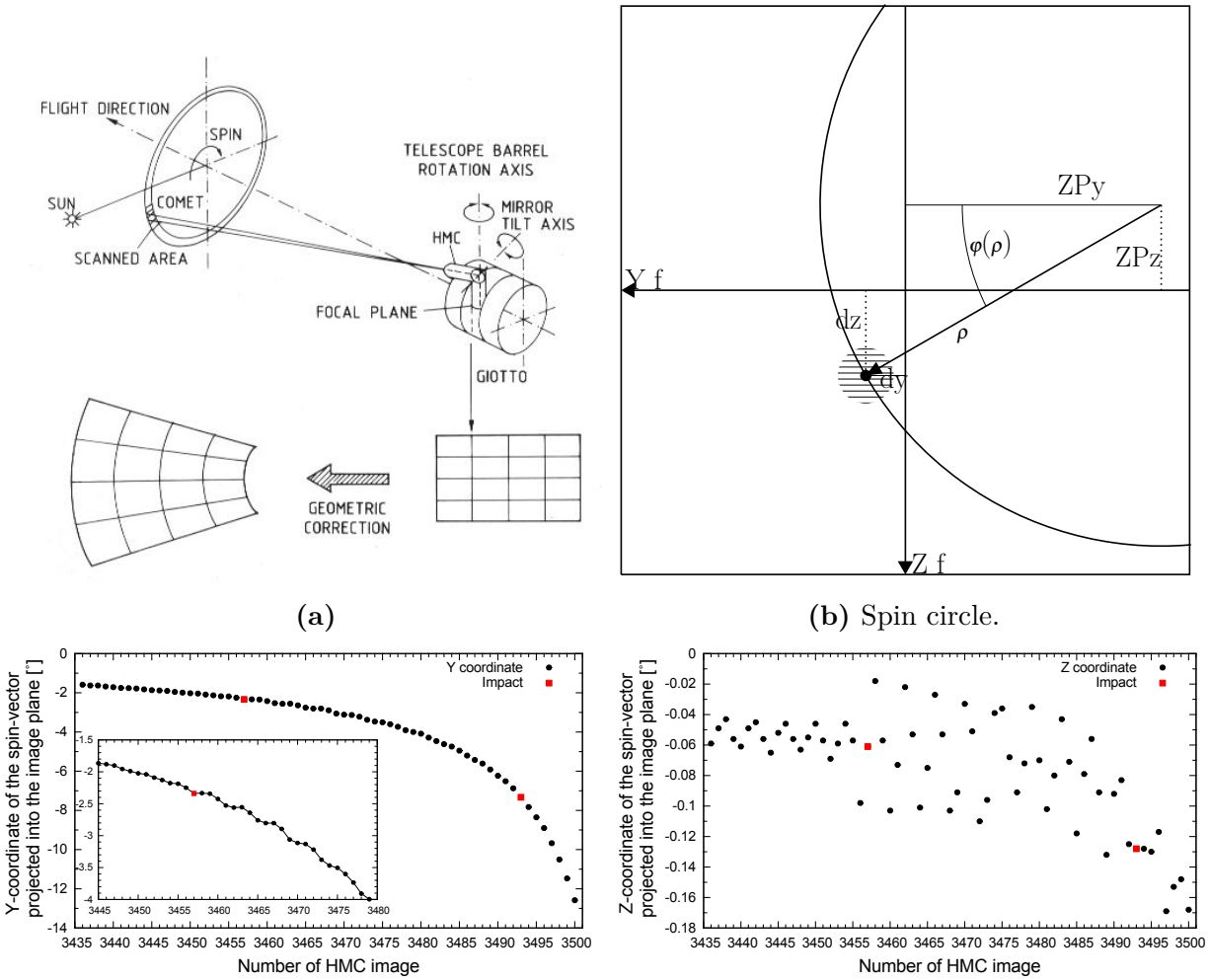

(a)

(b) Spin circle.

(c) Y coordinate.

(d) Z coordinate.

Figure 4.13.: (a): the principle of HMC operation (image from [8]). Top: HMC could rotate to view objects away from the SC spin axis while the mirror tilt mechanism increased the speed of the object motion across the slit for observations close to the spin axis. Bottom: a segment of an annulus is stores in the rectangular CCD. Its true geometry has to be reconstructed by a mathematical transformation (geometric correction). (b): spin circle of an object in the HMC focal plane coordinate system; object position as defined by the aspect angle ρ and its phase φ_p together with the point ZP miss the origin by dy and dz (image from [25]). (c),(d): X and Y coordinates of the spin-vector projected into the image plane (data from catalogue in [25] was used to build these images). Time of impacts of SC with particles is marked by red squares.

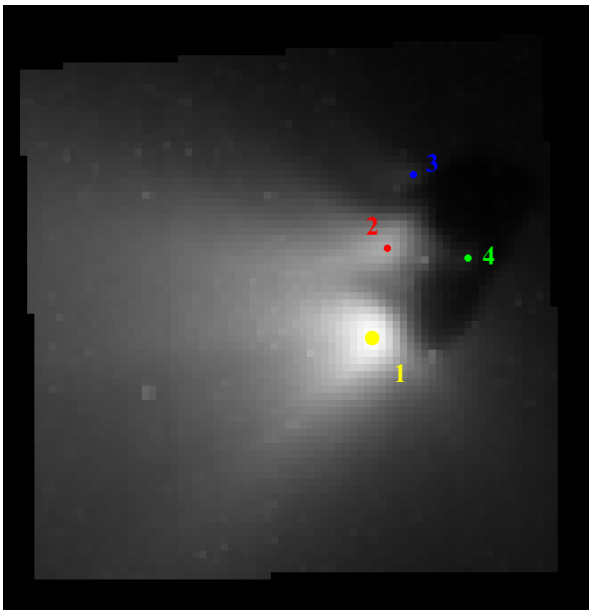

Figure 4.14.: Position of points used for studying the congruence of calculated images (geometrically corrected) and images obtained by HMC team.

4.3.4. Coordinate systems and transforms

The particles which might exist near the comet nucleus would have been detected by the HMC as contrast pixels on the dark or bright background. The only difference between these particles and random noise is space coherence of the formers. This means that images of the particles have to bear this information and thus be placed in images systematically but not randomly as noise pixels are. We assume that after the ejection from the nucleus a particle does not interact with the comet. As such a particle continues to move along a straig line in a frame connected to the comet (*system H*). Thus we have to detect objects which, in the frame connected to the comet, move along straight lines and these straight lines intersect in the vicinity of the nucleus. The particle has to move in the direction from comet. In special case their velocities might be so small that they will be seen by HMC as non-moving objects.

Since the problem is formulated in the simplest possible way in a frame connected to the comet and this frame can be considered as inertial on a scale of the HMC experiment, the solution will be formulated in it.

We select the suspicious pixels (see section 4.3.2), then compute their lines of sight and transform them into the comet reference frame. If a set of these lines from different images intersects in a given vicinity of a certain point or these lines are displaced from a certain particle trajectory for not more than a given angular distance we assume that a particle is detected.

Known facts about the camera and observation process which are related to our task

- Spacecraft (SC) is spin rotated.
- The imaging technique adopted by the HMC team was a line scan mode (by rotation of the SC).
- Camera orientation with respect to the spin axis (SA) is changed from image to image because the camera was tracking the comet.
- Most of the fly-by geometry parameters were obtained in real time with reasonable accuracy since they were a part of the HMC onboard tracking data or could be accessed by straightforward calculations.

- Several dust impacts perturbed the SC attitude that caused random changes of the SA position from image to image. *Y*- and *Z*-coordinates of the spin-vector projected into the image plane were calculated and stored for every image after the mission (ZPY and ZPZ) [25].

4.3.4.1. Description of the coordinate systems

To compute the lines of sight in *system H* we have to establish a transition from the image pixel coordinates (*system I*) into the *system H*. To do this one has to know position and orientation of the camera with respect to the *system H*. Cartesian barycentric coordinates of the comet Halley and Giotto are known for the time of HMC experiment. Since the particle trajectories are randomly oriented straight lines (not necessary originated from the centre of the comet) let us define the *frame H* as a Cartesian barycentric system shifted to the cometary position. All boresight vectors have to be transformed into the same coordinate frame. Since we are looking for trajectories which are straight lines, and lines of sight are straight lines, it is natural to solve this problem in a coordinate system where these straight lines are defined in the simplest form. Obviously, such system is Cartesian one and centred at the comet nucleus since trajectories are expected to begin near the nucleus too. The task then is to find the line of sight for a given pixel in a given image in this coordinate system, which is common for all images. Such coordinate *system H* may be established via barycentric coordinates of the Sun, Halley comet and GIOTTO and information from HMC headers (Sun azimuth and elevation). To connect HMC images with this system we use the brightest pixel on cometary surface (the activity region on the northern subsolar limb, see section 4.3.3.1), defined at every image with accuracy 0.5 px, and assume that its line of sight is the vector connecting GIOTTO and the Halley comet, as a reference direction, and Sun azimuth as second reference for fixing rotation of the system around the reference direction.

Cone Geometry of HMC images is not simple, because images were taken from the spinning SC. The imaging technique adopted by the HMC team was a line scan mode. The portion of the sky swept by the exposed lines during image taking was a section of an annulus resulting in over-sampling at the end of the exposed lines nearest the SC spin axis and under-sampling at the other end [8]. The published at web images have been corrected for the geometrical distortion introduced by "squashing" the section of an annulus into rectangular array [8]. Since we work with "flight" data level (raw image with processed header which contains the information about the given image) we need to take into account the changes of the field of view for different pixels when we restore the lines of sight. We need to know in what direction camera looked, how it was oriented for every image, and where was the SC relative to the comet. In few words, we have to be able to go successively from image coordinates to the coordinates on cone, then to the coordinates on sphere which touched the cone, and then to the directions in space (Cartesian system related to the comet).

The line of sight computations are implemented using the following co-ordinate systems:

System I is image co-ordinate system with the co-ordinate origin in the bottom left corner. X co-ordinate increases to the right, Y to the top at unprocessed image.

System S is spherical co-ordinate system with polar axis of unity sphere aligned to the spacecraft spin axis and the origin at the camera position. For negative values of the ZPY parameter (which is typical and true for all MDM images) longitude of the centre of the image is 180°. Thus, in a typical MDM image in System S latitude increases from left to right, and longitude increases from top to bottom.

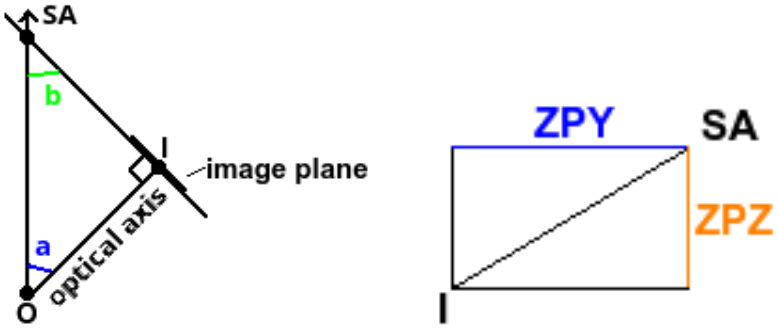

(a) Cone scheme.

(b) Spin axis real position at image plane defined by ZPZ and ZPY.

Figure 4.15.: Definition of the cone.

System B is Cartesian barycentric co-ordinate system.

System H is the same as System B, but co-ordinate origin is moved to the comet nucleus. Thus the system moves with respect to the Solar system barycentre.

4.3.4.2. Transitions between co-ordinate systems

System I → System S Co-ordinate origin in a HMC image is in the bottom left corner.

Firstly, we have to restore the geometry of flight images. As it was told above, image is the part of the surface of cone. For every pixel we have to obtain its place at the cone surface. For transition from the pixel in image to the line of sight in space we need to solve the following tasks:

1. Define the cone: value of the cone angle is defined by the SA and the camera optical axis (the prolonged straight line at image plane intersects at some point (cone apex) with the SA, and thus formed the cone). Optical axis is perpendicular to the cone surface, thus the angle between the SA and optical axis defines the cone. $I - SA$ at fig. 4.15b is the same as angle a at fig. 4.15a, and is defined by cosine theorem (spherical geometry): $\cos^{-1}(\cos(ZPZ) \cdot \cos(ZPY))$. Thus cone open angle $b = 180° - 90° - a = 90° - a$ (see fig. 4.15a).

2. Calculate the position of image frame at the cone surface: coordinate system is defined by the distance from the vertex to the given point and azimuth.

3. Find the orientation of the cone in inertial space, which is given by orientation of rotation axis (in our case this is SA), and its rotation position is defined by some known rotation (azimuth).

4. Due to the geometry of our task it is easy to expect appearance of the spherical coordinates with polar axis coinciding with the SA. So the cone touchs the unity sphere which is located inside of it.

We assume that the unity sphere touches the cone at latitude $\theta = \pi/2 - \cos^{-1}(\cos(ZPZ) \cdot \cos(ZPY))$. Thus the centre of the detector "C" has latitude of θ on the celestial sphere, where the spacecraft spin axis is its polar axis. We assume its longitude to be π if ZPY is negative and 0 in the opposite case (see fig. 4.16).

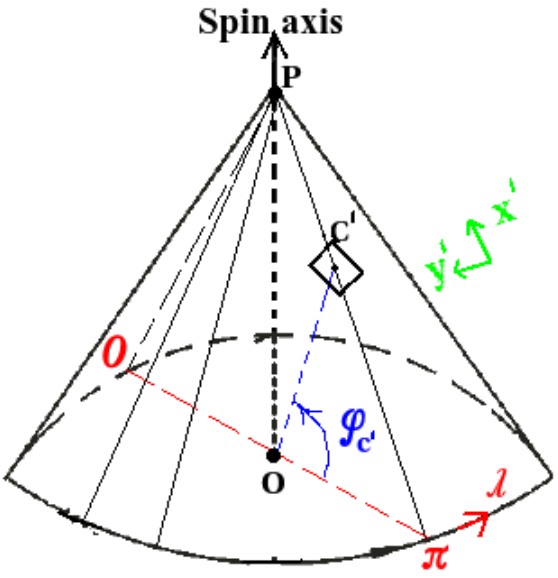

(a) Image location at cone surface and coordinate system.

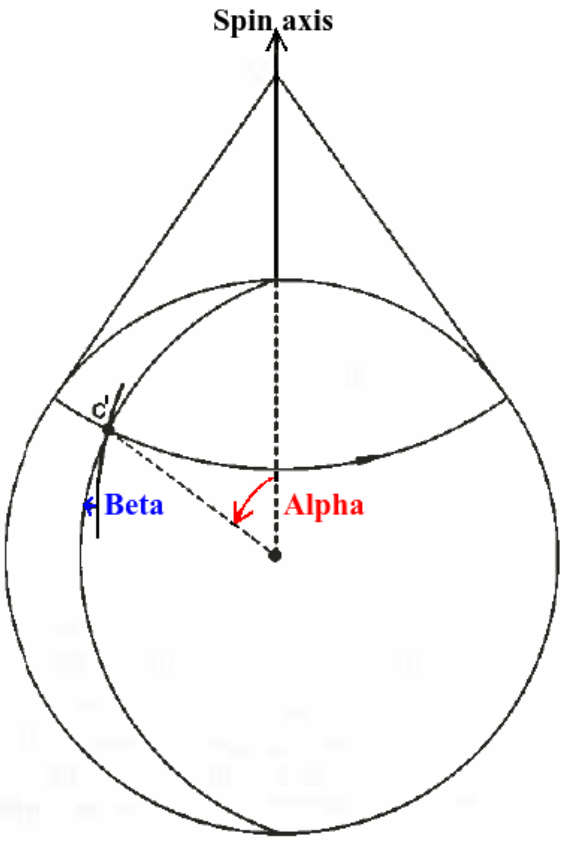

(b) Tangent cone.

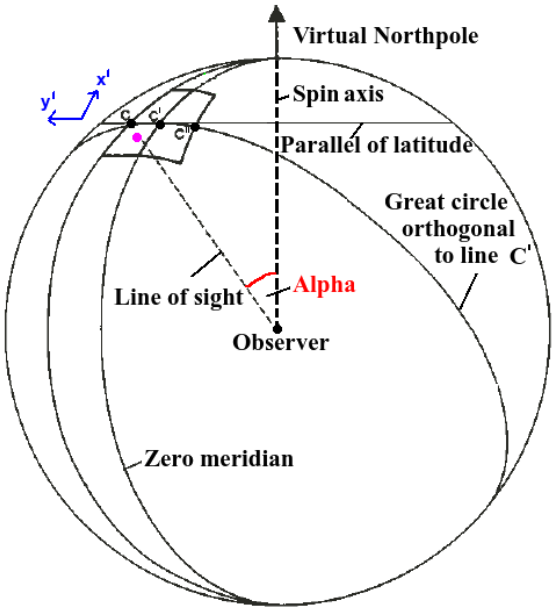

(c) Celestial sphere, *system S*.

Figure 4.16.: Tangent cone through the centre pixel of line C (b). Stripe scanned by CCD line C on the celestial sphere during one TDI interval (c).

At initialisation step we compute coordinates of the central pixel on the virtual cone surface tangential to unity sphere:

$$\begin{cases} r_0 = \cot(\theta) \\ \lambda_0 = \begin{cases} 0, ZPY \geq 0 \\ \pi, ZPY < 0 \end{cases} \end{cases}.$$

Here r is distance from the cone vertex, and λ is longitude (zero in subscript means the central point).

After the initialisation we proceed as follows:

1. Move co-ordinate origin to the centre of the image (transition matrix T_C), and get new coordinates (X_0, Y_0).

2. Rotate co-ordinate system around co-ordinate origin by angle $\beta = \tan^{-1}(ZPZ/ZPY)$ (rotation matrix R_β). After that the spin axis projection is located on the X' axis ($ZPZ = 0$) (the new system is named (X', Y')).

3. Scale the image multiplying by pixel TDI field of view s:

$$\begin{cases} s_x = 22.4\,\text{rad} \\ s_y = 2\pi \cdot TDI/\text{spin period} \end{cases}$$

4. Add (r_0, λ_0) to the coordinates and let's name the obtained co-ordinates (χ, υ). Under this definition $\chi = r - r_0$.

Now we apply formulae of the conic projection (chapter D) to get latitude φ and longitude λ on the sphere:

$$\begin{cases} \varphi = \theta - \tan^{-1}(\chi - \cot(\theta)) \\ \lambda = \upsilon + \lambda_0 \end{cases}$$

System $S \rightarrow$ System B We have three known object positions: the Sun, Giotto SC and Halley comet nucleus. Consider vectors Giotto-Sun $G\vec{S}^S$ and Giotto-Haley $G\vec{H}^S$ in the system S and the same vectors $G\vec{S}^B$ and $G\vec{H}^B$ in the barycentric system B. $G\vec{S}^S$ is defined by the azimuth and elevation pair, $G\vec{H}^S$ is defined by the line of sight of the brightest pixel of the comet image. $G\vec{H}^B$ and $G\vec{S}^B$ are determined from barycentric coordinates of the objects.

We determine two rotations: firstly to align $G\vec{H}^S$ with $G\vec{H}^B$, and then the second rotation around $G\vec{H}^B$ to align $G\vec{S}^S$ with $G\vec{S}^B$ by azimuth, counted in a plane, perpendicular to $G\vec{H}^B$.

First rotation: angle α_1 between $G\vec{H}^B$ and $G\vec{H}^S$ is equal to

$$\alpha_1 = \cos^{-1}\left(\frac{G\vec{H}^B \cdot G\vec{H}^S}{|G\vec{H}^S||G\vec{H}^B|}\right)$$

Rotation around axis $\vec{r_1} = G\vec{H}^S \times G\vec{H}^B$ (vector product) by angle α_1 aligns $G\vec{H}^S$ with $G\vec{H}^B$: $G\vec{H}_1^S = M_1 \times G\vec{H}^S$, where M_1 is the corresponding rotation matrix.

After that we project vectors $G\vec{S}^B$ and rotated $G\vec{S}_1^S = M_1 \times G\vec{S}^S$ onto the plane, perpendicular to the $G\vec{H}^B$ obtaining $G\vec{S}_{proj}^B$ and $G\vec{S}_{1proj}^S$. Angle between them

$$\alpha_2 = \cos^{-1}\left(\frac{G\vec{S}_{proj}^B \cdot G\vec{S}_{1proj}^S}{|G\vec{S}_{1proj}^S||G\vec{S}_{proj}^B|}\right)$$

The next rotation around $G\vec{H}^B$ by angle α_2 (determined via matrix M_2) aligns azimuth of the Sun in both systems.

Now we can apply rotation 1 and 2 to any point in system S and transform it into system B:

$$\vec{w}^B = M_2 \times (M_1 \times \vec{w}^S)$$

System $B \rightarrow$ System H Transition from system B to H requires co-ordinate shift, determined by relative positions of the comet and Giotto. No rotation is required. At this system lines of sight for any pixel is defined by two vectors:

1. Vector of direction from Giotto SC to comet for suspicious pixel (was defined at previous steps).
2. Point from which this vector originates (coordinates of Giotto SC).

If a set of these lines from different images intersects in a given vicinity of a certain point or these lines are displaced from a certain particle trajectory for not more than a given angular distance (and if conditions of realistic case are executed) we assume that a particle is detected.

4.3.5. Searching the particles

The set of suspicious pixels might produce many combinations that have to be analysed (with most part of it to be rejected). From the other hand, we do not want to miss any possible particle. While a brute-force search is simple to implement, and it will always find a solution if it exists, its cost is proportional to the number of candidate solutions — which in many practical problems tends to grow very quickly as the size of the problem increases [6]. We shall optimize the algorithm to decrease the time needed for finding the all possible particles. The main aim is to reject combinations of lines of sight that failed tests as soon as possible. To do this effectively we will use the following knowledge about particles that we have *a priori*:

1. For a given particle and HMC image not more than one pixel can be occupied by a particle.
2. Particle trajectory shall start in the given neighbourhood of the nucleus.
3. Particle speed shall be constant along trajectory.
4. Particle trajectory shall cross lines of sight in order, defined by imaging times (from past to future).

We can additionally assume that particle has to be visible in all images where it was imaged (*i.e.* it does not decrease brightness too much), which can significantly simplify enumeration of possible combinations.

Having lists of pixels' lines of sight for each image we can start actual search for a possible particle trajectories (hereafter we define non-moving particle as a special case of a moving particle), please see algorithm schemes in figs. 4.17 and 4.18:

1. Sort the list of images by time.

[6] Brute-force search is typically used when the problem size is limited, or when there are problem-specific heuristics that can be used to reduce the set of candidate solutions to a manageable size. This method is also used when the simplicity of implementation is more important than speed. This is the case, for example, in critical applications where any errors in the algorithm would have very serious consequences; or when using a computer to prove a mathematical theorem. Brute-force search is also useful as a baseline method when benchmarking other algorithms or metaheuristics. Indeed, brute-force search can be viewed as the simplest metaheuristic.

2. Extract all possible image "triads". "Triad" is a set of three lines of sight from three different images in a correct time sequence.

3. For each "triad" test for particle trajectories. If there are any, save this triad to the list of triads with trajectories.

4. For each "triad" with trajectories try to add a fourth image and test found trajectories with the fourth image.

5. Each trajectory that we are unable to extend is saved to the final list.

6. To each extended trajectory try to add next image until image sequence is exhausted.

Finding possible trajectories in images is different for initial triads and for extending: for the first three images we use all possible combinations of lines of sight from different images, but for extending we just check all lines of sight in the appended frame against already found trajectories.

For initial search we try to find a trajectory for a given set of lines of sight. For each additional image we test whether its lines of sight extend any of the found trajectories, but we do not check all possible line of sight combinations in the extended set, that allows us to save computational time.

Trajectory determination is implemented differently for moving and non-moving particles. In the simple case of non-moving particle we just look for a point in space that is close enought to all lines of sight. For moving particles the scheme of search for the trajectory is shown in fig. 4.17.

4.3.5.1. Software implementation

All described algorithms were implemented in C++. Each step was tested individually. The software can be seen as consisting of the following major parts:

Suspicious pixels detection module analyses camera images and produces lists of pixels (in image coordinates) that might be images of a particle. This is rather simple program and it can be applied to any cometary images.

Pointing retrievals module transforms the list obtained at the previous module from image coordinates into the frame connected with the comet nucleus. Additional required information (*e.g.* timing, Sun phase) is taken from the images' metadata. This step produces lists of boresight vectors with attached time and brightness information. This step creates an ASCII table file which contains all the required information about suspicious pixels for the automatic search of particles. Significant part of this module implementation is designed specifically for HMC.

Particles detection module takes boresight vectors list and searches for probable particles trajectories. It outputs list of found trajectories (if any) with detailed description of each one (including lists of suspicious pixels and camera images). This uni does not know anything about camera and can be applied to any cometary data.

Each module is implemented as independent application and the units communicate by passing data from one to another (there are no inter-module calls).

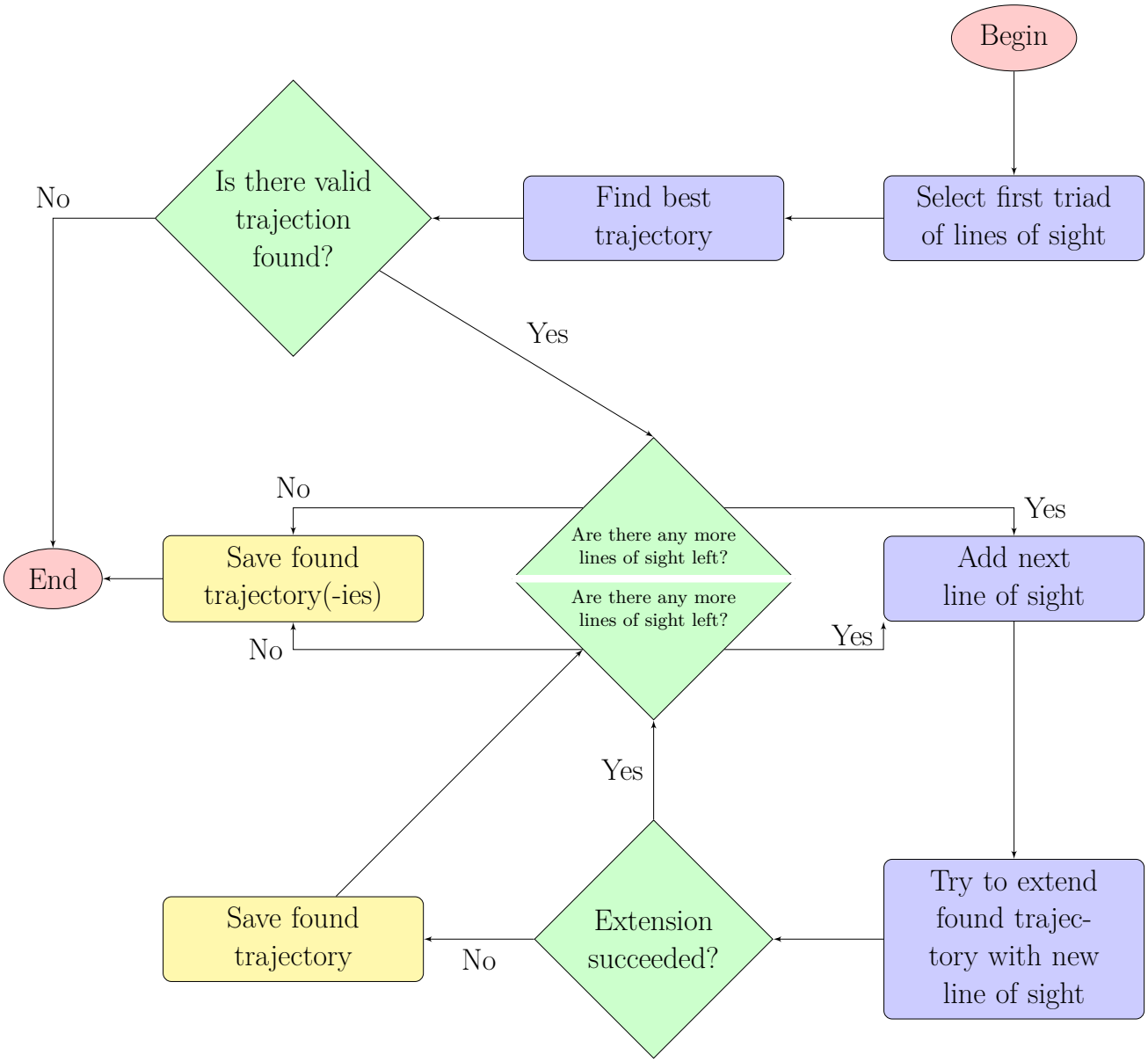

Figure 4.17.: Scheme of algorithm of particles search.

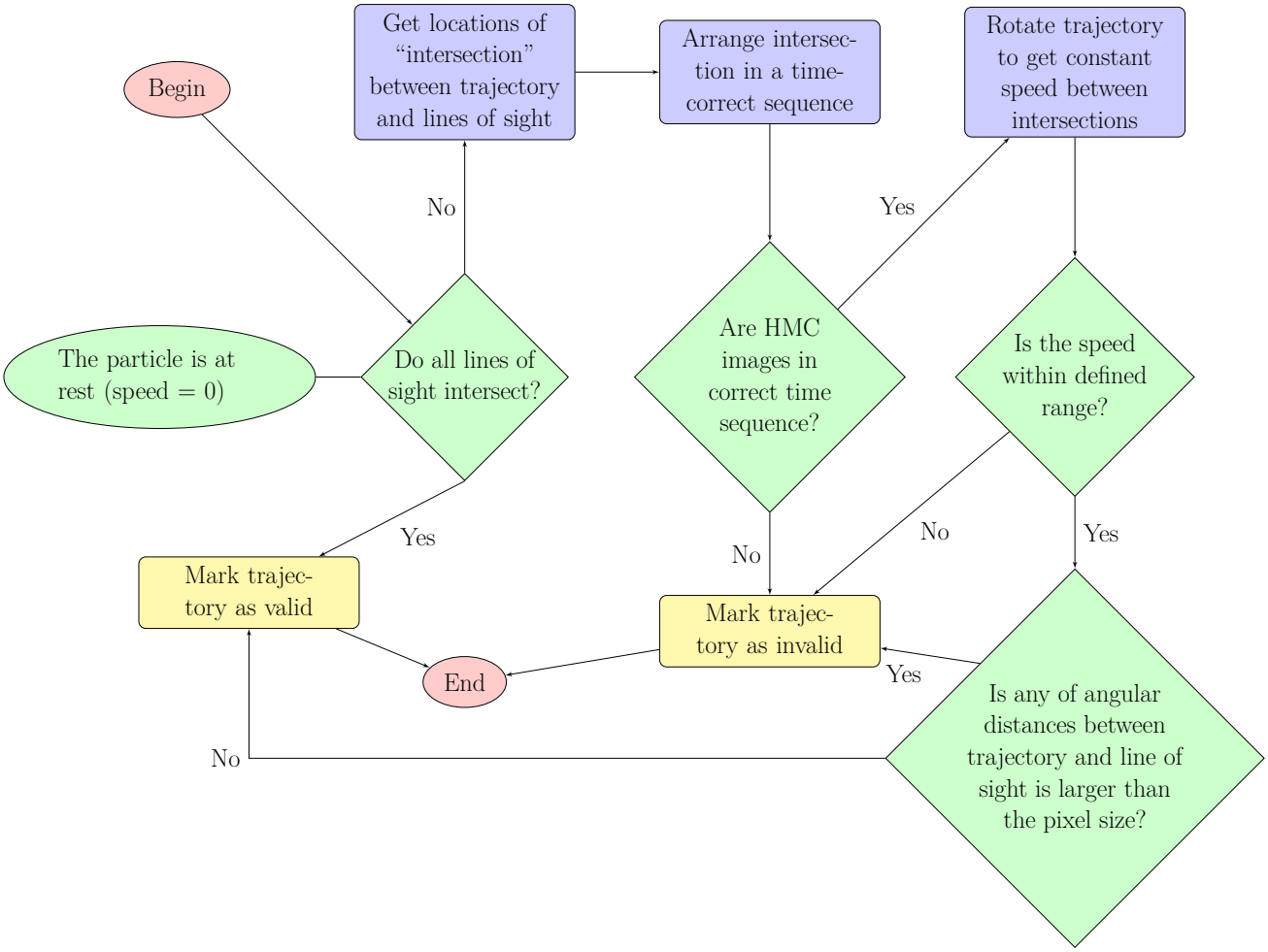

Figure 4.18.: Scheme of algorithm of trajectory checks. These actions are performed when initial trajectory is found (using three lines of sight) and when a trajectory is being extended.

4.3.5.2. Software testing

Parts of the algorithm and the implementation can be tested independently. The suspicious pixels finder can be tested manually using HMC images or automatically using artificially generated ones. Pointing computations can be partially tested against HMC rectified images: if it can reproduce the geometrically corrected ("rectified") HMC images, one can conclude that corrections for camera and observational geometries are correct. Particles detection module can be automatically tested using artificially generated boresight vectors lists.

Trivial tests of programs which prepare data for automatic steps were done (*e.g.* work with image metadata).

Successful testing has been done for the suspicious pixels detection and particles detection units. In particular, the manual testing was performed for the suspicious pixels detection and automatic for the particles detection units. For the particles detection testing various artificial configurations were used, with non-moving particles and particles moving with various speed and acceleration.

For the particles detection unit performance testing was done. About 1000 boresight vectors were processed. This special artificial set contained closely placed particles, and depending on required accuracy, can yield huge number of trajectories. The algorithm and implementation do not have any special requirement for memory size and thus we've ran it using ageing (at the time of writing) laptop with Core i7 720 QM CPU and Core i7 4810 MQ CPU. This system was able to find all trajectories in the test set in about 4 and 2 hours correspondingly (search for the non-moving particles is even faster). Using more powerful computer can increase the speed of work. Thus we concluded that performance of this unit is satisfactory.

Tests of the pointing retrieval unit revealed insignificant differences in the rectified images produced by the software and the ones prepared by the HMC team. Precise pointing information is crucial for the particles detection, and correct accounting for the changed of field of view (FOV) for different pixels, caused by the fact that every image was a part of cone, was needed.

To restore lines of sight for HMC pixels one needs to know where the camera was and how it was oriented at the time of imaging. This information is given as barycentric co-ordinates of GIOTTO, the Sun and the Halley comet (for positions) and sun elevation and azimuth with respect to the camera optical axis (for orientation). These two sets of co-ordinates have to be consistent. However, if one computes the angle Sun-GIOTTO-Halley in both systems, these two angles do not match. In the barycentric system the angle is computed via Cartesian co-ordinates, in the second system it is computed knowing position of the comet in the image. Even if the geometry of the image is incorrectly known, mistake can not be more than the FOV of the HMC (0.09°), while actual difference raises with the frame number and reaches more than 1° for image number 3 500. Another source of the barycentric co-ordinates is SPICE kernel for the GIOTTO and Halley comet, released together with the HMC dataset. With these co-ordinates the angle are not equal too with the same level of error. However, our co-ordinates transformations are not much sensitive to the elevation of the Sun because the uncertainty is in plane, almost perpendicular to the optical axis due to geometry of observations. Thus the obtained error is insignificant for the final conclusion.

4.3.5.3. Results

A potential presence of particles in the HMC images has been analysed. Suspicious pixels have been taken from the unprocessed HMC images (numbers 3 436 – 3 493, distances from the camera to the nucleus are 20 000 – 4 000 km, MDM), and thus they include random noise. The only difference between possible particle images and random noise is space coherence of the formers. The list of suspicious pixels for every image and all needed information for further calculations was formed into the ASCII file. Algorithm of particles search and corresponding software were

developed. A comprehensive analysis was performed to test whether these pixels might be images of particles seen as stable objects or moving along straight lines with speeds between 0 and $500\,\mathrm{m}\cdot\mathrm{s}^{-1}$ with respect to the comet nucleus: calculations of lines of sight for suspicious pixels and searching the intersections between them for different images were done. If a set of lines of sight from different images intersects in a given vicinity of a certain point or these lines are displaced from a certain particle trajectory for not more than a given angular distance we assume that a particle is detected. The geometrical distortion was taken into account for restoring the pixels field of view, and transition from image coordinate system to the comet reference frame (Cartesian barycentric system with origin shifted to the comet) was performed.

The testing was done assuming possible angular error in pixel bore-sight vector directions up to $2.26\times10^{-4}\,\mathrm{rad}$ (10 HMC pixels). The test yielded no detected particles, *i.e.* HMC did not detect particles with radius larger than 1.5 m (in case of dark particles).

We plan to apply the developed algorithm to the data obtained by the other cometary missions.

5. Summary 1: Searching the large grains at GIOTTO/HMC images (comet 1P/Halley)

1. The full HMC data set was stored on CD-ROMs and magnetic tapes in VMS format. The CD-ROMs have been read and the data from them stored. Not all of HMC backup tapes survied and thus not all data from them have been recovered. All available HMC data obtained during the Giotto mission stored in different places were collected and prepared to place them into a single data archive. Additionally, image headers were converted into the PDS labels.

2. Checks for reliability of the radiometric calibration of HMC images in the range of very weak signals were done. Problematic images were identified.

3. The preliminary testing of the Richardson-Lucy method in application to the HMC data was done on the example of the Earth images.

4. Estimations of particle detectability by the HMC camera was done. Dusty particles with radii of about $1-1.5\,\mathrm{m}$ and larger can be detected at the closest approach (in case of icy particles, the size decreases to centimetres). Obtained values are in accordance with the estimations made for comet 103P/Hartley 2. It was found that particles will look as unmoving objects in subsequent images, which allows for simple SNR increase.

5. According to the estimations of particles detectability, the set of images with numbers $3\,436-3\,493$ (distances from camera to nucleus are in range of $20\,000-4\,000\,\mathrm{km}$) was selected for searching the evidence of large particles ("flight" level of processing, MDM, detector C, clear filter).

6. Two algorithms were proposed for searching the particles in HMC images, and corresponding software has been developed.

   a) The first one, "Image differencing method" (IDM) is more simple, and works with image differencing. Software for superposing images was developed, and it was found that the difference between the images in selected sequence does not decreases significantly after reaching alignment accuracy of $0.25\,\mathrm{px}$. This method was found not perspective because it is not accurate enough, and does not allow to make tests of plausibility of the results of searching the particles.

   b) The second one, "Automatic method of the large particle detection" (AM) is more sophisticated and needs more developing, but it is much more accurate than IDM method, and has benefits that image differencing method does not have. Thus, it was chosen for further developing.

7. Software for AM algorithm for particle detection (section 4.3) was implemented.

   a) All software blocks have been successfully tested using known information from HMC images, and artificial data sets (*e.g.* for detection the trajectory of a moving particle).

b) An algorithm and its optimal parameter values for suspicious pixels selection from the unprocessed HMC images were suggested: deviation of more than 4σ from the surrounding region with size 7×7 pixels in the images, processed by the diagonal Laplace filter. This results in selection of about 60 suspicious pixels per image, that are distributed not only in the comet jet areas.

8. A potential presence of particles in HMC images has been analysed.

   Suspicious pixels have been taken from the unprocessed HMC images. A comprehensive analysis was performed to test whether these pixels can be images of particles seen as stable objects or moving along straight lines with speeds between 0 and $500\,\mathrm{m}\cdot\mathrm{s}^{-1}$ with respect to the comet nucleus. For that retrievals of lines of sight for the suspicious pixels and consequent search for the intersections between them in different images were done. The test yielded no detected particles, *i.e.* HMC did not detect particles with radius larger than 1.5 m (in case of dark dusty particles).

Problems and possible solutions:

Not all data that were expected to be stored are available due to technical reasons (data in original flight format, Altair images, PSF obtained using the Altair images are examples of the data that seem to be lost). But this is not critical for the current project and can not prevent us from getting the planned output. The PSF obtained using the Altair images could be replaced from the PSF obtained by the other star observations.

Planned update of the research:

Developed software can be applied to the analysis of data from another experiments. The only work needs to be done is to transform image coordinates into boresight vectors in the nucleus frame. Therefore the software can be used not only for HMC data but also could be reused to analyse the data obtained for the other comets listed in **Phase 2** Task 2 of the current project.

Conference attendance:

This work was presented at European Planetary Science Congress 2015 (27 September – 02 October 2015, Nantes, France) [28].

6. Testing the algorithm using DIXI data (comet Hartley 2)

6.1. Motivation

After retrieving the negative result of particle search near the Halley comet (see the previous chapters), we decided to apply our software to the images of comet 103P/Hartley 2 (hereafter, H2 or 103P) obtained by Deep Impact spacecraft (EPOXI mission), because it is known that coma of this comet has a significant population of large particles observed as a point sources in images [29, 17, 1], so performing the particle search at such data is a good test for our software on real data.

6.2. Applying the software to DIXI data: general algorithm

As at previous study with analyzing HMC data (see section 4.3.1), the particle-detection algorithm consists of three main blocks (see fig. 6.1):

1. Detection of suspicious pixels (whose brightness significantly differs from that of surrounding pixels) in images.

2. Finding all possible trajectories that can produce these pixels.
   - Firstly, we have to calculate the line of sights for the suspicious pixels in 3D space. For this we need the precise pointing.

3. Validating the derived trajectories: the valid ones have to start at the nucleus, the velocity of the particle along the trajectory has to stay constant within reasonable limits, and trajectory intersections with the boresight vectors have to be in the correct order.

What we expect from the algorithm is the confident detection of pixels that contain probable images of a dust/ice particle, which stays or moves along a straight line in space.

6.3. DIXI data

EPOXI uses the Deep Impact spacecraft in a campaign consisting two missions: the Deep Impact Extended Investigation (DIXI) and Extrasolar Planet Observation and Characterization (EPOCh). DIXI aimed to send the Deep Impact spacecraft on a flyby of another comet. It was successfully sent the Deep Impact spacecraft on a flyby of comet Hartley 2 and closest approach to 103P/Hartley occurred at 10 am EDT on November 4, 2010, passing to within 694 kilometers of this small comet. The flyby speed was 12.3 km/s. The spacecraft employed three science instruments: two telescopes and an infrared spectrometer. The point sources around H2 are found in visible wavelength images taken with both the High Resolution Instrument (HRI) and the Medium Resolution Instrument (MRI) [29, 17]. It was the first images of sub-meter particles from a comet seen as indovidual objects. Prior images in visible/infrared light (*e.g.* [30, 31, 32]) and with radar [33] probed collections of many large particles.

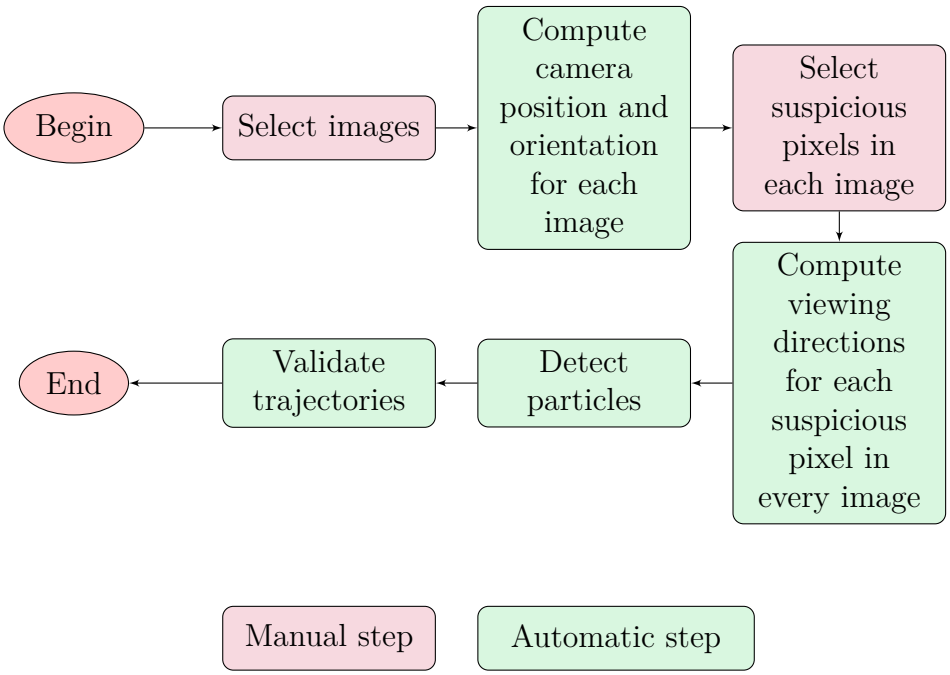

Figure 6.1.: General scheme of algorithm of particles detection for Hartley-2 data. Parts of it are described in details in subsections below.

Images of Comet 103P were taken with Deep Impact's Medium Resolution Instrument and High Resolution Instrument CCD cameras. Both cameras have 1024 x 1024 pixel arrays; the HRIVIS pixel scale is 0.41300 pixel^{-1} (2 μrad), and the MRI pixel scale is 2.0600 pixel^{-1} (10 μrad). The instruments are described by [34], and their calibration by [35]. The MRI and HRIVIS data are available *e.g.* in the NASA Planetary Data System (PDS) archive. Images taken with the MRI are labeled with the prefix "mv", and for the HRIVIS the prefix is "hv"

6.3.1. Known results about the large particles evidence

There are two important papers which present results concerned to the investigation of large particles near H2. The first one, [17] presented measuring the photometric properties of the large particles in the coma of comet H2; they convert their fluxes into sizes, discuss their spatial distribution, attempt to constrain their composition, and compare them to large particles observed in radar observations. Two possible particles compositions were examined: dusty case (low albedo, 0.3 g/cm^{-3}) with size limit ranging from 10 cm to 2 m in radius, and icy case (high albedo of Jovian satellite Europa, 0.1—1.0 g/cm^{-3}) with size limit ranging from 1 to 20 cm in radius (0.3 g/cm^{-3}). Authors considered the icy case to be more likely than the dusty case because of the several reasons: the icy particles are more easily lifted by gas drag; they account for the sunward/anti-sunward asymmetry in the particle distribution if ice is sublimating on their sunlit sides; and the total large particle mass for the dusty case is much greater than the total mass of the nucleus. Later in erratum to this paper [36] authors increased their estimations of grains radii up to 30 cm in icy case (with an estimated population mass within a 20.6 km aperture of $0.2—6 \cdot 10^{10}$ g, or up to 0.02% of the nucleus mass), and up to 4 m for dusty case (total population mass of $0.1—3 \cdot 10^{10}$ g, or 0.6—14% of the mass of the nucleus, potentially exceeding the estimated orbital mass-loss rate of the comet).

The large particles and the total coma have different spatial distributions. Specifically, the coma is dominated by the jet activity, but the large particles are not and instead have a distinct asymmetry toward the anti-sunward and night-side directions. In this work authors discuss four potential causes for the asymmetry: ejection history; solar radiation pressure; the rocket

effect from sublimating water ice; and, hydrodynamic flow. The ejection history of the particles depends on their source locations and the rotation state of the nucleus, both of which are loosely constrained. Ejection asymmetries can play a role, but on their own they do not appear to be able to account for the observed large particle distribution. Solar radiation pressure is weak, but can still be significant, depending on the (unknown) particle density and scattering behavior. Ice sublimation has a strong effect on the particle dynamics, potentially stronger than solar gravity.

The second one, [29], is more important for our work, so we will put more attention on it. In this research authors performed an analysis of the identification, localization, and dynamics of particles present in the encounter images taken around closest approach. The goal of this work was to identify and locate the brightest particles surrounding H2 to understand their positions, evaluate their possible motions, and tie dynamics to grain properties. In that work authors concentrated on the 31 encounter images taken during the 3 min bracketing closest approach (mainly on MRI images). All images were obtained with the broadband "CLEAR" filter to maximize the signal to noise ratio at closest approach; integration times also varied during this time period: from 40 to 120 ms for MRI and 125 to 375 ms for HRI.

Bright point sources, described as "particles" were detected near the nucleus in the MRI and deconvolved HRI images. These particles, interpreted to be composed primarily of water ice [1] were detected at a high density near the nucleus [17]. Most particles are consistent with point sources in the MRI camera and are therefore interpreted to be $\lessapprox 7$ m in diameter. This camera yields an even smaller upper bound on their possible sizes since the HRI camera theoretically has a factor of 5 better resolution than the MRI. Due to a flaw in the pre-launch calibration of the HRI, however, the instrument is out of focus [35]. Deconvolution routines an restore much of the lost clarity. As the images around the closest approach of H2 were returned from the spacecraft and viewed temporally, it was visually apparent that not only were there thousands of bright particles in each frame but that the same particles seemed to persist in subsequent images and follow discrete paths during the encounter. The apparent motion of the particles comes primarily from the motion of the spacecraft cameras (translation and rotation) as they flew past the comet. Thus, the magnitude and direction of the apparent parallactic motion of a particle is dictated by its distance from the comet (the approximate center of rotation). Many of these particles can be identified throughout a number of encounter images. The motion of the spacecraft instruments relative to the nucleus (including not only spacecraft flyby velocity but also pointing adjustments) provides a metric to estimate the location and displacement of these particles by stereoscopic reconstruction of particle locations in successive frames (see fig. 6.2.

Due to the large number of bright spots (or "candidate" particles), in this work the areas that are at least 2 sigma above the background threshold were identified in each image (as an criterion). Images were processed via a high-pass filter to enhance the visibility of the particles. The background is estimated from a box centered on each particle excluding any comet surface, thereby permitting its use as a threshold value. This strategy serves to make the analysis tenable, but does bias the results to the brighter (and thus, probably larger) particles. The brightness of each individual particle is highly variable between images however, with most appearing and disappearing several times during the flyby. While the HRI exhibits a theoretical factor of 5 improvement in resolution over the MRI, the MRI is in focus (without the need for deconvolution), and, more importantly, has a significantly higher temporal resolution during encounter (with 5 s between images during closest approach). As a result, many of the same particles can be located in multiple MRI frames; this is not the case for the HRI. So in that work authors therefore focus on the MRI images for determination of the positions of the particles [29].

The results presented in this work were calculated from 114 unique particle identifications (*e.g.*, 3 or more detections) over the 31 images surrounding closest approach. The average number of images in which a given particle was detected was 13.9; this is approximately equal to the median number of detections (13.5). Of the located particles, 6 were detected in only

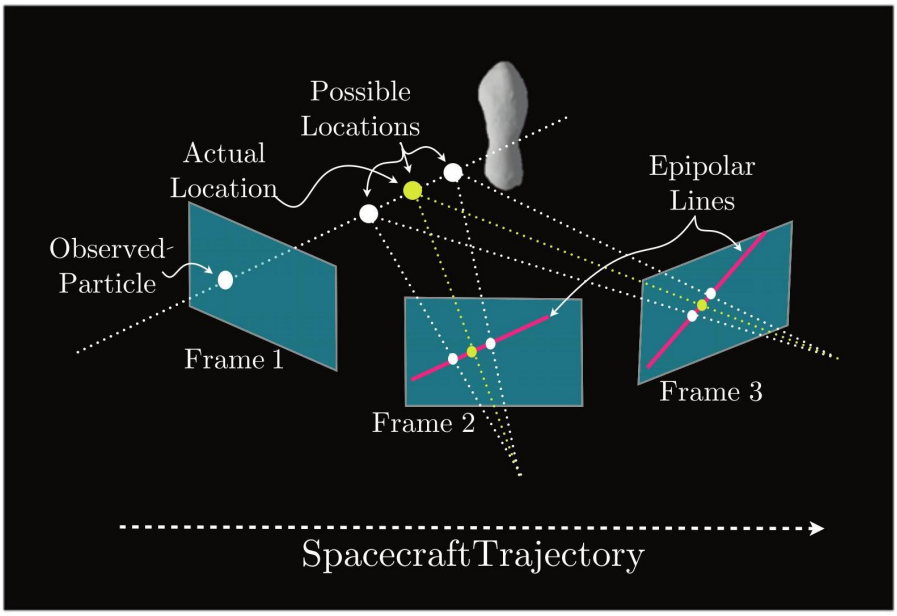

Figure 6.2.: Scheme of the epipolar geometry employed in the reconstruction of the particle locations. The 3D location of a particle identified in only frame 1 of the illustrated sequence cannot be uniquely determined. The solution space can be mapped into an "epipolar line" in subsequent frames based on their respective viewing geometries. The correct particle identification between frames will match in reconstructed 3D coordinates throughout the encounter (within some reconstruction error or intrinsic motion of the particle). (Image was taken from [29]).

the required minimum of 3 images; 2 particles were detected in the maximum of 29 images (see fig. 6.3a). The majority of the detected particles are located within 10 km from the center of the nucleus (fig. 6.3b) and were traveling a few meters per second or slower.

6.3.2. Selecting the images

For our purposes it is better to use the close up images. It is also has sence that data set chosen for current work should follow the data were used in work [29] (taken during the 3 min bracketing closest approach, "CLEAR" filter) by the same reasons: they exhibit the greatest number of measurable and identifiable particles; in case if SPICE accuracy of pointing retrieving would be not enough (that was found to be a case, see section 6.4.1 below) for restoring the geometry of observations, we will need to utilize the control points (features on the nucleus), that are well-resolved in close-up images; the parallax between subsequent images is sufficient to allow stereoscopic reconstruction.

As in work [29] we will focus only on MRI images, because MRI was in focus (without the need for deconvolution), and, more importantly, had a significantly higher temporal resolution during encounter (with 5 s between images during closest approach), although the HRI exhibited a theoretical factor of 5 improvement in resolution over the MRI. Images taken with the MRI are labeled with the prefix mv. We keep this convention through document.

We will use calibrated images Level 3 RADREV (level is RADREV for calibrated but uncleaned data in units of radiance, calibration steps can be reversed to get back to the raw DN) from the PDS archive [37] (detailed description of MRI calibration, and the PDS data description could be find *e.g.* in [35] and [38] correspondingly).

Following images meet the criteria and form working set of 24 images (see details in chapter F): starting from mv10110413 _5004029 _001 _RR.FIT (distance from camera to nucleus was D =

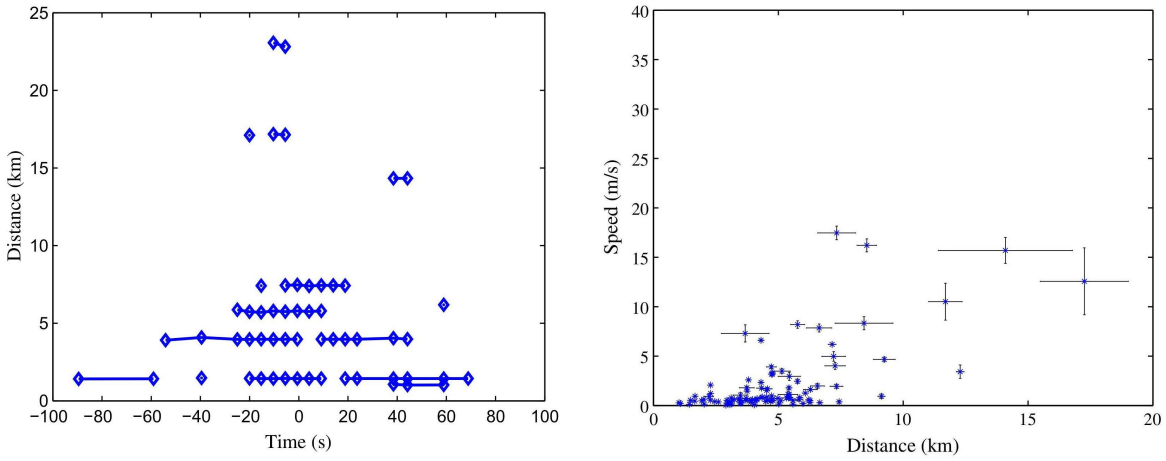

(a) **(b)**

Figure 6.3.: (a): distance of a selected at work [29] set of particles from nucleus center versus time relative to closest approach; connected diamonds mark the same particle identified in subsequent images. Note temporally varying nature as particles drop beneath the noise floor only to reemerge at a different viewing geometry. (b): particle speeds (absolute value of velocity) versus distance from center of nucleus (the error bars are 1 sigma uncertainties from the robust regression of position and velocity). (Plots were taken from [29]) .

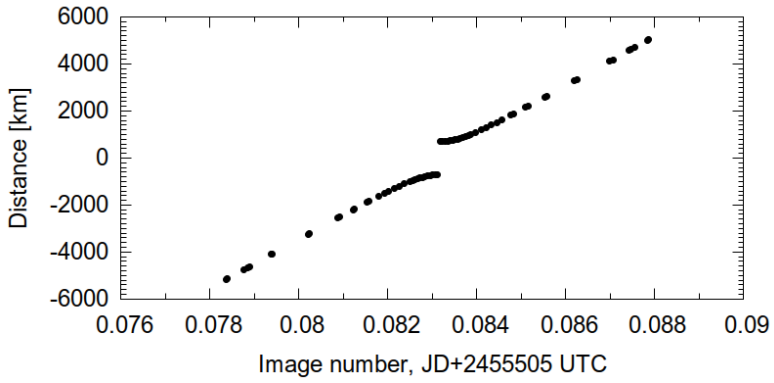

Figure 6.4.: Geometry of flyby.

963.144 km), with the closest image mv10110413 _6000002 _001 _RR.FIT (D = 694.051 km), and the last one mv10110414 _5004064 _001 _RR.FIT (D = 1004.451 km) (see fig. 6.4).

6.3.3. Selecting the suspicious pixels

As easily seen from example of image, there are a lot of bright points in typical MRI image fig. 6.5. The procedure of the suspicious pixels selection was the same as for HMC data (see section 4.3.2). It was decided to use 5σ cut-off level to reduce value of suspicious pixels (as easily seen from example of image, there are a lot of bright points in typical image). Figures 6.6 and 6.7 demonstrate the examples of influence of different surrounding regions size. Size 7×7 pixels was chosen as optimal, and this result in selection about 2 thousands of suspicious pixels per image.

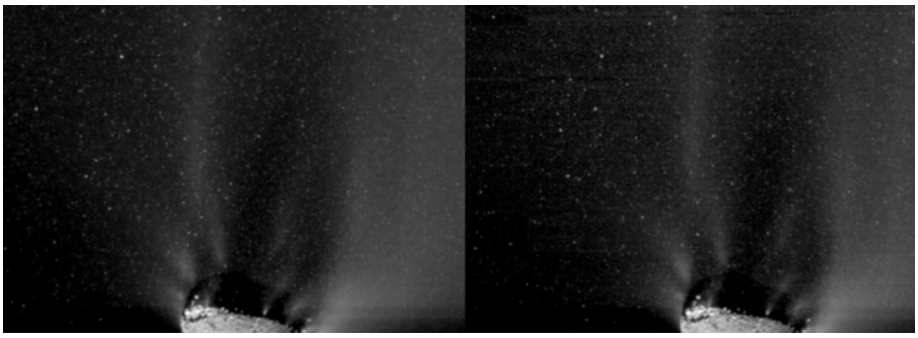

Figure 6.5.: Fragment of images, is a stereo view (cross-eyed viewing technique) of processed MRI images to illustrate the stereoscopic parallax caused by the motion of the spacecraft and instruments. Images were stretched to enhance both particles and jets.

Table 6.1.: Information about images used for test.

Image N "mv10110413"+	MidTime 2010-11-04	Dist [km]	Pixel Scale [m/pix]	Phase Angle [°]	Total integr.time [msec]
"5004029"	13:58:53.085	963.329	9.633	79.8664918	120.5
"5004032"	13:59:07.747	848.102	8.481	79.3093093	40.5
"5004041"	13:59:22.289	759.412	7.594	78.9720089	120.5

6.4. Retrieving the required accuracy for particle search

6.4.1. Accuracy of pointing given by SPICE

For testing the SPICE ephemerids accuracy, the following test war performed: the coordinates for several points at the nucleus image were determined manually for several images, and SPICE was called to give positions of this points at images, and the displacement between measured and calculated by SPICE coordinates was calculated. It was found that the accuracy of SPICE solution it is much worse that it is needed, and it is good to only $\sim$ 10 pixels instead of 1 pixel (see fig. 6.8). Faced with this problem we become to search better approach of retrieving required accuracy.

6.4.2. Different approaches of getting the required accuracy

6.4.2.1. General idea

Since the accuracy of SPICE kernels is not sufficient, we had to find a way to improve it. Objects on the surface of a comet nucleus can be used as reference point for pointing determination. Locations of these objects do not change with time (in the nucleus frame). If we have enough objects in each image and do know their exact co-ordinates (in the nucleus frame), we can determine pointing parameters for each image independently. If any of these conditions is not fulfilled, we need to use a sequence of images at once, probably with information about the spacecraft trajectory.

An overview of the pointing determination (adjustment) algorithm is shown in fig. 6.9. We use values from SPICE as the initial approximation and then adjust them to reach the required accuracy. Too approaches were developed: the one which does not rely on reference object co-ordinates known in advance, and the one which does. Below we will describe the both approaches and their outcomes. In this description we will use a (pseudo-)inertial frame, which is bound to the comet nucleus.

In this frame we define the following:

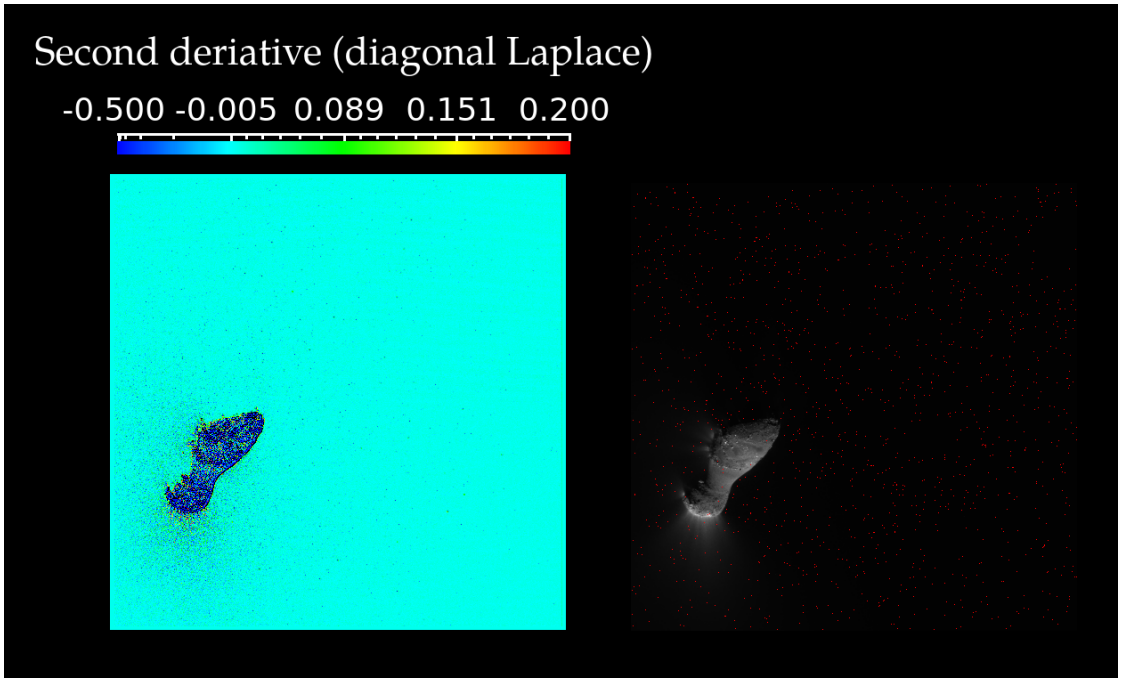

(a) right: 3x3 pixels (5396 points).

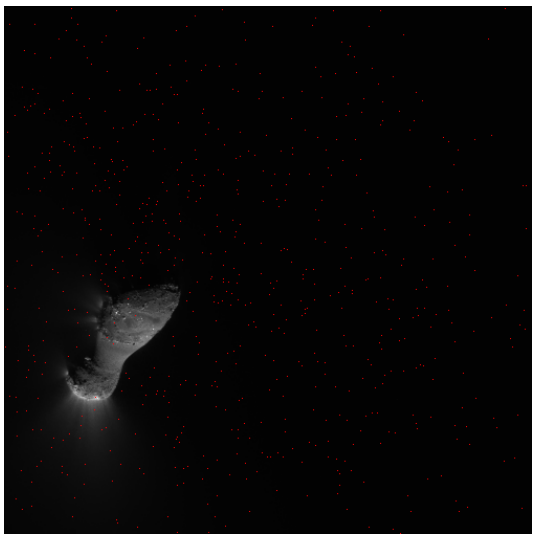

(b) 7x7 pixels (2643 points).

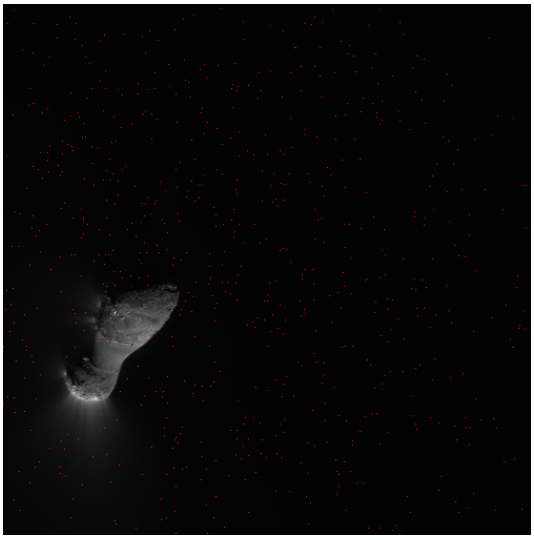

(c) 11x11 pixels (2818 points).

Figure 6.6.: Example of suspicious particles distribution for MRI image mv10110413-5004051, clear 1 filter, 696 km (first image after closest approach), gamma 4, cut-off level is 5σ for all subimages. (a): second deriative image (left), prepared the same as was described at section 4.3.2, and result of the pixels selection for the square "window" size 3 x 3 pixels produce 5396 points (right). Amount of selected suspicious pixels for marked sizes of "window" shown at (b) and (c) .

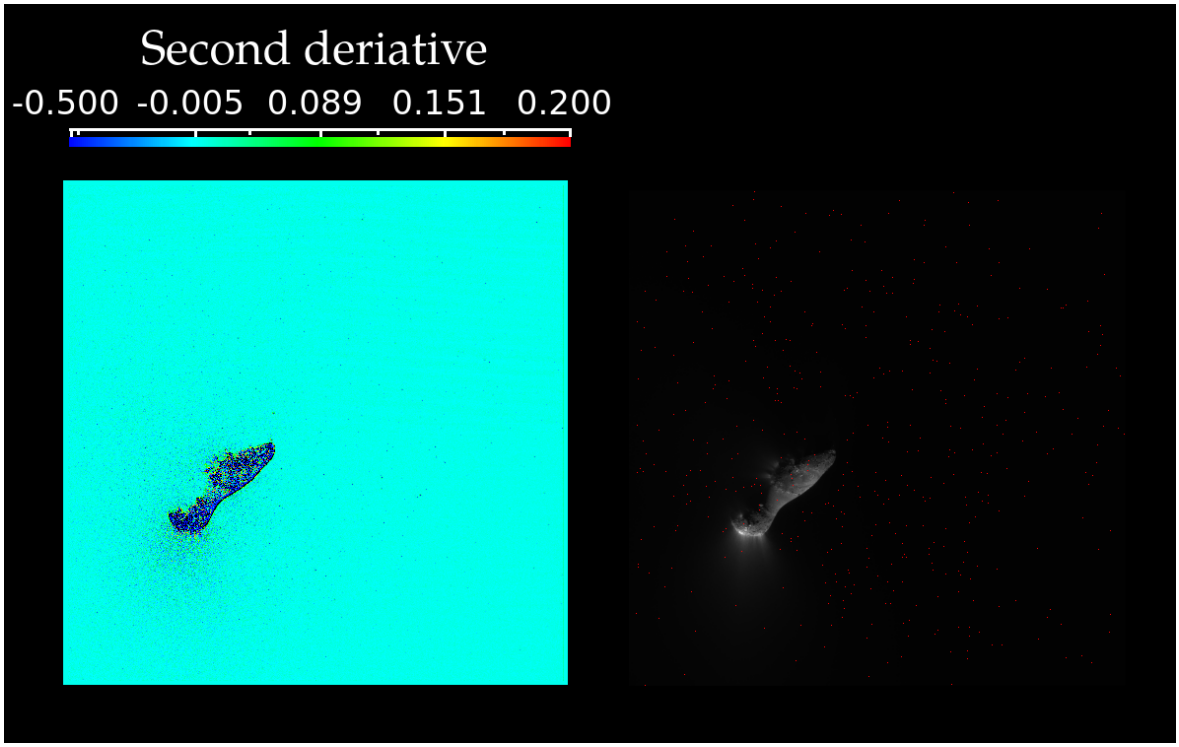

Figure 6.7.: Example of suspicious particles distribution for another MRI image mv10110414-5004061, clear 1 filter, 882 km (after closest approach), gamma 4, cut-off level is 5σ, square "window" size is 11x11 pixels result in the selection of 1881 suspicious pixels.

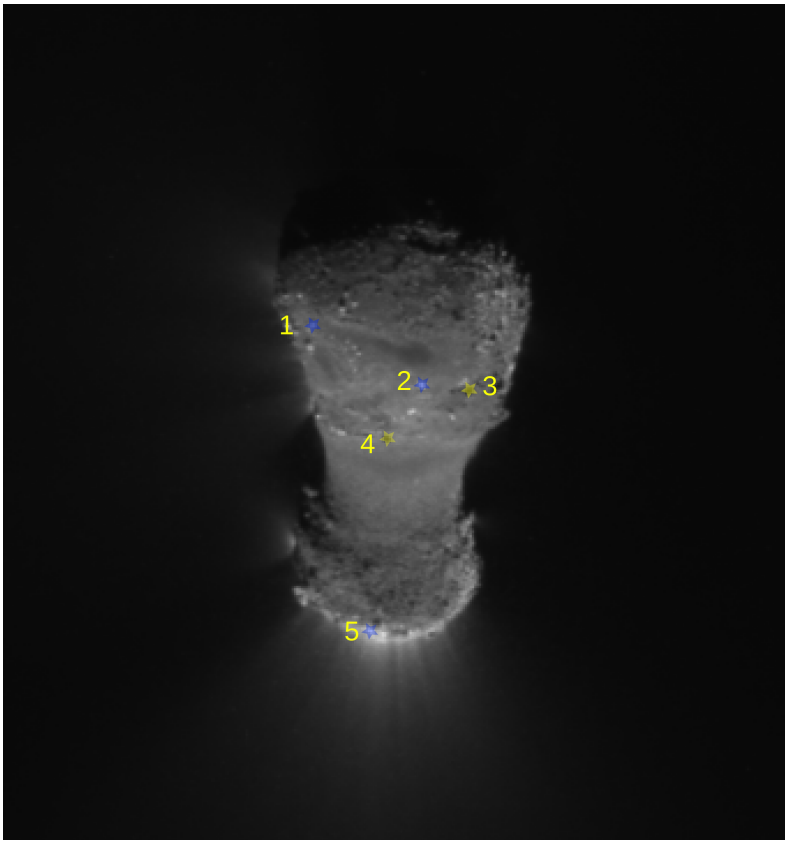

Figure 6.8.: Retrieved displacement for 5 points for set of 3 images (see section 6.4.1) marked at image by stars: 1 – 9.6806/2 pix, 2 – 7.9153/2 pix, 3 – 6.8813/2 pix, 4 – 4.7208/2 pix, 5 – 7.7473/2 pix.

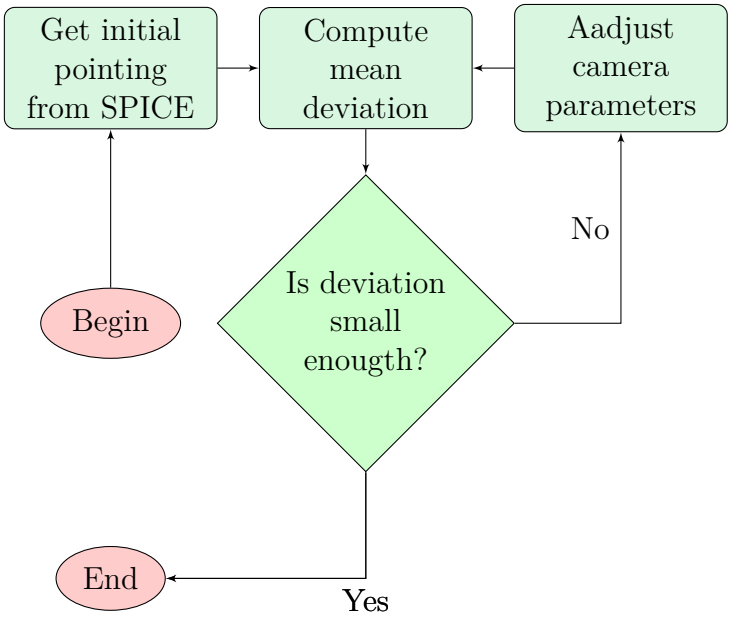

Figure 6.9.: General scheme for pointing determination.

1. Positions and orientation of the camera for time moments of each image.
2. Positions of the reference objects.
3. Trajectory of the spacecraft.

We compute projections of the reference objects onto the image plane and compare them with the actual positions, measured in images. Then we adjust the above mentioned values until the difference between the measured and projected locations becomes small enough (we target less than 1 px).

Two methods were tried: per-frame fitting and an integrated processing for a sequence of images. For the first method (described in section 6.4.2.3) one needs too know exact co-ordinates of the reference objects, while for the second method they are required as initial values. For the second method (described in section 6.4.2.4) we have to assume that the spacecraft trajectory is a straight line and spacecraft position is defined by a shift along this line. However, if we do not know reference objects location at all, we can try to get their positions from the images too. We started from this method and them moved to others (see below why).

6.4.2.2. General fitting with little constraints

The images of the nucleus bear many easily identifiable details (see *e.g.* fig. 6.13). Having an image sequence and assuming that the reference object positions do not change, we a set of spacecraft positions and camera orientation to fit all the objects with its image locations. For this work we measured locations for ≈ 40 objects (note, that part of them is not visible in some of the images due to the nucleus rotation in the field of view). Then we defined the following variable quantities:

Camera position 3D vector which defines spacecraft positions with respect to the nucleus frame.

Camera orientation Three angles that define the orientation of the camera. Two of them define viewing direction (optical axis) and the third one defines position angle (rotation around the viewing direction).

Reference object positions defined by 3D Cartesian vectors.

The fitting procedure was minimizing

$$\sum_{i=0}^{n}\sum_{k=0}^{m}\left|\vec{p_k^i} - M^i(\vec{r_k})\right|^2, \tag{6.1}$$

where i is image index, k is reference object index, $\vec{p}$ is location of the reference object projection in image plane, $\vec{r}$ is its space coordinates, and M is the function which maps space coordinates onto the image plane.

The fitting was done using an optimized Nelder-Mead method [20]. In principle, similar methods are used to reconstruct the shape of the comet nucleus. However, we did not reach the state where the method returns unambiguous results. Therefore we decided to add more *a priori* information in the form of know reference objects positions.

6.4.2.3. Per-image fitting with constant reference objects

If reference object coordinates are know well enough, it is possible to restore camera orientation using just two of such objects. Then only orientation of the camera may be changed to fit the reference object positions in an image.

Dr. Farnham provided us a table with coordinates of the two points measured by him in images [39]: the center of the nucleus, and position of the bright spot on the end of the large lobe of the nucleus (please, see these points marked in figs. 6.14 and 6.17). He claimed that he estimated that these were good to a level of at least 0.5 pxin most cases. Using very well known information about two points in space (from the shape model of H2 nucleus [40], see images figs. 6.16 and 6.17) and in images it is possible to restore the position and orientation of the camera, and get better accuracy of pointing than that given by SPICE.

In the shape model the bright spot location was measured (several probable position of it, because it was not easy to identify it place at the shape model). Before using these data, the following simple test was performed: the angle between directions to this point and to the nucleus center was computed and compared with distance in pixels between their projections in Dr. Farnham file (S/C co-ordinates were taken from the SPICE kernels) (see details in chapter H).

A plot of difference on line number resembles a sinusoidal function (please, see fig. 6.10a), that was strange, and difference reached up to 35 pixels.

Then it was found that for the images in which we may see the very well pronounced black detail (shadow), to which the shape model center meridian (0° longitude) was tied, the sub-spacecraft longitude in image header (and the same in SPICE kernels) is about 151°, that is definitely wrong (see fig. 6.11). There are coordinates of the S/C in the headers, in fields $[(REC)or(NOM)]SCLAT$, $[(REC)or(NOM)]SCLON$, $[(REC)or(NOM)]SCRNG$ which do not differ much from the values, returned by SPICE. If we take an MRI Hartley2 image, where the dark boulder located near the centre of the visible part of the nucleus, the header shows $[(REC)or(NOM)]SCLON$ about 150°. For instance, for one of the image 5004032_001_$rr.fit$ (see fig. 6.11): NOMSCLON = 151.750938847 [deg] Sub-spacecraft IAU longitude.

At the same time, the shape model shows, that central meridian is very close to the dark boulder, *i.e.* zero longitude is very close to the boulder (please, see images figs. 6.11 and 6.14). Moreover, longitudes in SPICE and headers follow left hand rule, while IAU requires right-hand rule (longitude increases when going from X axis to Y axis in right-handed system).

Dr. Farnham found that he used another orientation constants than those defined in the SPICE kernels (see image fig. 6.11), and provides them for us. Using these constants we get realistic sub-spacecraft longitude values (for example, it was changed from 151 to 356 degrees).

Also it was found in the description to SPICE kernels [41] that some wrong comments are present (*e.g.* in some places instead of comet Hartley 2 the Tempel 1 comet was written). And it was claimed that these data are in consistency with [42], but as it was found this is not the case.

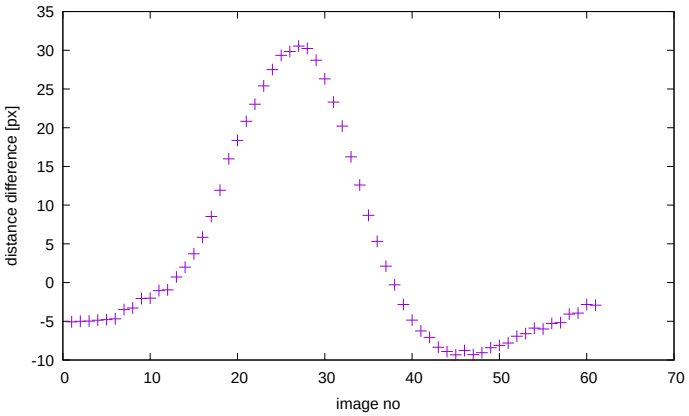

(a) Using original SPICE kernels. Sequential image number is shown in X axis.

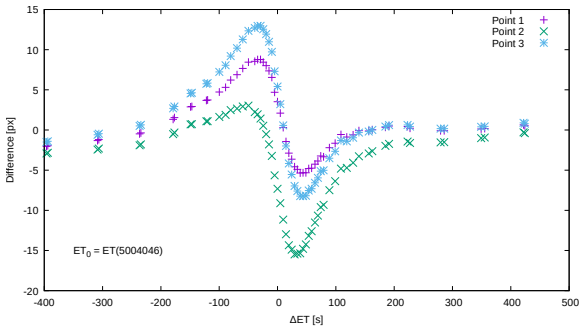

(b) Modified SPICE kernels. The X axis is ephemeris time.

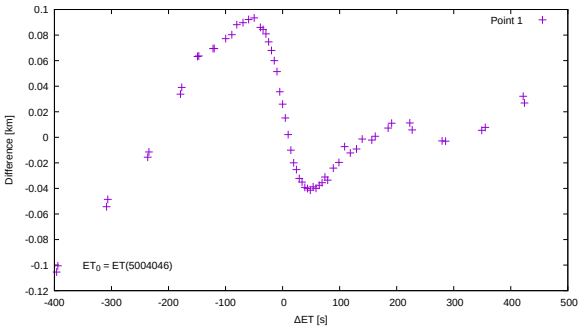

(c) The same as (b) for point 1, but angle is converted into distance in image plane, taking spacecraft to comet distance from SPICE.

Figure 6.10.: Results of the test for the data given by Dr. Farnham. The plots show difference in angles between directions from camera towards two reference points, computed from images and from 3D object coordinates. With ideal pointing these two angles have to be equal.

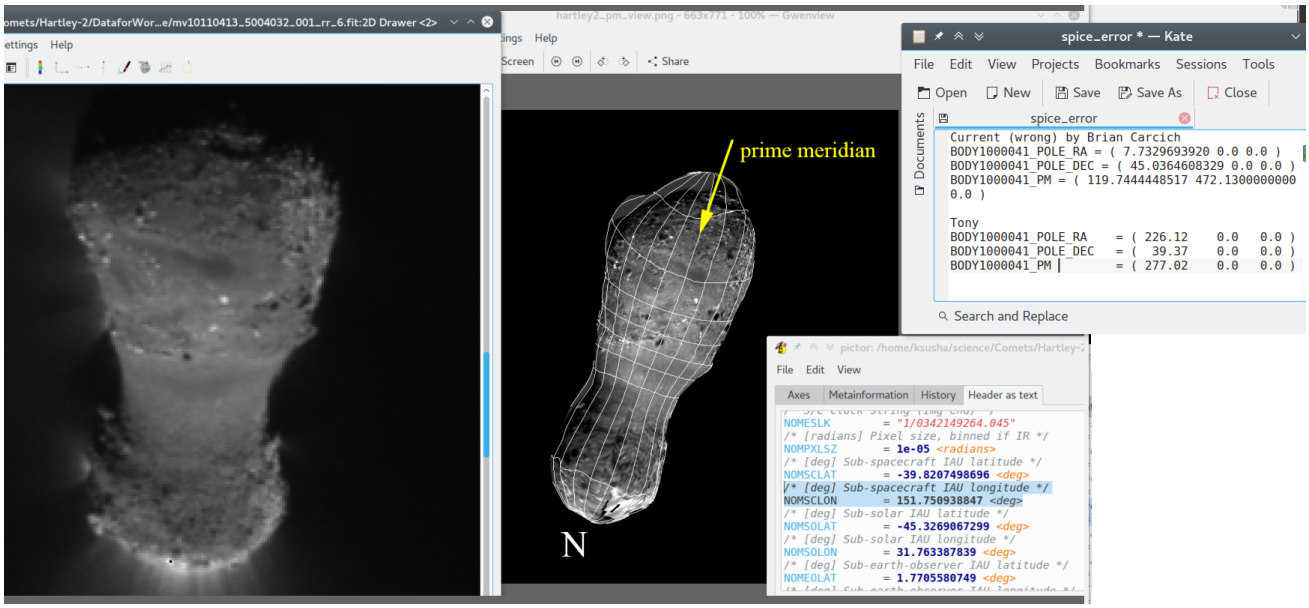

Figure 6.11.: Errors in data headers.

After changing the orientation constants, the above mentioned test was performed again, and yielded much better results, but still not enough good, and some periodical dependence is still present (please, see image fig. 6.10c and fig. 6.10b with 3 dependencies for 3 probable coordinates of bright spot in shape model; it is seen that the first one gives the smallest difference, up to 7 pixels).

It is probable that the reason for this uncorrect behavior is incorrect camera coordinates, which are returned by SPICE. We did not get further comments from Dr. Farnham on this matter, so, we went back to our previous approach, but with modification: we utilize information from the shape model for the initial values.

This method showed that the available to the general public SPICE kernels for the mission do not agree with the nucleus shape model. Therefore we took another approach, combining the two methods.

6.4.2.4. Fitting adjusting reference objects locations

In this modification of the very general method (section 6.4.2.2) we use data from the shape model as initial values for the reference objects positions. It is hard to correlate details in images, most of that are shadows and light patches to the the relief features in the model.

We assumed that the spacecraft trajectory is a straight line (initial trajectory was obtained from SPICE) but then it can be adjusted. As such, we were changing the following variables.

- Common for all images:

  Spacecraft trajectory : two angles defining direction and a cartesian 3D vector defining a base point.

  Reference objects coordinates as 3D cartesian vector for each object.

- Per image:

  Camera orientation is defined by three angles.

  Camera position is defined by shift along the trajectory from the base point.

The fitting was done minimising the same quantity (eq. (6.1)) as in section 6.4.2.2 with the help of Nelder-Mead method. In most of the cases displacements for the reference objects is within

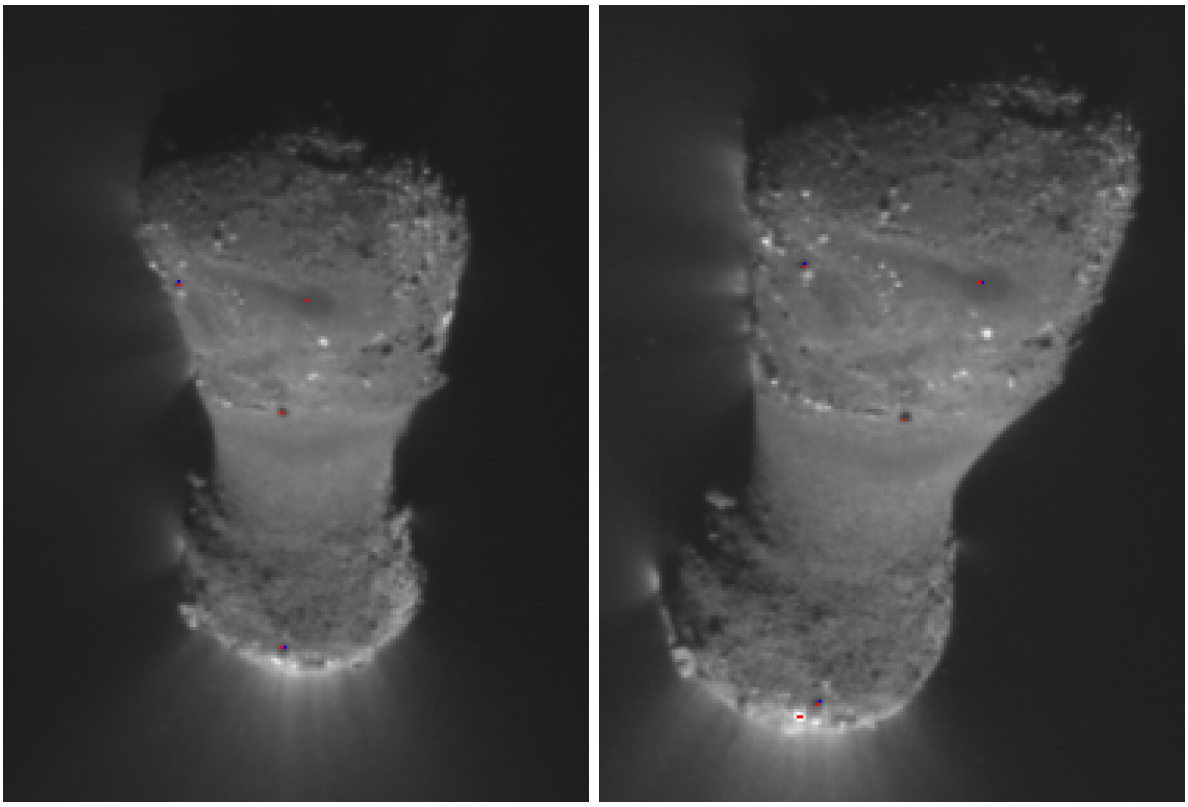

(a) Image #5004031. **(b)** Image #5004042.

Figure 6.12.: Example of the reference objects positions fitting. Blue points mark measured in images locations, red ones show locations obtained projecting the 3D positions onto the image plane. A red point was put after the blue ones and may hide the latter completely if their pixel positions are the same.

1 – 2 px (see example in fig. 6.12), but for image #5004046 and later ones, the displacement increases quickly reaching ~ 10 px due to unknown reason.

6.5. Searching the particles using DIXI data

We tried to get the better pointing by set of the closest images obtained by MRI, and did not reach the needed accuracy for performing the independent grains search at DIXI/MRI images to compare our results with results retrieved in [29].

Regardless of above listed problems, developed algorithm of boulders detection in CCD cometary images was successfully tested using the manually selected set of points from MRI data (which were clearly seen as same particles visually at several images) (seefig. 6.18).

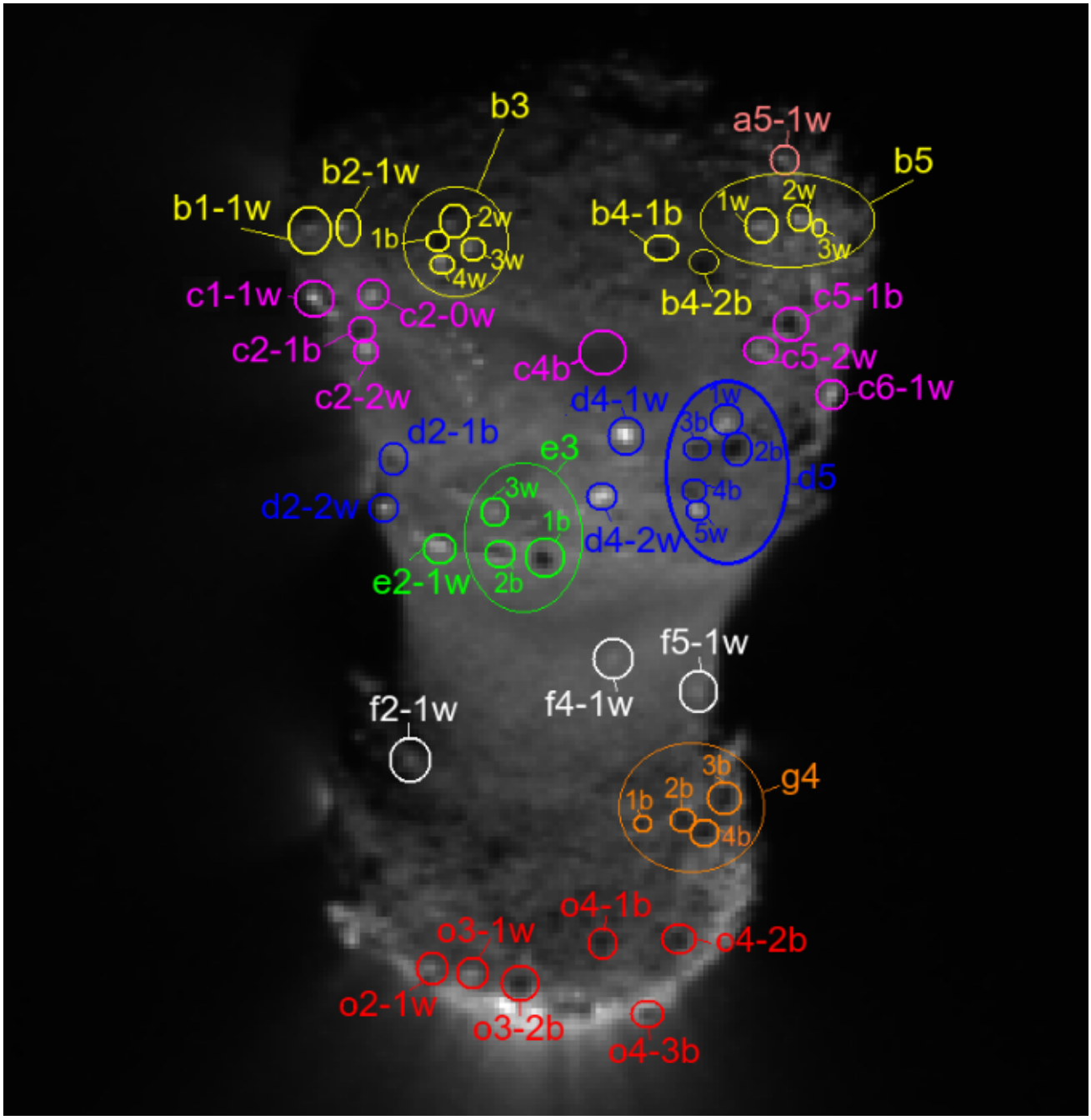

Figure 6.13.: Basic points. White points were marked by “w”, black by “b”.

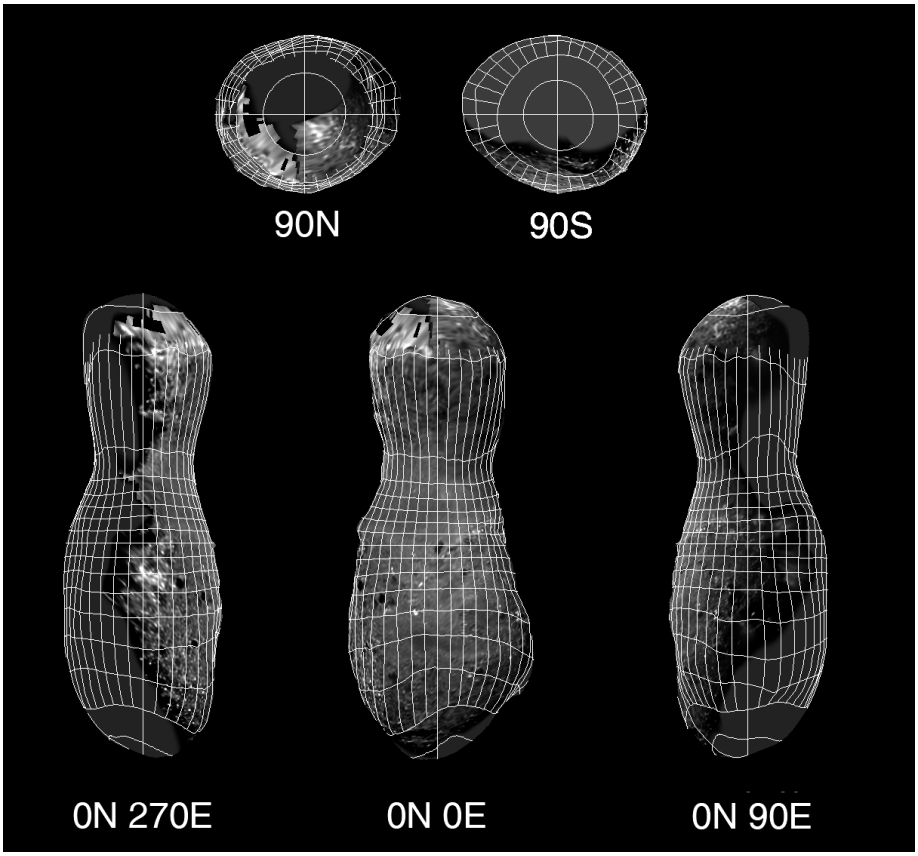

Figure 6.14.: Images showing views of the nucleus from the primary axes, incudes surface features and coordinate grid [40].

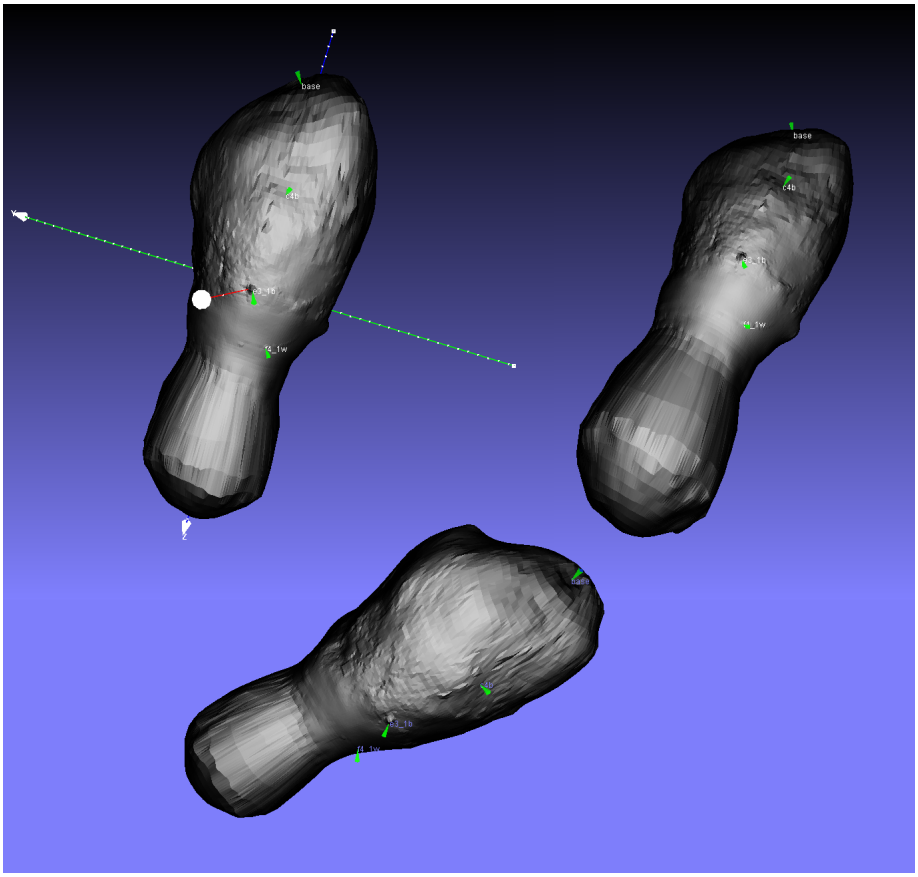

Figure 6.15.: Model images with marked base points fro different points of view.

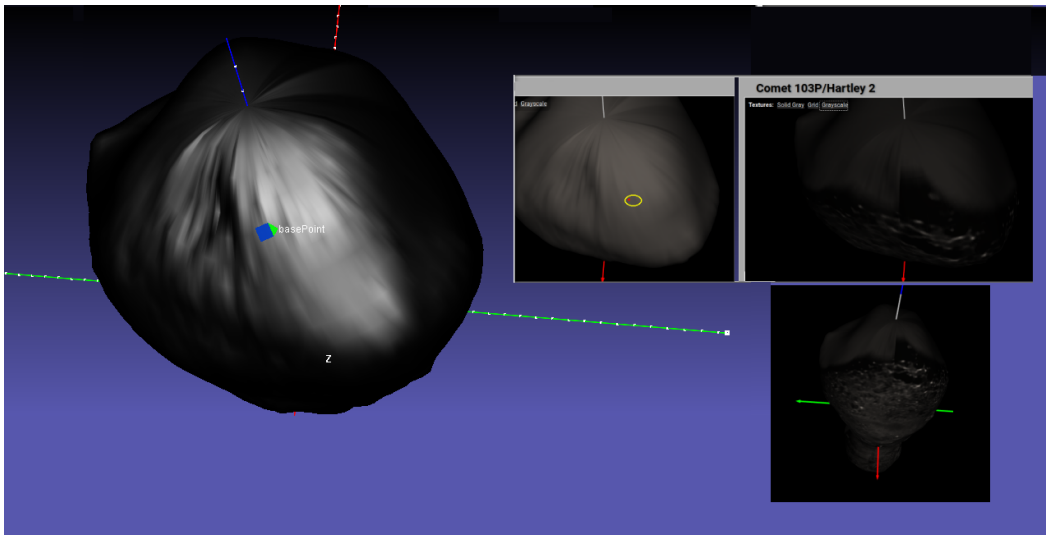

Figure 6.16.: View from pole on a base point.

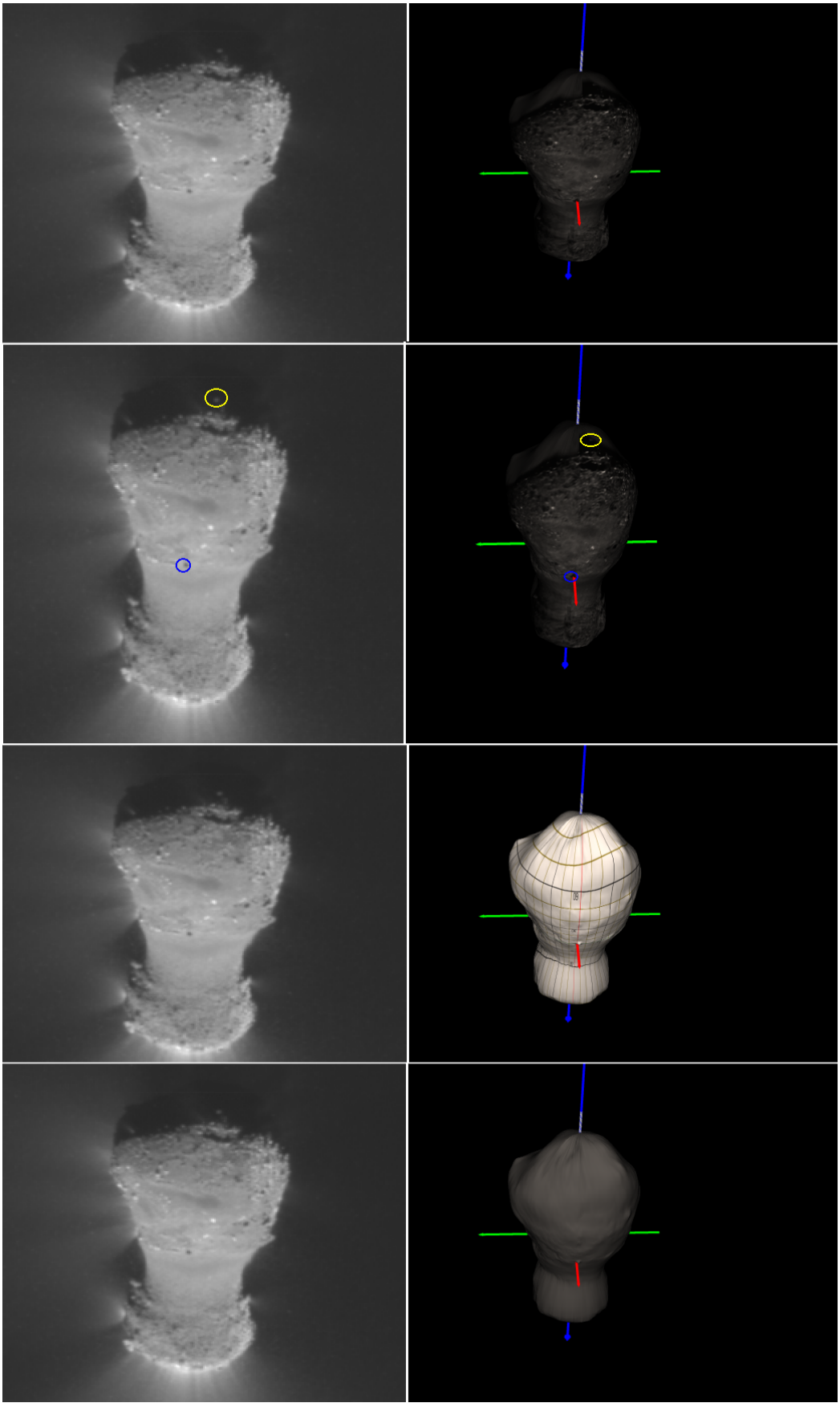

Figure 6.17.: Illustration of two base points positions at comet MRI image and at model image. The null point which is seen as shadow of hill, and the pole bright point which is clearly seen at all images. Axis Y almost going through the black base point, and central meridian are defined to go through this point.

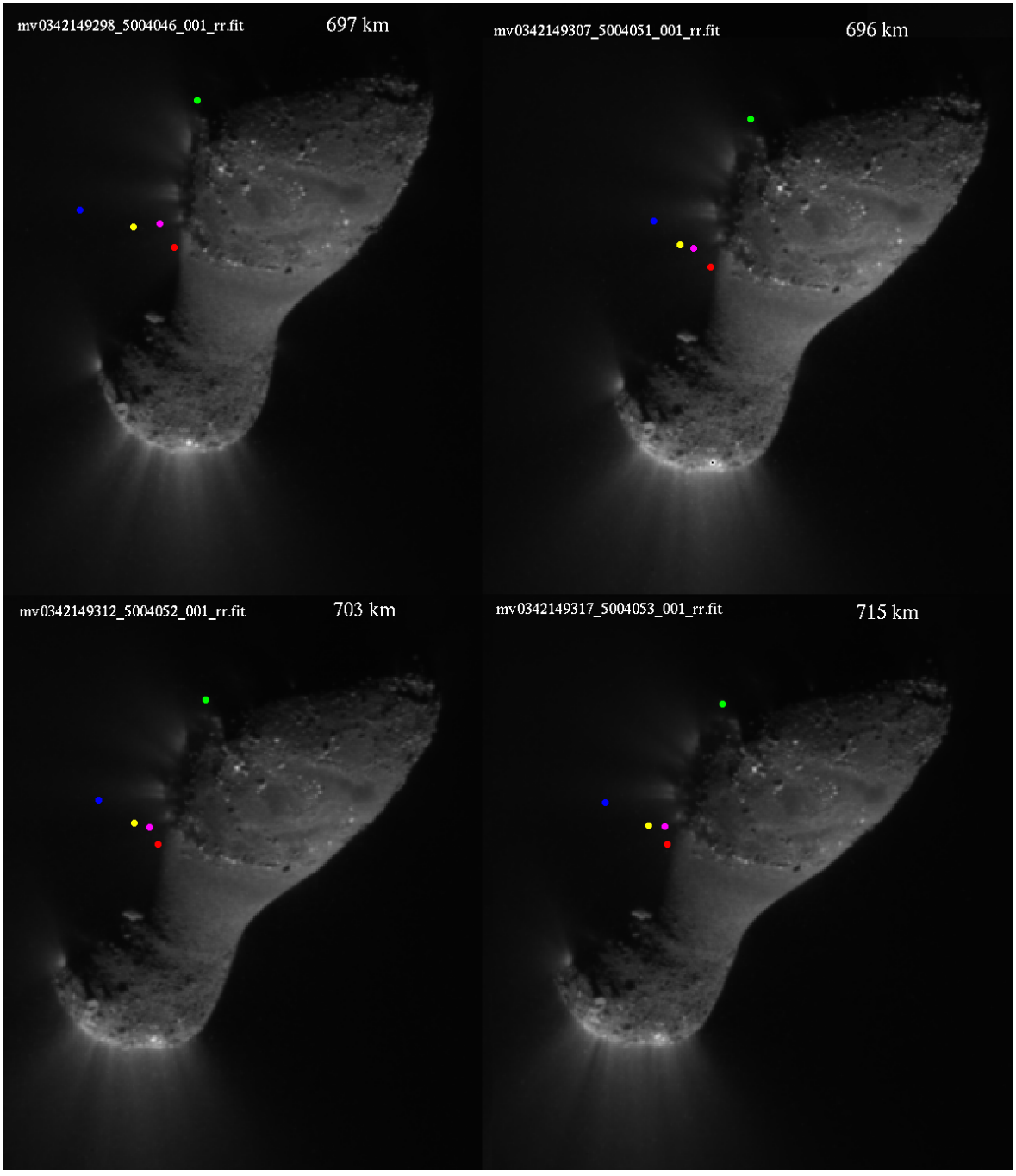

Figure 6.18.: Examples of MRI clear filter encounter images of Hartley 2 demonstrate several particle positions (marked by colour) and one control point (jet, marked by green colour) that were used for testing the particle search software.

6.6. Summary 2: Testing the software using DIXI/MRI data

1. Working set of 24 images was used in current work (see details in chapter F): Level 3 RADREV calibrated, "clear filter", image numbers starting from mv10110413 _5004029 (distance from camera to nucleus $D = 963.144$ km), with the closest image mv10110413 _6000002 ($D = 694.051$ km), and the last one mv10110414 _5004064 ($D = 1\,004.451$ km). Optimal parameter values for suspicious pixels selection results in selection of about 2 000 suspicious pixels per image.

2. The software for retrieving the ephemerids from SPICE was developed and implemented. The retrieved accuracy of pointing was found not enough for particle search: it is good to only ~ 10 pixels instead of required 1 pixel.

3. Several approaches for retrieving a better positioning were proposed, and corresponding software has been developed. The common part for them is: for a set of objects on the surface of nucleus find camera position and orientation to fit projected onto image plane object locations to the measured in images ones.

   a) In the first one, the 3D position of a reference object was a free parameter. This is approach needs only images and *a priori* information about spacecraft trajectory shape. The approach failed to achieve a good fitting most likely due to presence of local minimus in the minimising function.

   b) The second one takes coordinates of the reference object directly from the shape mode. Unfortunately, we had only two such points measured with high accuracy, thus leaving us dependent on the spacecraft coordinates, taken from SPICE. The coordinates appeared to be poorly known.

   c) The third approach combines the first two, taking more reference objects with their coordinates from the shape model. The coordinates are used as initial values only. This approach gave the most accurate results (but not accurate enough through).

   All methods did not achieve required accuracy. The first method did not give the stable results, and accuracy for different images and base points search was in range of 1-5 pixels. The second method was ruined by errors in the SPICE kernels and their contradictions with the shape model. The third method gave good results (less than 1 px accuracy) for images before the closest approach, but quickly degraded after, falling to ~ 10 px accuracy.

   The obtained pointing accuracy does not allow to detect particles near the comet in all images and to determine their velocities.

4. Regardless of above listed problems, developed algorithm of boulders detection in CCD cometary images was successfully tested using the selected set of points from MRI data (which were clearly seen as same particles visually at several images).

5. A potential presence of particles in set of closest MRI images has been analyzed, but because of bad pointing accuracy, the algorithm produced many false-positive results.

Problems:

- It was found that SPICE do not provide required accuracy of pointing for our purposes.
- It was found that official released data archive contains errors in a headers of images (some of them are the same in SPICE kernels).

Possible update of the research:

Developed software can be applied to the analysis of data from another experiments, including Rosetta mission. The only work needs to be done is to transform image coordinates into boresight vectors in the nucleus frame, and it is desirable to have a precise pointing ($\sim$ 1 pixel). Therefore the software can be reused to analyze the data obtained for the other comets.

Conference attendance:

This work was presented at European Planetary Science Congress 2015 (27 September – 02 October 2015, Nantes, France) [28].

7. Summary of the project: Searching for large grains in CCD images of inner comas of comets

Motivation

Recent results suggest that the mechanism of cometary activity and the near-nucleus coma may substantially differ from what was thought before. Much of cometary activity may be initiated by a break-up of large boulders from the nucleus, but origin of boulders in coma is still an open question. Developing the algorithm of boulders detection in CCD cometary images and the software that could be applied for different comets could be useful to get better understanding of this problem.

Algorithm for searching the grains. Applying the sofware to GIOTTO/HMC data (comet 1P/ Halley)

1. The full HMC data set was stored on CD-ROMs and magnetic tapes in VMS format. The CD-ROMs have been read and the data from them stored. Not all of HMC backup tapes survied and thus not all data from them have been recovered. All available HMC data obtained during the Giotto mission stored in different places were collected and prepared to place them into a single data archive. Additionally, image headers were converted into the PDS labels.

2. Checks for reliability of the radiometric calibration of HMC images in the range of very weak signals were done. Problematic images were identified.

3. The preliminary testing of the Richardson-Lucy method in application to the HMC data was done on the example of the Earth images.

4. Estimations of particle detectability by the HMC camera was done. Dusty particles with radii of about $1-1.5\,\mathrm{m}$ and larger can be detected at the closest approach (in case of icy particles, the size decreases to centimetres). Obtained values are in accordance with the estimations made for comet 103P/Hartley 2. It was found that particles will look as unmoving objects in subsequent images, which allows for simple SNR increase.

5. According to the estimations of particles detectability, the set of images with numbers $3\,436-3\,493$ (distances from camera to nucleus are in range of $20\,000-4\,000\,\mathrm{km}$) was selected for searching the evidence of large particles ("flight" level of processing, MDM, detector C, clear filter).

6. Two algorithms were proposed for searching the particles in HMC images, and corresponding software has been developed.

    a) The first one, "Image differencing method" (IDM) is more simple, and works with image differencing. Software for superposing images was developed, and it was found that the difference between the images in selected sequence does not decreases significantly after reaching alignment accuracy of $0.25\,\mathrm{px}$. This method was found not

perspective because it is not accurate enough, and does not allow to make tests of plausibility of the results of searching the particles.

b) The second one, "Automatic method of the large particle detection" (AM) is more sophisticated and needs more developing, but it is much more accurate than IDM method, and has benefits that image differencing method does not have. Thus, it was chosen for further developing.

7. Software for AM algorithm for particle detection (section 4.3) was implemented.

   a) All software blocks have been successfully tested using known information from HMC images, and artificial data sets (*e.g.* for detection the trajectory of a moving particle).

   b) An algorithm and its optimal parameter values for suspicious pixels selection from the unprocessed HMC images were suggested: deviation of more than 4σ from the surrounding region with size 7×7 pixels in the images, processed by the diagonal Laplace filter. This results in selection of about 60 suspicious pixels per image, that are distributed not only in the comet jet areas.

8. A potential presence of particles in HMC images has been analysed.

   Suspicious pixels have been taken from the unprocessed HMC images. A comprehensive analysis was performed to test whether these pixels can be images of particles seen as stable objects or moving along straight lines with speeds between 0 and $500\,\mathrm{m}\cdot\mathrm{s}^{-1}$ with respect to the comet nucleus. For that retrievals of lines of sight for the suspicious pixels and consequent search for the intersections between them in different images were done. The test yielded no detected particles, *i.e.* HMC did not detect particles with radius larger than 1.5 m (in case of dark dusty particles).

Testing the software using DIXI/MRI data (comet 103P/Hartley 2)

1. Working set of 24 images was used in current work (see details in chapter F): Level 3 RADREV calibrated, "clear filter", image numbers starting from mv10110413 _5004029 (distance from camera to nucleus $D = 963.144\,\mathrm{km}$), with the closest image mv10110413 _6000002 ($D = 694.051\,\mathrm{km}$), and the last one mv10110414 _5004064 ($D = 1\,004.451\,\mathrm{km}$). Optimal parameter values for suspicious pixels selection results in selection of about 2 000 suspicious pixels per image.

2. The software for retrieving the ephemerids from SPICE was developed and implemented. The retrieved accuracy of pointing was found not enough for particle search: it is good to only ~ 10 pixels instead of required 1 pixel.

3. Several approaches for retrieving a better positioning were proposed, and corresponding software has been developed. The common part for them is: for a set of objects on the surface of nucleus find camera position and orientation to fit projected onto image plane object locations to the measured in images ones.

   a) In the first one, the 3D position of a reference object was a free parameter. This is approach needs only images and *a priori* information about spacecraft trajectory shape. The approach failed to achieve a good fitting most likely due to presence of local minimus in the minimising function.

   b) The second one takes coordinates of the reference object directly from the shape mode. Unfortunately, we had only two such points measured with high accuracy, thus leaving us dependent on the spacecraft coordinates, taken from SPICE. The coordinates appeared to be poorly known.

c) The third approach combines the first two, taking more reference objects with their coordinates from the shape model. The coordinates are used as initial values only. This approach gave the most accurate results (but not accurate enough through).

All methods did not achieve required accuracy. The first method did not give the stable results, and accuracy for different images and base points search was in range of 1-5 pixels. The second method was ruined by errors in the SPICE kernels and their contradictions with the shape model. The third method gave good results (less than 1 px accuracy) for images before the closest approach, but quickly degraded after, falling to ~ 10 px accuracy.

The obtained pointing accuracy does not allow to detect particles near the comet in all images and to determine their velocities.

4. Regardless of above listed problems, developed algorithm of boulders detection in CCD cometary images was successfully tested using the selected set of points from MRI data (which were clearly seen as same particles visually at several images).

5. A potential presence of particles in set of closest MRI images has been analyzed, but because of bad pointing accuracy, the algorithm produced many false-positive results.

Problems and possible solutions:

- Not all GIOTTO/HMC data that were expected to be stored are available due to technical reasons (data in original flight format, Altair images, PSF obtained using the Altair images are examples of the data that seem to be lost). But this was not critical for the current project. The PSF obtained using the Altair images could be replaced from the PSF obtained by the other star observations.

- It was found that SPICE did not provide needed accuracy of pointing for DIXI/MRI data: it is good to only ~ 10 pixels instead of 1 pixel of the location of the nucleus in the image.

- Wrong information in MRI images headers were found (some are the same generated by SPICE), as well as in the description file, that was confirmed also by Dr. Farnham who is one of the scientist responsible for the DIXI PDS archive. It is hard to predict how many errors may contain released data.

- We tried to get the better pointing by set of the closest images obtained by MRI, and did not reach the needed accuracy for performing the independent grains search at DIXI/MRI images to compare our results with results retrieved in [29]. It is possible, that the correction of cover information stored at data could lead to better pointing results, and thus to performing such research.

Possible update of the research:

Developed software can be applied to the analysis of data from another experiments, including Rosetta mission. The only work needs to be done is to transform image coordinates into boresight vectors in the nucleus frame, and it is desirable to have a precise pointing ($\sim$1 pixel). Therefore the software can be reused to analyze the data obtained for the other comets.

Conference attendance:

This work was presented at:

- European Planetary Science Congress 2015 (27 September–02 October 2015, Nantes, France) [28].

- 615. WE-Heraeus-Seminar on "How primitive are comets" (24–29 April 2016, Bad Honnef, Germany) [43].

Honors:

Best poster prize for "Searching for large particles in images of inner comas of comets" [43], WE-Heraeus-Seminar on "How primitive are comets", Bad Honnef, Germany (2016).

Publications

[1] M. F. A'Hearn, M. J. Belton, W. A. Delamere, L. M. Feaga, D. Hampton, J. Kissel, K. P. Klaasen, L. A. McFadden, K. J. Meech, H. J. Melosh, et al. "EPOXI at comet Hartley 2". In: *Science* 332.6036 (2011), pp. 1396–1400.

[2] B. Gundlach, S. Kilias, E. Beitz, and J. Blum. "Micrometer-sized ice particles for planetary-science experiments–I. Preparation, critical rolling friction force, and specific surface energy". In: *Icarus* 214.2 (2011), pp. 717–723.

[3] B. Gundlach, Y. V. Skorov, and J. Blum. "Outgassing of icy bodies in the Solar System–I. The sublimation of hexagonal water ice through dust layers". In: *Icarus* 213.2 (2011), pp. 710–719.

[4] Y. V. Skorov, R. Van Lieshout, J. Blum, and H. U. Keller. "Activity of comets: Gas transport in the near-surface porous layers of a cometary nucleus". In: *Icarus* 212.2 (2011), pp. 867–876.

[5] P. Lämmerzahl, J. Gebhard, E. Grün, and G. Klees. "Gas release from ice/dust mixtures: results from eleven KOSI experiments". In: *Planetary and Space Science* 43.3 (1995), pp. 363–373.

[6] *GIOTTO HALLEY MULTICOLOR CAMERA IMAGES V1.0*. ESA, Planetary Science Archive. URL: http://www.sciops.esa.int/index.php?project=PSA&page=giotto.

[7] *GIOTTO HALLEY MULTICOLOR CAMERA IMAGES V1.0*. NASA, The Planetary Data System. URL: http://pdssbn.astro.umd.edu/holdings/gio-c-hmc-3-rdr-halley-v1.0/dataset.html.

[8] H. U. Keller, W. Curdt, J.-R. Kramm, and N. Thomas. *Images of the Nucleus of Comet Halley obtained by the Halley Multicolour Camera (HMC) on board the Giotto spacecraft*. Ed. by R. Reinhard, N. Longdon, and B. Battrick. Vol. 1. Atlas of Images the Nucleus of Comet Halley. ESTEC, Nordwijk, The Netherlands: ESA Publications Division, 1994. ISBN: 92-9092-080-7.

[9] J. R. Kramm, W. Möhring, and H. U. Keller. "Image restoration using the point spread function of the Halley Multicolour Camera". In: *Geophysical research letters* 14.7 (1987), pp. 677–680.

[10] K. Wilhelm. *HMC In-flight calibrations: Some Geometric and Radiometric Aspects*. Tech. rep. MPAE-W-55-86-06. Rev. 1. MPAE, Feb. 1986.

[11] N. Thomas and H. U. Keller. "Photometric calibration of the Halley multicolour camera". In: *Applied optics* 29.10 (1990), pp. 1503–1519.

[12] B. Hanisch, ed. *Newsletter of STScI's Image restoration project*. AURA. Vol. 1. Maryland, 1993, p. 83.

[13] W. H. Richardson. "Bayesian-based iterative method of image restoration". In: *JOSA* 62.1 (1972), pp. 55–59.

[14] L. B. Lucy. "An iterative technique for the rectification of observed distributions". In: *The astronomical journal* 79 (1974), p. 745.

[15] L. A. Shepp and Y. Vardi. "Maximum likelihood reconstruction for emission tomography". In: *Medical Imaging, IEEE Transactions on* 1.2 (1982), pp. 113–122.

[16] H. U. Keller et al. *Halley Multicolour Camera design and performance requirements specification*. 6th ed. MPAE. May 1984.

[17] M. S. Kelley, D. J. Lindler, D. Bodewits, M. F. A'Hearn, C. M. Lisse, L. Kolokolova, J. Kissel, and B. Hermalyn. "A distribution of large particles in the coma of Comet 103P/Hartley 2". In: *Icarus* 222.2 (2013), pp. 634–652.

[18] W. Curdt and H. Keller. "Collisions with cometary dust recorded by the Giotto HMC camera". In: *ESA Journal* 12 (1988), pp. 189–208.

[19] W. Curdt and H. U. Keller. "Large dust particles along the Giotto trajectory". In: *Icarus* 86.1 (1990), pp. 305–313.

[20] J. A. Nelder and R. Mead. "A simplex method for function minimization". In: *The computer journal* 7.4 (1965), pp. 308–313.

[21] *Blink comparator*. URL: http://en.wikipedia.org/wiki/Blink_comparator.

[22] *SPICE*. URL: http://www.cosmos.esa.int/web/spice.

[23] *An Observation Geometry System for Planetary Science Missions*. URL: http://naif.jpl.nasa.gov/naif/.

[24] *Giotto SPK files*. URL: http://naif.jpl.nasa.gov/pub/naif/GIOTTO/kernels/spk/.

[25] W. Curdt. "HMC fine targeting at the Halley encounter". In: *MPAE Report* MPAE-W-55-87-12 (1987).

[26] A. Craubner, G. Schwarz, E. Mikusch, K. Schmidt, W. Curdt, W. Degenhardt, H. Keller, and K. Wilhelm. "High Precision Geometrical Rectification, Registration and Composition of Cometary Images Taken by the Halley Multicolour Camera". In: *Proc. 13th Annual Conference of The Remote Sensing Society, Advances in Image Processing*. 1987, pp. 23–35.

[27] A. Craubner, E. Mikusch, K. Schmidt, and G. Schwarz. "Image processing document Halley Multicolor Camera (Giotto mission)". In: *DFVR Report* DFVR-FB 88-20 (1988), p. 419.

[28] O. Shalygina, H. Keller, and J. Blum. "Re-analysis of the Giotto mission data obtained by the Halley Multicolour Camera (HMC) with aim of large particles detection in the inner coma of comet 1P/Halley". In: *EPSC*. (Nantes, France). Vol. 10. EPSC2015-592. 2015. URL: http://meetingorganizer.copernicus.org/EPSC2015/EPSC2015-592.pdf.

[29] B. Hermalyn, T. L. Farnham, S. M. Collins, M. S. Kelley, M. F. A'Hearn, D. Bodewits, B. Carcich, D. J. Lindler, C. Lisse, K. Meech, et al. "The detection, localization, and dynamics of large icy particles surrounding Comet 103P/Hartley 2". In: *Icarus* 222.2 (2013), pp. 625–633.

[30] M. V. Sykes and R. G. Walker. "Cometary dust trails: I. Survey". In: *Icarus* 95.2 (1992), pp. 180–210.

[31] M. Ishiguro, J. Watanabe, F. Usui, T. Tanigawa, D. Kinoshita, J. Suzuki, R. Nakamura, M. Ueno, and T. Mukai. "First detection of an optical dust trail along the orbit of 22P/Kopff". In: *The Astrophysical Journal Letters* 572.1 (2002), p. L117.

[32] W. T. Reach, M. S. Kelley, and M. V. Sykes. "A survey of debris trails from short-period comets". In: *Icarus* 191.1 (2007), pp. 298–322.

[33] J. K. Harmon, M. C. Nolan, E. S. Howell, J. D. Giorgini, and P. A. Taylor. "Radar observations of comet 103P/Hartley 2". In: *The Astrophysical Journal Letters* 734.1 (2011), p. L2.

[34] D. L. Hampton, J. W. Baer, M. A. Huisjen, C. C. Varner, A. Delamere, D. D. Wellnitz, M. F. A'Hearn, and K. P. Klaasen. "An overview of the instrument suite for the Deep Impact mission". In: *Space Science Reviews* 117.1-2 (2005), pp. 43–93.

[35] K. P. Klaasen, M. F. A'Hearn, M. Baca, A. Delamere, M. Desnoyer, T. Farnham, O. Groussin, D. Hampton, S. Ipatov, J. Li, et al. "Invited article: Deep Impact instrument calibration". In: *Review of Scientific Instruments* 79.9 (2008), p. 091301.

[36] M. S. Kelley, D. J. Lindler, D. Bodewits, M. F. A'Hearn, C. M. Lisse, L. Kolokolova, J. Kissel, and B. Hermalyn. "Erratum to "A distribution of large particles in the coma of Comet 103P/Hartley 2" [Icarus 222 (2013) 634–652] ". In: *Icarus* 262 (2015), pp. 187–189. ISSN: 0019-1035. DOI: 10.1016/j.icarus.2015.09.004. URL: //www.sciencedirect.com/science/article/pii/S0019103515004005.

[37] E. A. Team. *MRI-data*. 2011. URL: http://pds-smallbodies.astro.umd.edu/holdings/dif-c-mri-3_4-epoxi-hartley2-v1.0/.

[38] E. A. Team, ed. *EPOXI: Raw and Calibrated Science Data Products for Hi-Res IR Spectrometer (HRII) Hi-Res Visible CCD (HRIV) Medium-Res Visible CCD (MRI)*. 2011. URL: http://pds-smallbodies.astro.umd.edu/holdings/dif-c-mri-3_4-epoxi-hartley2-v1.0/document/epoxi_sis.pdf.

[39] T. Farnham. Personal communication. Department of Astronomy University of Maryland, USA, 2016.

[40] T. Farnham and P. Thomas. *PLATE SHAPE MODEL OF COMET 103P/HARTLEY 2 V1.0, DIF-C-HRIV/MRI-5-HARTLEY2-SHAPE-V1.0*. Ed. by N. P. D. System. 2013. URL: http://pdssbn.astro.umd.edu/holdings/dif-c-hriv_mri-5-hartley2-shape-v1.0/dataset.html.

[41] B. Carcich and B. Semenov. *SPICE*. 2011. URL: https://naif.jpl.nasa.gov/pub/naif/pds/data/dif-c_e_x-spice-6-v1.0/epxsp_1000/data/pck/di_hartley_2_v01.tpc.

[42] P. Thomas, M. F. A'Hearn, J. Veverka, M. J. Belton, J. Kissel, K. P. Klaasen, L. A. McFadden, H. J. Melosh, P. H. Schultz, S. Besse, et al. "Shape, density, and geology of the nucleus of Comet 103P/Hartley 2". In: *Icarus* 222.2 (2013), pp. 550–558.

[43] O. S. Shalygina, H. U. Keller, and J. Blum. "Searching for large particles in images of inner comas of comets". In: *Proc. WE-Heraeus-Seminar on "How primitive are comets", Bad Honnef, Germany*. 2016.

[44] N. Thomas and H. U. Keller. "Comet P/Halley's dust production rate at Giotto encounter derived from Halley Multicolour Camera observations". In: *Astronomy and astrophysics* 249.1 (1991), pp. 258–268.

[45] N. Thomas and H. U. Keller. "Interpretation of the inner coma observations of comet P/Halley by the Halley Multicolor Camera". In: *Annales Geophysicae* 8 (Feb. 1990), pp. 147–165.

Appendices

A. Examples of HMC images

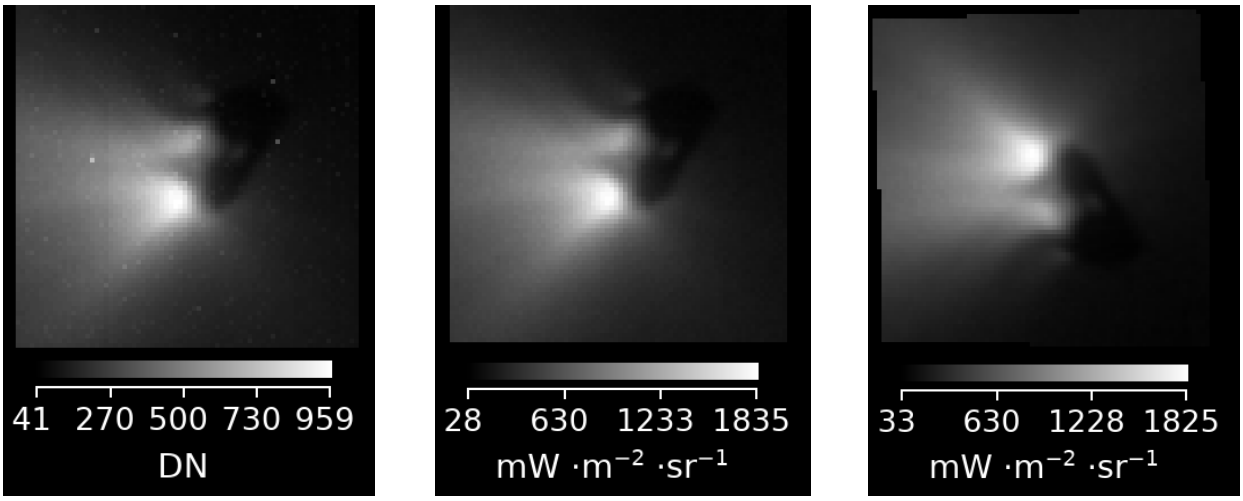

(a) FNC03437, "flight" level. **(b)** FNC03437, "radio" level. **(c)** FNC03437, "geo" level.

(d) FCC03128, "flight" level. **(e)** FCC03128, "radio" level. **(f)** FCC03128, "geo" level.

Figure A.1.: Examples of images obtained in the Clear filter. FNC03437: size is 74 x 74 pixels, distance to nucleus is 19925 km (figs. A.1a to A.1c), and FCC03128: size is 196 x 196 pixels, distance to nucleus is 104386 km (figs. A.1d to A.1f). Demonstration of the three levels of data processing. Geometrical rectified data (figs. A.1c and A.1f) are oriented in a specific coordinate system: a horizontal line on the images is parallel to a plane defined by the relative velocity vector of the Giotto spacecraft and the centre of the cometary nucleus.

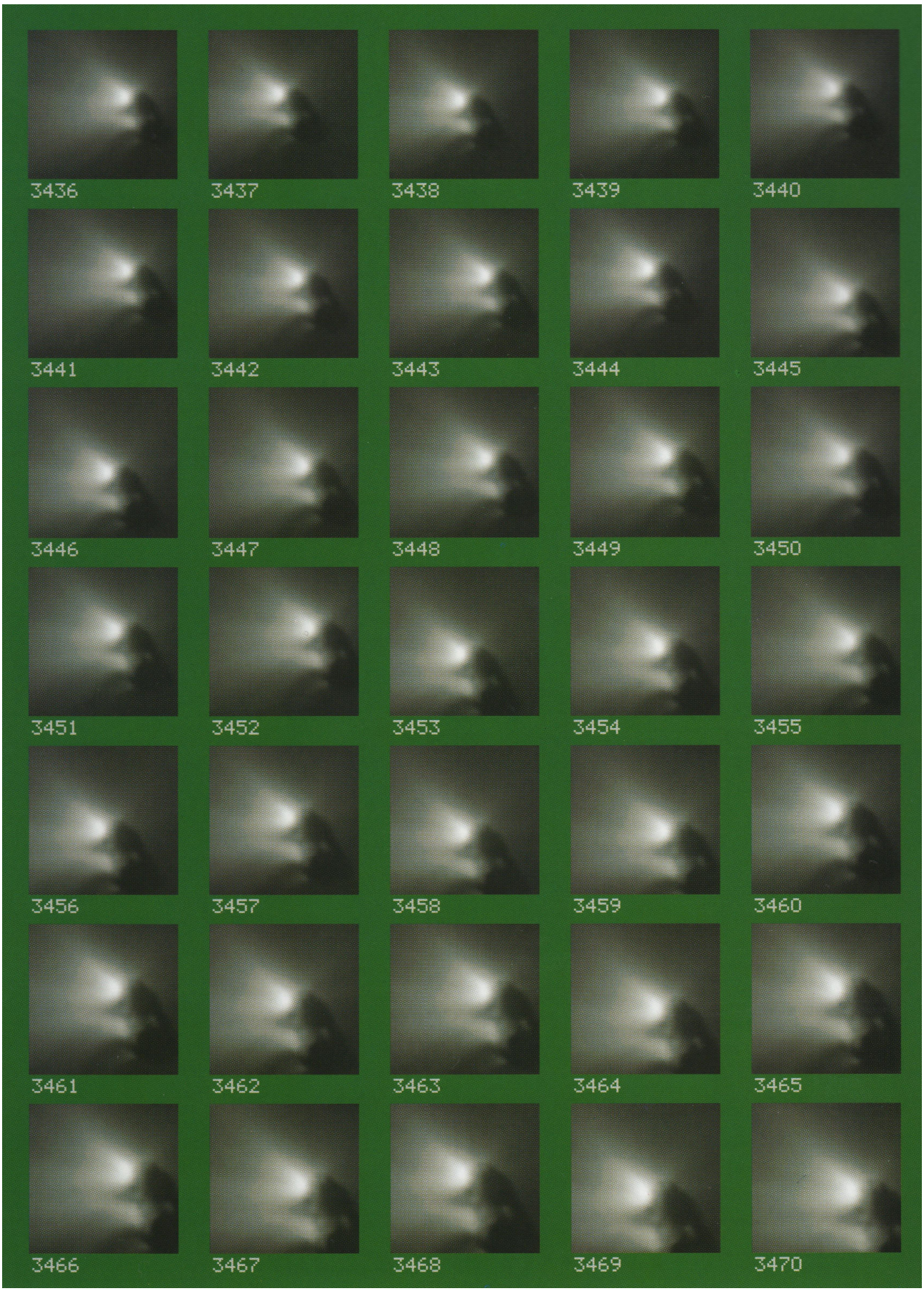

Figure A.2.: Sequence of HMC images obtained in MDM, clear filter, detector C, calibrated, cleaned (from [8]). Numbers of images: 3436–3470.

Figure A.3.: Sequence of HMC images obtained in MDM, clear filter, detector C, calibrated, cleaned (from [8]). Numbers of images: 3471–3503.

B. Results of the background data approximation by the Poisson distribution

Table B.1.: Fit results. Images with bad fit for $I \leqq 2$ and $4\,\mathrm{mW \cdot m^{-2} \cdot sr^{-1}}$ are marked by a *. For images with for $I \leqq 6\,\mathrm{mW \cdot m^{-2} \cdot sr^{-1}}$ the bad fits in the ranges of small amount of pixels are marked by a star *, and the image with small number of points is marked by a circle $^\circ$. Last column shows the filter name: "c" is "clear" ($\lambda_{eff} = 652.9\,\mathrm{nm}$), "b" is "blue" ($\lambda_{eff} = 440.0\,\mathrm{nm}$), "r" is "red" ($\lambda_{eff} = 813.0\,\mathrm{nm}$), and "o" is "orange" ($\lambda_{eff} = 645.4\,\mathrm{nm}$).

Filename	$\leqq 2\,\mathrm{mW \cdot m^{-2} \cdot sr^{-1}}$			$\leqq 4\,\mathrm{mW \cdot m^{-2} \cdot sr^{-1}}$			$\leqq 6\,\mathrm{mW \cdot m^{-2} \cdot sr^{-1}}$			Filter
	Δx	λ	$\lambda + \Delta x$	Δx	λ	$\lambda + \Delta x$	Δx	λ	$\lambda + \Delta x$	
FCC00682	-8.01	18.70	10.69	-14.61	17.26	2.65	-13.34	17.30	3.96	c
FCC00686	-8.26	18.55	10.28	-15.27	17.04	1.77	-14.63	16.98	2.35	c
FCC00688	-6.39	10.02	3.64	-9.95	13.10	3.15	-3.23	6.59	3.36	c
FCC00692	-8.19	18.56	10.37	-15.37	17.06	1.69	-14.43	17.02	2.58	c
FCC00694	-7.70	18.79	11.08	-9.80	13.35	3.55	-2.55	6.43	3.88	c
FCC00698	-7.85	18.73	10.88	-7.12	11.91	4.79	-4.01	8.70	4.69	c
FCC00700	-8.11	18.67	10.57	-2.51	6.44	3.93	-2.84	6.99	4.16	c
FCC00704	-8.39	11.13	2.75	-5.27	8.25	2.98	-5.58	8.53	2.94	c
FCC00720	-16.00	16.72	0.71	-12.97	13.72	0.75	-10.03	10.81	0.77	r
FCC00736	-15.97	16.52	0.55	-12.76	13.32	0.56	-11.11	11.67	0.57	o
FCC00752	-25.15	25.62	0.48	-18.59	19.14	0.55	-21.67	22.21	0.54	b
FCC00776	-10.96	13.46	2.50	-0.84	3.74	2.91	-5.09	8.07	2.98	c
FCC00792	-15.77	16.59	0.82	-12.99	13.82	0.83	-8.88	9.74	0.86	r
FCC00808	-13.79	14.42	0.63	-11.26	11.91	0.65	-11.09	11.75	0.66	o
FCC00824	-25.86	26.61	0.75	-21.00	21.77	0.77	-19.85	20.59	0.74	b
FCC00848	-5.94	8.91	2.98	-4.91	8.02	3.10	-5.31	8.38	3.07	c
FCC00864	-14.71	15.55	0.84	-12.30	13.28	0.98	-10.05	11.06	1.01	r
FCC00880	-15.68	16.38	0.70	-12.54	13.25	0.71	-12.99	13.70	0.72	o
FCC00896	-21.36	22.37	1.00	-21.97	22.88	0.91	-23.06	23.94	0.87	b
FCC00920	-5.59	8.53	2.95	-6.54	9.57	3.04	-4.13	7.30	3.17	c
FCC00936	-11.98	13.01	1.03	-10.69	11.70	1.01	-8.72	9.76	1.03	r
FCC00952	-12.31	13.06	0.75	-11.12	11.85	0.73	-9.41	10.15	0.74	o
FCC00968 *	-18.87	20.11	1.24	-22.04	23.06	1.02	-23.19	24.16	0.97	b
FCC00998	-7.30	10.27	2.98	-5.63	8.68	3.04	-3.70	6.89	3.19	c
FCC01014	-13.50	14.51	1.01	-9.94	10.99	1.05	-8.62	9.69	1.06	r
FCC01030	-13.33	14.08	0.75	-10.74	11.52	0.77	-9.97	10.76	0.78	o
FCC01046	-20.10	21.25	1.15	-21.54	22.59	1.05	-23.03	24.03	1.00	b
FCC01070	-14.00	16.68	2.68	-7.70	10.68	2.98	-3.17	6.42	3.25	c
FCC01086	-16.22	17.32	1.09	-12.01	13.12	1.11	-9.83	10.97	1.14	r
FCC01102	-13.81	14.64	0.83	-13.70	14.52	0.82	-12.89	13.72	0.83	o
FCC01118	-21.45	22.66	1.21	-21.60	22.71	1.10	-22.73	23.79	1.06	b
FCC01142	-7.16	10.22	3.06	-7.36	10.33	2.97	-2.85	6.15	3.30	c
FCC01158	-14.59	15.72	1.13	-11.32	12.46	1.13	-9.46	10.62	1.15	r

Continued on next page

Filename	$\leqq 2\,\mathrm{mW \cdot m^{-2} \cdot sr^{-1}}$			$\leqq 4\,\mathrm{mW \cdot m^{-2} \cdot sr^{-1}}$			$\leqq 6\,\mathrm{mW \cdot m^{-2} \cdot sr^{-1}}$			Filter
	Δx	λ	$\lambda + \Delta x$	Δx	λ	$\lambda + \Delta x$	Δx	λ	$\lambda + \Delta x$	
FCC01174	-13.76	14.58	0.82	-10.80	11.62	0.82	-10.40	11.24	0.83	o
FCC01190	-21.56	22.91	1.35	-22.13	23.30	1.17	-23.22	24.34	1.12	b
FCC01214	-9.12	11.90	2.78	-5.61	8.67	3.06	-2.85	6.16	3.31	c
FCC01230	-16.97	18.20	1.22	-9.01	10.26	1.26	-10.86	12.11	1.25	r
FCC01246	-14.28	15.28	1.00	-14.00	14.95	0.95	-13.28	14.25	0.96	o
FCC01262	-23.55	25.10	1.55	-18.93	20.32	1.39	-17.45	18.82	1.37	b
FCC01292 ⋆	-14.32	17.29	2.97	-9.76	12.78	3.01	-2.30	5.78	3.48	c
FCC01308	-14.79	16.07	1.28	-13.80	15.09	1.29	-8.65	9.98	1.34	r
FCC01324	-12.05	13.03	0.98	-10.99	11.96	0.96	-8.44	9.42	0.98	o
FCC01340	-22.58	24.11	1.53	-18.72	20.13	1.42	-17.78	19.16	1.38	b
FCC01364 ⋆	-9.00	12.17	3.17	-6.13	9.33	3.20	-2.46	6.01	3.55	c
FCC01380	-15.02	16.38	1.36	-1.76	3.38	1.62	-10.38	11.76	1.38	r
FCC01396	-9.89	0.28	-9.62	-9.87	0.28	-9.59	-11.40	12.46	1.05	o
FCC01412	-20.95	22.54	1.58	-21.02	22.49	1.47	-22.24	23.65	1.41	b
FCC01436*	-10.00	0.25	-9.75	-10.00	0.25	-9.75	-2.35	5.90	3.55	c
FCC01452*	-9.91	0.27	-9.63	-9.88	0.28	-9.60	-8.99	10.37	1.38	r
FCC01468	-12.95	13.96	1.02	-10.66	11.67	1.01	-8.63	9.66	1.03	o
FCC01484	-24.84	26.44	1.61	-18.96	20.43	1.48	-17.71	19.15	1.44	b
FCC01508*	-9.50	0.74	-8.76	-9.34	0.83	-8.51	-2.30	5.93	3.63	c
FCC01524	-13.06	14.47	1.42	-10.80	12.19	1.39	-7.65	9.09	1.44	r
FCC01540	-12.92	13.92	1.00	-10.06	11.09	1.03	-7.56	8.61	1.06	o
FCC01556	-22.24	23.86	1.62	-21.87	23.33	1.47	-22.69	24.12	1.43	b
FCC01586 ⋆	-8.85	11.74	2.89	-6.78	10.02	3.24	-1.63	5.30	3.67	c
FCC01602	-15.96	17.33	1.37	-10.96	12.36	1.40	-8.31	9.74	1.44	r
FCC01618	-14.86	15.92	1.06	-11.54	12.60	1.06	-9.41	10.49	1.08	o
FCC01634	-21.71	23.64	1.93	-22.64	24.19	1.55	-23.26	24.77	1.50	b
FCC01658 ⋆	-9.05	12.24	3.20	-8.13	11.23	3.10	-1.75	5.36	3.61	c
FCC01674	-13.82	15.29	1.47	-11.16	12.61	1.45	-8.88	10.36	1.48	r
FCC01690	-15.35	16.46	1.11	-12.08	13.17	1.09	-9.54	10.66	1.11	o
FCC01706	-24.46	26.30	1.84	-19.93	21.62	1.69	-18.86	20.47	1.62	b
FCC01730 ⋆	-8.08	11.40	3.32	-7.97	11.11	3.13	-1.90	5.51	3.61	c
FCC01746	-14.40	15.91	1.52	-11.45	12.92	1.47	-7.79	9.32	1.53	r
FCC01762*	-9.99	0.25	-9.74	-9.99	0.25	-9.74	-10.03	11.17	1.14	o
FCC01778	-19.73	21.71	1.98	-21.90	23.58	1.68	-22.92	24.54	1.61	b
FCC01802 ⋆	-10.34	13.69	3.36	-8.48	11.72	3.24	-2.30	5.91	3.61	c
FCC01818	-12.82	14.43	1.61	-11.85	13.38	1.54	-9.21	10.80	1.58	r
FCC01834*	-9.93	0.27	-9.65	-9.91	0.28	-9.63	-9.95	11.12	1.17	o
FCC01850	-20.39	22.38	1.99	-21.99	23.71	1.72	-23.31	24.94	1.64	b
FCC01880 ⋆	-5.98	10.90	4.91	-9.50	12.76	3.26	-2.30	5.96	3.66	c
FCC01896	-14.30	15.92	1.62	-11.16	12.75	1.59	-7.56	9.21	1.65	r
FCC01912	-15.20	16.43	1.24	-12.10	13.29	1.19	-9.66	10.88	1.21	o
FCC01928 ⋆	-23.08	25.20	2.13	-20.52	22.26	1.75	-18.82	20.52	1.70	b
FCC01952	-6.53	10.22	3.69	-7.52	10.81	3.29	-2.61	6.26	3.65	c
FCC01968	-12.60	14.37	1.76	-11.98	13.63	1.65	-9.49	11.18	1.70	r
FCC01984	-14.22	15.51	1.29	-12.71	13.94	1.23	-10.22	11.47	1.25	o
FCC02000	-24.14	26.27	2.14	-22.82	24.61	1.79	-23.88	25.57	1.69	b
FCC02024	-12.76	16.28	3.52	-9.95	13.38	3.42	-6.31	9.88	3.57	c
FCC02040	-13.79	15.50	1.71	-12.29	13.90	1.61	-6.81	8.55	1.73	r
FCC02056	-15.16	16.41	1.24	-11.18	12.43	1.25	-7.38	8.68	1.30	o

Continued on next page

Filename	$\leqq 2\,\mathrm{mW \cdot m^{-2} \cdot sr^{-1}}$			$\leqq 4\,\mathrm{mW \cdot m^{-2} \cdot sr^{-1}}$			$\leqq 6\,\mathrm{mW \cdot m^{-2} \cdot sr^{-1}}$			Filter
	Δx	λ	$\lambda + \Delta x$	Δx	λ	$\lambda + \Delta x$	Δx	λ	$\lambda + \Delta x$	
FCC02072	-27.01	29.14	2.13	-22.54	24.45	1.92	-24.06	25.85	1.79	b
FCC02096	-6.29	10.77	4.48	-10.11	13.65	3.55	-2.86	6.72	3.86	c
FCC02112	-1.74	3.42	1.69	-10.43	12.19	1.75	-6.07	7.92	1.85	r
FCC02128	-15.28	16.65	1.37	-12.03	13.37	1.34	-8.33	9.73	1.40	o
FCC02144	-25.86	28.04	2.18	-22.05	24.01	1.97	-22.80	24.70	1.90	b
FCC02174	-6.11	9.86	3.75	-5.45	9.27	3.82	-4.10	8.04	3.94	c
FCC02190	-13.91	15.89	1.97	-10.93	12.82	1.89	-6.92	8.90	1.99	r
FCC02206	-15.65	17.10	1.45	-11.29	12.70	1.41	-6.96	8.44	1.48	o
FCC02246*	-29.81	16.10	-13.71	-5.95	9.95	4.00	-4.43	8.50	4.07	c
FCC02262	-13.76	15.75	1.99	-14.38	16.29	1.90	-5.01	7.08	2.07	r
FCC02278	-14.47	16.00	1.52	-10.02	11.53	1.51	-6.22	7.80	1.58	o
FCC02294	-24.44	26.76	2.32	-19.07	21.26	2.19	-18.26	20.32	2.06	b
FCC02318	-8.95	13.19	4.24	-9.13	12.97	3.84	-3.25	7.53	4.28	c
FCC02334	-10.82	12.93	2.11	-11.54	13.56	2.03	-5.53	7.69	2.16	r
FCC02350	-15.49	17.08	1.59	-11.38	12.91	1.53	-6.44	8.06	1.62	o
FCC02366 ⋆	-25.27	28.11	2.85	-22.45	24.72	2.27	-23.50	25.64	2.14	b
FCC02390	-10.92	15.00	4.09	-2.60	7.41	4.81	-4.00	8.46	4.46	c
FCC02406	-11.84	13.93	2.08	-14.45	16.38	1.93	-4.70	6.83	2.14	r
FCC02422 ⋆	-15.59	17.07	1.48	-9.05	10.59	1.54	-4.85	6.49	1.65	o
FCC02438	-23.31	25.95	2.64	-22.06	24.35	2.29	-23.30	25.45	2.15	b
FCC02468	-6.12	10.34	4.23	-7.13	11.13	4.00	-2.20	6.85	4.64	c
FCC02484	-15.49	17.50	2.01	-10.37	12.41	2.04	-4.00	6.27	2.28	r
FCC02500	-12.80	14.46	1.66	-11.70	13.32	1.62	-4.98	6.73	1.75	o
FCC02516	-21.52	24.32	2.80	-21.19	23.62	2.44	-23.03	25.29	2.26	b
FCC02540	-6.13	10.68	4.55	-4.52	8.97	4.45	-2.61	7.52	4.91	c
FCC02556	-12.06	14.19	2.13	-10.75	12.87	2.11	-4.11	6.43	2.32	r
FCC02572	-14.01	15.58	1.57	-8.06	9.74	1.69	-4.66	6.45	1.79	o
FCC02588 ⋆	-18.33	21.14	2.81	-22.02	24.29	2.27	-22.57	24.92	2.36	b
FCC02612	-10.13	13.88	3.75	-5.49	9.89	4.39	-2.75	7.96	5.21	c
FCC02628*	-9.86	0.29	-9.57	-9.82	0.30	-9.53	-5.87	8.31	2.44	r
FCC02644	-1.58	3.40	1.82	-10.49	12.27	1.78	-4.94	6.87	1.93	o
FCC02660	-16.66	19.92	3.27	-21.73	24.16	2.43	-22.53	24.87	2.34	b
FCC02684	-11.46	15.29	3.82	-2.91	7.91	5.00	-2.50	7.72	5.21	c
FCC02700	-13.02	15.35	2.33	-9.06	11.48	2.42	-4.94	7.51	2.57	r
FCC02716	-10.68	12.60	1.92	-9.76	11.56	1.80	-4.05	6.03	1.98	o
FCC02732	-22.67	25.69	3.03	-22.02	24.50	2.49	-22.56	24.99	2.43	b
FCC02762*	-10.00	0.25	-9.75	-10.00	0.25	-9.75	-1.96	6.72	4.76	c
FCC02778	-9.14	11.87	2.73	-11.78	14.26	2.48	-5.35	8.02	2.68	r
FCC02794	-12.73	14.80	2.07	-10.19	12.18	1.99	-5.11	7.26	2.15	o
FCC02810	-30.37	33.51	3.14	-27.18	29.89	2.71	-22.90	25.47	2.57	b
FCC02834	-6.11	12.85	6.74	-11.61	15.41	3.80	-2.01	6.65	4.64	c
FCC02850	-14.42	16.96	2.55	-9.24	11.84	2.60	-4.58	7.41	2.83	r
FCC02866	-8.50	10.85	2.34	-9.88	11.97	2.09	-5.56	7.80	2.24	o
FCC02882	-13.75	17.77	4.02	-19.98	22.83	2.84	-22.86	25.58	2.72	b
FCC02906	-6.07	12.96	6.89	-7.34	11.32	3.98	-2.15	6.59	4.44	c
FCC02922	-5.11	8.63	3.52	-8.36	11.30	2.93	-5.89	8.96	3.07	r
FCC02938	-9.22	11.48	2.26	-9.16	11.43	2.28	-5.22	7.64	2.43	o
FCC02954	-18.60	22.04	3.44	-21.48	24.62	3.14	-30.22	33.18	2.96	b
FCC02978	-8.16	17.28	9.13	-7.77	11.48	3.71	-8.16	12.57	4.40	c

Continued on next page

Filename	$\leqq 2\,\mathrm{mW \cdot m^{-2} \cdot sr^{-1}}$			$\leqq 4\,\mathrm{mW \cdot m^{-2} \cdot sr^{-1}}$			$\leqq 6\,\mathrm{mW \cdot m^{-2} \cdot sr^{-1}}$			Filter
	Δx	λ	$\lambda + \Delta x$	Δx	λ	$\lambda + \Delta x$	Δx	λ	$\lambda + \Delta x$	
FCC02994	-9.31	12.38	3.06	-5.80	9.30	3.50	-5.55	9.22	3.67	r
FCC03010	-13.89	15.62	1.73	-8.73	11.27	2.54	-5.74	8.44	2.70	o
FCC03026	-13.87	17.44	3.57	-13.67	17.20	3.54	-27.85	31.09	3.24	b
FCC03056	-5.78	11.02	5.24	-11.73	15.92	4.20	-4.74	9.73	4.99	c
FCC03072	-8.84	11.84	3.00	-16.96	19.86	2.89	-7.16	11.22	4.06	r
FCC03088	-6.06	9.07	3.01	-18.80	21.46	2.66	-5.86	9.16	3.30	o
FCC03104 ⋆	-14.41	17.39	2.98	-13.90	17.17	3.27	-13.47	16.97	3.50	b
FCC03128 °	-5.95	18.82	12.87	-5.24	11.15	5.90	-17.26	30.25	12.99	c
FCC03136	-10.94	15.74	4.80	-9.18	13.97	4.79	-7.44	12.27	4.83	r
FCC03144	-10.21	14.37	4.15	-11.74	15.33	3.59	-7.07	11.19	4.12	o
FCC03152 ⋆	-13.84	17.51	3.67	-13.58	17.63	4.05	-13.31	17.50	4.19	b
FCC03160	-5.35	19.26	13.91	-5.59	12.65	7.06	-4.93	12.97	8.05	c
FCC03168	-11.91	15.28	3.36	-9.00	13.86	4.86	-7.88	12.79	4.91	r
FCC03176	-15.29	19.43	4.13	-16.21	19.86	3.65	-6.22	10.54	4.32	o
FCC03184 ⋆	-13.63	17.48	3.85	-13.44	17.73	4.29	-13.07	17.55	4.48	b
FCC03200	-10.41	14.77	4.36	-8.70	14.26	5.55	-7.14	12.81	5.67	r
FCC03208	-9.75	14.39	4.65	-18.62	22.82	4.20	-7.00	11.89	4.89	o
FCC03216 ⋆	-13.95	17.27	3.31	-13.52	17.64	4.12	-12.77	17.57	4.80	b
FCC03232	-10.71	17.24	6.53	-8.20	13.36	5.16	-10.18	15.10	4.92	r
FCC03240	-14.33	17.66	3.33	-17.72	20.46	2.75	-12.90	15.81	2.91	o
FCC03248 ⋆	-14.79	17.14	2.35	-14.53	17.44	2.92	-13.93	17.33	3.41	b
FCC03264	-12.69	18.26	5.58	-10.24	14.91	4.67	-9.21	13.98	4.77	r
FCC03272	-12.58	18.13	5.55	-13.31	17.06	3.75	-9.10	13.06	3.96	o
FCC03280 ⋆	-15.07	17.15	2.08	-12.27	15.82	3.55	-14.14	17.28	3.13	b
FCC03296	-10.80	17.82	7.02	-14.09	19.62	5.53	-11.00	17.95	6.95	r
FCC03304	-11.56	17.54	5.98	-17.21	22.80	5.59	-11.51	17.86	6.35	o
FCC03312 ⋆	-14.28	16.95	2.67	-14.10	17.48	3.38	-13.11	17.46	4.35	b
FCC03336	-5.22	13.26	8.05	-6.16	10.50	4.35	-9.30	14.12	4.83	o
FCC03344	-10.03	19.99	9.96	-8.46	14.51	6.05	-6.98	14.11	7.12	b
FCC03368	-7.43	18.77	11.34	-9.56	15.45	5.89	-12.27	17.46	5.19	o
FCC03376	-8.99	18.39	9.40	-11.47	18.10	6.63	-11.19	17.92	6.73	b
FCC03392	-6.48	19.00	12.52	-9.48	15.85	6.37	-5.90	12.74	6.83	r
FCC03400	-7.31	18.83	11.53	-11.82	19.56	7.74	-10.44	16.16	5.72	o
FCC03408	-8.98	18.38	9.40	-12.71	17.80	5.09	-11.91	17.74	5.83	b
FCC03432	-8.34	18.53	10.19	-11.12	18.22	7.10	-21.66	28.54	6.88	o

C. Additional information about HMC flyby data

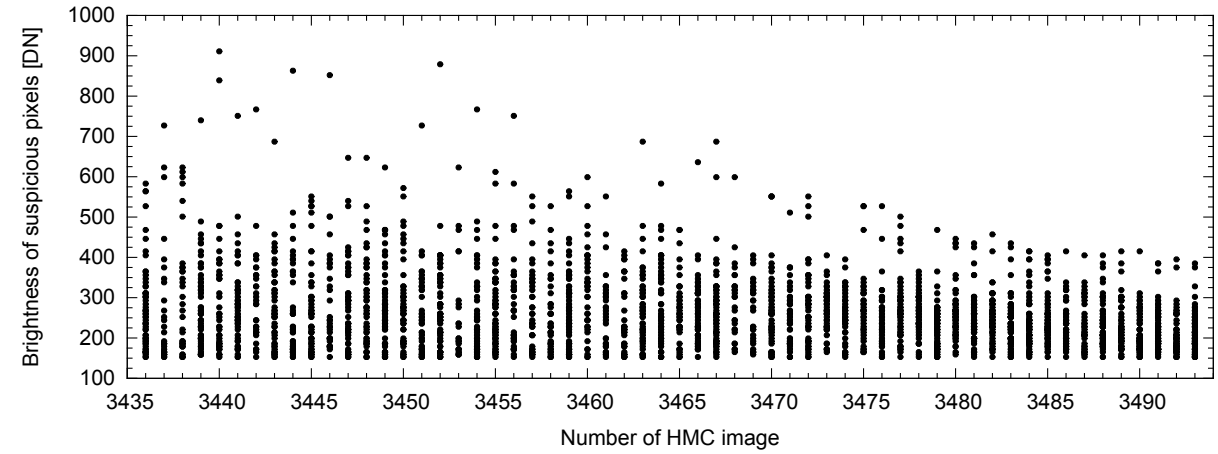

(a)

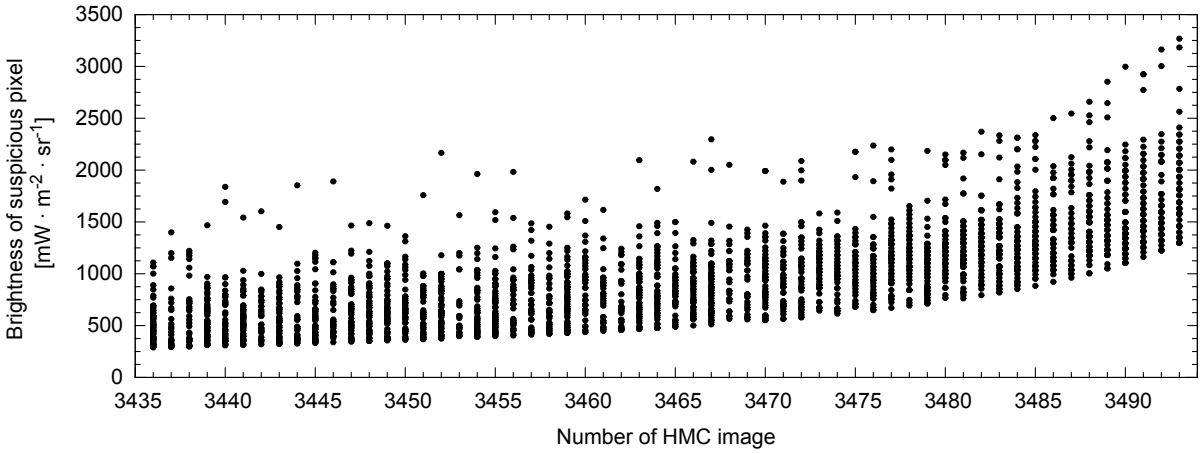

(b)

Figure C.1.: Brightness of suspicious pixels, $B_{min} = 150$ DN, $\sigma = 4$.

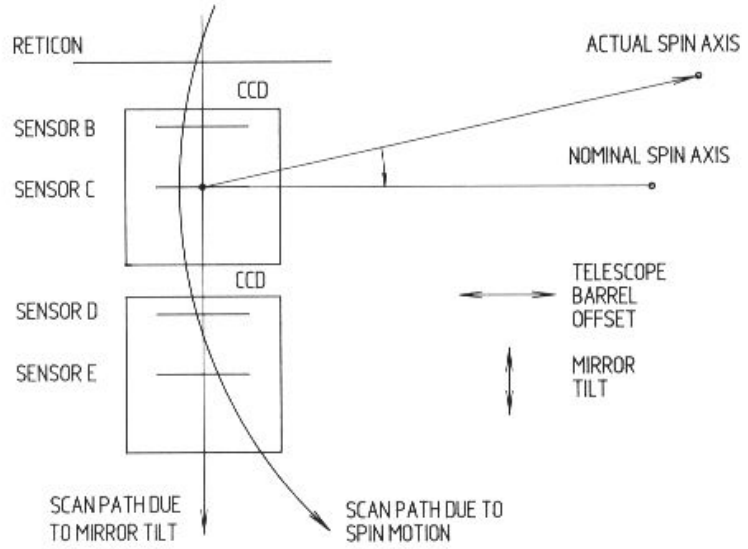

Figure C.2.: Apparent motion of an image across the focal plane showing the effect of the rotation mechanism, the spin motion, and the mirror tilt mechanism on the position of the image on the focal plane. Image from [8].

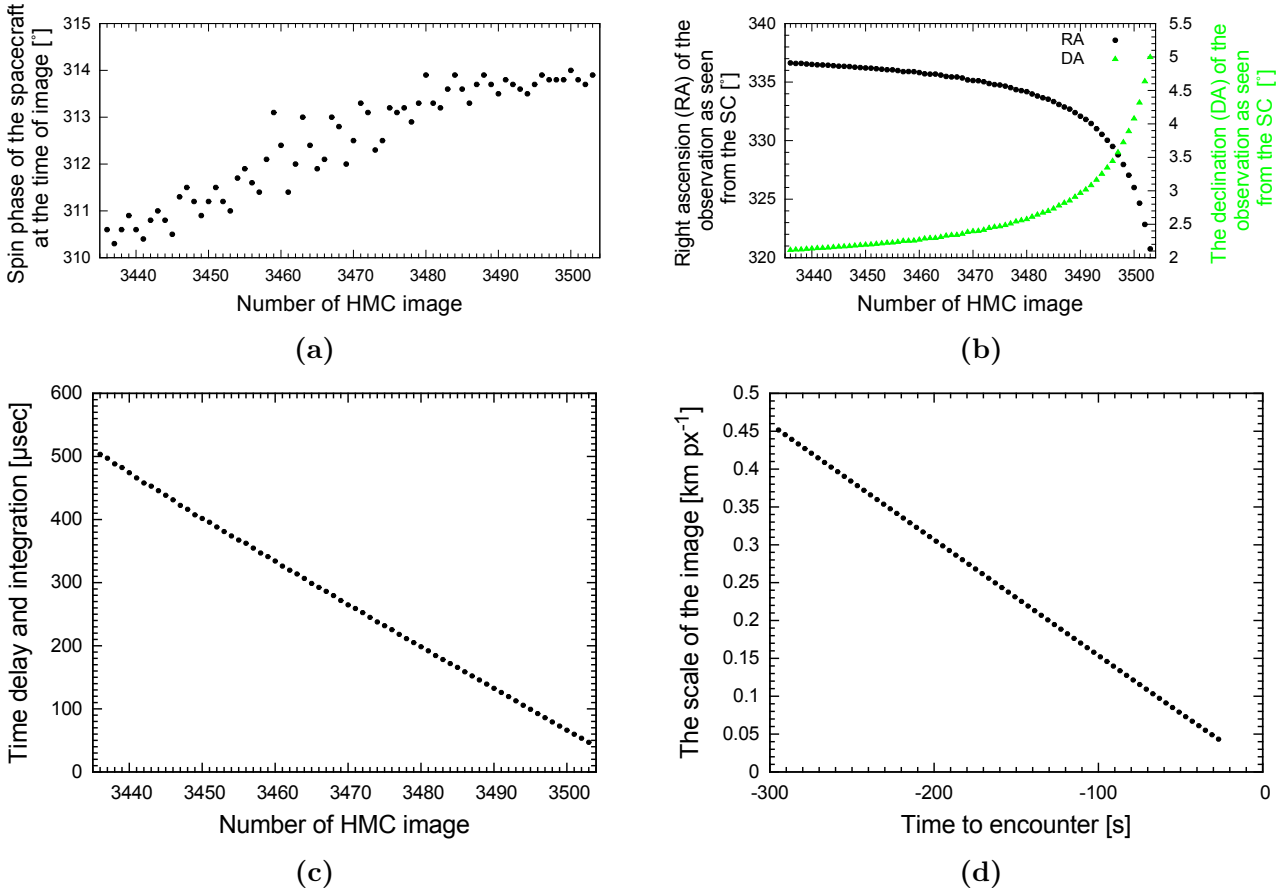

Figure C.3.: Additional information about MDM mode of HMC imaging.

D. Conic projection

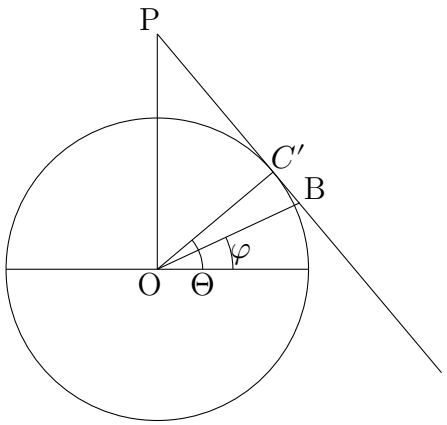

Figure D.1.: Side view of the celestial sphere with cone surface.

We transform latitude and longitude (ϕ, λ) on a unity sphere into angular coordinates on a cone surface (r, α). C' is a point on which cone touched a sphere (centre of image), B is the any point for which we want to calculate the coordinates, Θ is latitude of C', ϕ is the same angle but for point B (arbitrary pixel). From the fig. D.1 by definition:

$$\begin{aligned} \vec{r_0} &= P\vec{C}', \\ \vec{\Delta} r &= \vec{C'B}, \\ \vec{r} &= \vec{r_0} + \vec{\Delta} r. \end{aligned}$$

From fig. D.1:

$$r_0 = \cot\Theta, \Delta r = \tan(\Theta - \phi)$$

and thus:

$$r = \cot\Theta + \tan(\Theta - \phi)$$

In the reverse direction:

$$\phi = \Theta - \tan^{-1}(r - \cot\Theta)$$

E. Known values of the parameters related to the HMC characteristics and observations of the 1P/Halley comet

$F_{\odot} = 720.1\,\mathrm{W}\cdot\mathrm{m}^{-2}$ [44, page 264] for clear filter ($\lambda_{eff} = 652.9\,\mathrm{nm}$ [45])

$a = 2\times10^{-3} - 9\times10^{-3}$ [8, page 70]

$l = 596 - 2\,000\,\mathrm{km}$ [8, page 16]

$k_s = \pi$

$D = 130.4\times10^{-3}\,\mathrm{m}$ (calculated from effective collecting area), [8, page 25]

$i_{FOV} = 22.4\,\mathrm{rad} = 1.283\,425\,46\times10^{-3}°$, angular resolution [8, pages 22, 25]

$v_p = 20\times10^3 - 68.373\times10^3\,\mathrm{m}\cdot\mathrm{s}^{-1}$ [8, page 16]

$\tau = 14.2\,\mathrm{s/line} - 1\,\mathrm{ms/line}$ times number of TDI lines [8, table VIII on page 25]

$size_{image} = 74\,\mathrm{px}\times74\,\mathrm{px} = 0.095°\times0.095°$

$size_{pixel_{CCD}} = 22.35\,\mathrm{m}\times22.35\,\mathrm{m} = 22.4\,\mathrm{rad}\times22.4\,\mathrm{rad}$, [8, page 25]

$resolution_{imaging(nominal)} = 22\,\mathrm{m}$ at $1\,000\,\mathrm{km}$ distance, [8, page 25]

F. MRI images of Hartley 2 comet used in current work

FileName	UT_time	JD	S/C_Range[km]	Enc.time[s]
mv0342149249_5004029_001_rr.fit	13:58:53.107	2455505.082559	-963.144	-54.2
mv0342149254_5004030_001_rr.fit	13:58:58.069	2455505.082617	-921.809	-49.2
mv0342149259_5004031_001_rr.fit	13:59:02.822	2455505.082672	-884.369	-44.5
mv0342149264_5004032_001_rr.fit	13:59:07.784	2455505.082729	-847.837	-39.5
mv0342149268_6000001_001_rr.fit	13:59:12.631	2455505.082785	-815.004	-34.7
mv0342149273_5004040_001_rr.fit	13:59:17.452	2455505.082841	-785.494	-29.9
mv0342149278_5004041_001_rr.fit	13:59:22.299	2455505.082897	-759.361	-25.0
mv0342149283_5004042_001_rr.fit	13:59:27.261	2455505.082954	-736.673	-20.0
mv0342149288_5004044_001_rr.fit	13:59:32.010	2455505.083009	-719.167	-15.3
mv0342149293_5004045_001_rr.fit	13:59:36.976	2455505.083067	-705.602	-10.3
mv0342149298_5004046_001_rr.fit	13:59:41.823	2455505.083123	-697.3	-5.5
mv0342149303_6000002_001_rr.fit	13:59:46.699	2455505.083179	-694.051	-0.6
mv0342149307_5004051_001_rr.fit	13:59:51.487	2455505.083235	695.909	4.2
mv0342149312_5004052_001_rr.fit	13:59:56.453	2455505.083292	703.078	9.1
mv0342149317_5004053_001_rr.fit	14:00:01.300	2455505.083348	715.07	14
mv0342149322_5004054_001_rr.fit	14:00:06.168	2455505.083405	731.835	18.9
mv0342149327_5004056_001_rr.fit	14:00:11.011	2455505.083461	752.896	23.7
mv0342149332_5004057_001_rr.fit	14:00:15.891	2455505.083517	778.178	28.6
mv0342149337_5004058_001_rr.fit	14:00:20.819	2455505.083574	807.455	33.5
mv0342149342_6000003_001_rr.fit	14:00:25.785	2455505.083632	840.37	38.5
mv0342149347_5004061_001_rr.fit	14:00:31.488	2455505.083698	881.896	44.2
mv0342149352_5004062_001_rr.fit	14:00:36.453	2455505.083755	920.892	49.1
mv0342149357_5004063_001_rr.fit	14:00:41.394	2455505.083812	961.993	54.1
mv0342149362_5004064_001_rr.fit	14:00:46.262	2455505.083869	1004.451	59

Figure F.1.: Our working set of MRI images. Table columns are: full file name (inner numbering); UT time; JD; S/C_Range: spacecraft–comet distance; Enc.time: time related to encounter.

Exposure[ms]	Scale[m]	Phase[deg]	FileNamePDS
120.5	9.6	79.9	MV10110413_5004029_001_RR.FIT
40.5	9.2	79.7	MV10110413_5004030_001_RR.FIT
120.5	8.8	79.5	MV10110413_5004031_001_RR.FIT
40.5	8.5	79.3	MV10110413_5004032_001_RR.FIT
120.5	8.2	79.2	MV10110413_6000001_001_RR.FIT
40.5	7.9	79	MV10110413_5004040_001_RR.FIT
120.5	7.6	79	MV10110413_5004041_001_RR.FIT
40.5	7.4	79	MV10110413_5004042_001_RR.FIT
120.5	7.2	79	MV10110413_5004044_001_RR.FIT
40.5	7.1	79.1	MV10110413_5004045_001_RR.FIT
120.5	7	79.3	MV10110413_5004046_001_RR.FIT
40.5	6.9	79.6	MV10110413_6000002_001_RR.FIT
120.5	7	80	MV10110413_5004051_001_RR.FIT
40.5	7	80.4	MV10110413_5004052_001_RR.FIT
120.5	7.2	80.9	MV10110414_5004053_001_RR.FIT
40.5	7.3	81.4	MV10110414_5004054_001_RR.FIT
120.5	7.5	82	MV10110414_5004056_001_RR.FIT
40.5	7.8	82.6	MV10110414_5004057_001_RR.FIT
120.5	8.1	83.1	MV10110414_5004058_001_RR.FIT
40.5	8.4	83.7	MV10110414_6000003_001_RR.FIT
120.5	8.8	84.3	MV10110414_5004061_001_RR.FIT
40.5	9.2	84.8	MV10110414_5004062_001_RR.FIT
120.5	9.6	85.2	MV10110414_5004063_001_RR.FIT
40.5	10	85.7	MV10110414_5004064_001_RR.FIT

Figure F.2.: Our working set of MRI images. Table columns are: exposure time; scale: pixel scale at the distance of the comet; phase angle: Sun–comet–spacecraft; full file name at PDS archive.

G. Intermadiate progress in testing the pointing search

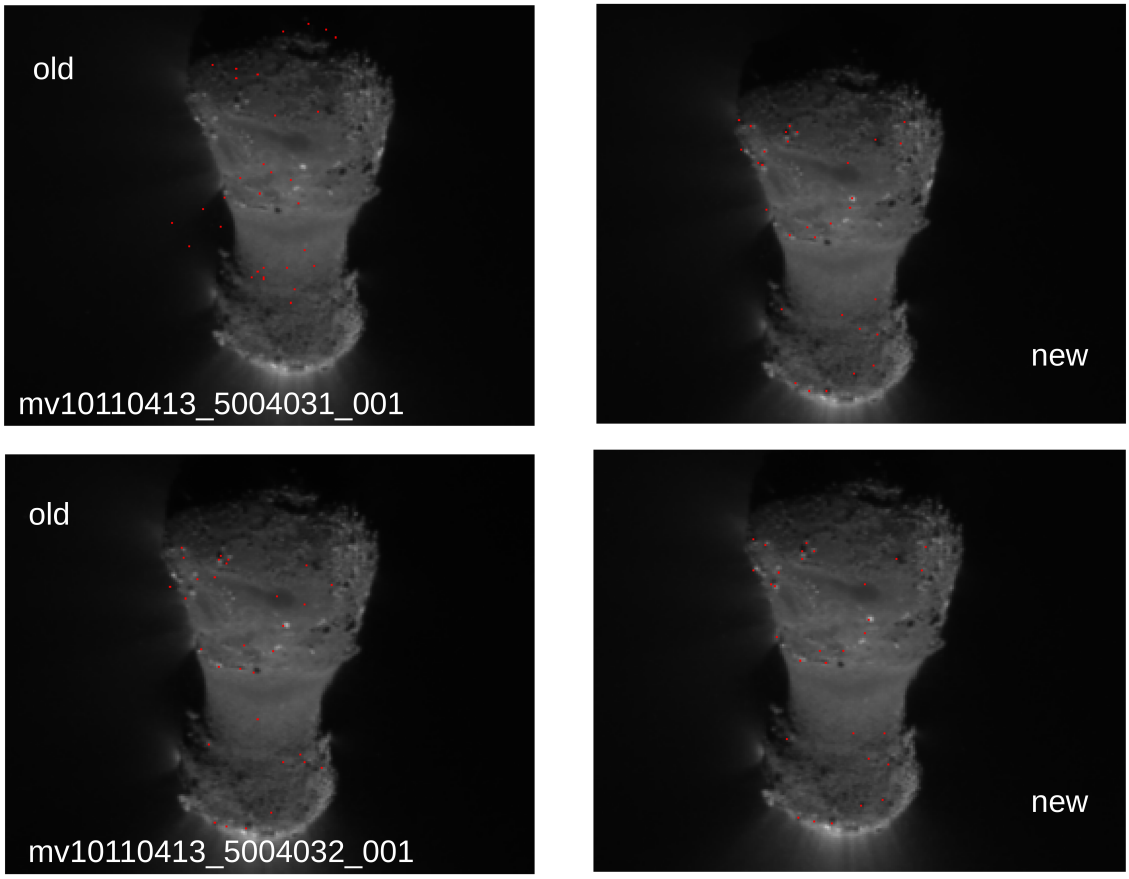

Figure G.1.: Intermediate progress: comparison of two approaches of automatic searching of camera position and orientation shown at examples of several images. Positions of test base points are shown by red dots: it is seen that for the "old" method programm restore wrong position of the basic points (some of them are placed even out of the comet).

H. Details connected to the pointing test

Here there are some details about the pointing test.

It were measured and compared two angles (they have to be equal). The first angle (the angle between the center of the nucleus and the reference point in image) we can measure directly from Dr. Farnham file as$[(x2 - x1)^2 + (y2 - y1)^2]^{0.5}$. To get the second angle (between directions from SC to the center of the nucleus and the reference point), we used SPICE and the nucleus shape model in the following way:

1. Observational date is taken from FITS header field "RECTDBSC" assuming that this is ephemeride time ET already (no conversion).
2. Call cidfrm() to get default frame for body 1000041 (Hartley 2).
3. For "DIF_MRI" instrument the 'INS" `'+ < id > + "_PLATFORM_ID" parameter is read to get body ID of the spacecraft.
4. Call spkezp() to get SC position in the default frame of the nucleus (2), using obtained time and LT+S aberration correction.

Then, in the shape model the coordinates of the bright point (which it is believable is Dr. Farnham's reference) was found. Model coordinates of the bright object (3 possible positions at shape model):

1. (0.0835456, 0.0309829, -1.05186)
2. (0.128334, 0.056577, -0.989622)
3. (0.0345464, 0.0925587, -1.03992)

The shape model is given in the same frame as returned by SPICE in step 2 (at least this is written in the fk/di_v18.tf file). Now I compute the angle, and convert it to pixels using scale of 1e-5 rad/px (neglecting distortions).

The comparison was plotted fig. 6.10b for three possible locations of the reference point (white detail at comet image), and the first one is the most probable (and it produced the smallest difference).